Chaotic Modeling and Simulation (CMSIM) 3 : 357-365, 2013

Correlation Relations and Statistical Properties of the Deformation Field of Fractal Dislocation in a Model Nanosystem

Valeriy S. Abramov

Donetsk Institute for Physics and Engineering named after A.A. Galkin,
National Academy of Sciences of Ukraine, Ukraine
E-mail: vsabramov@mail.ru

Abstract: A model sample of a finite nanosize with the volumetric lattice in the form of a rectangular parallelepiped is considered. On the basis of the previously proposed one-point model, a two-point model is constructed, which uses the theory of fractional calculus and the concept of fractal. The features of the behavior of the deformation field of fractal dislocation and possible correlation connections are investigated. It is shown that complex correlation connections have negative, positive and sign changing correlation coefficients. The strongly pronounced stochastic behaviour of amplitudes and phases of average functions is established. The change of the statistics from Fermi-Dirac type to the statistics of Boze-Einstein type for separate internal nodal planes is shown by the method of numerical modeling.
Keywords: fractal dislocation, nanosystem, stochastic deformation field, numerical modeling, distribution functions, correlation connections.

1. Introduction

For experimental studies of the physical properties of individual atoms (electrons, photons) and the quantum measurement it is necessary to create special traps: nanosystem - trapped particles (or group of particles) in a trap. These traps can be useful for realization of optical quantum computation with quantum information processing, measurement in quantum optics [1]. In his Nobel lecture in Physics in 1989 W. Paul [2] considered electromagnetic traps for charged and neutral particles. For the observation of Bose-Einstein condensation phenomenon [3] the magnetic traps were used. Serge Haroche and David Wineland, 2012 Nobel laureates in Physics, proposed experimental methods that made it real to measure individual quantum systems and govern them [4, 5]. The experimental studies of the features of the statistical properties of individual quantum systems in neutron spin measurements [6], with the observation of Bose-Einstein condensation [7] showed the presence of correlations in the measured values. Near singular points (Dirac points) Dirac fermions in molecular graphene show quantum and statistical features of behavior [8].

Received: 2 April 2013 / Accepted: 7 July 2013

ISSN 2241-0503

Fractal dislocation is one of the structural objects in nanostructured materials [9, 10]. The core of a linear dislocation is a set of singular points. The deformation field of fractal dislocation has unusual quantum and statistical properties [11 - 13] and shows the presence of quantum chaos [14]. Earlier a one-point model was used to describe the structural states of the deformation field of fractal dislocation [10, 12] (fractal dimension was an effective coordinate). In this model, the elements of the displacement of the lattice nodes are real random functions and were determined without the effect of bifurcation of solutions of a nonlinear equation. However, consideration of the effect of bifurcation of solutions [11] leads to the four branches of the lattice nodes displacement function. Elements of the lattice nodes displacement matrix become complex random functions. In order to describe possible correlation effects and statistical properties of the deformation field of fractal dislocation of pure structural states a two-point model was proposed [15] in which the theory of fractional calculus [16] and the concept of fractal [17] are used. It is necessary to investigate the mixed states, the description of which requires introducing the density of states and accounting for the distribution of this density of states on nodes of the volumetric lattice.

The purpose of this paper is to generalize the two-point model to the case of mixed state and investigate correlation connections and the statistical properties of the deformation field of fractal dislocation in the model nanosystem.

2. Description of mixed states in the two-point model

A model nanosystem [15] is considered: a sample in the form of a rectangular parallelepiped of finite size with volumetric discrete lattice $N_1 \times N_2 \times N_3$. Deviations of the lattice nodes from the state of equilibrium in a separate plane $N_1 \times N_2$ for two different points of $z_1(j)$ and $z_2(j)$ are described by non-hermitian displacements operators $\hat{u}(z_1)$ and $\hat{u}(z_2)$, corresponding to the rectangular matrix with dimensions $N_1 \times N_2$, $j \in [1, N_3]$.

For the description of mixed states the effective composite operators of displacements for the states $p = 1,2,...8$ are introduced, respectively,

$$\hat{u}_1 = \hat{\rho}_{12}\hat{u}^+(z_1);\ \hat{u}_3 = \hat{\rho}_{12}\hat{u}^+(z_2);\ \hat{u}_5 = \hat{u}(z_1)\hat{\rho}_{12}^T;\ \hat{u}_7 = \hat{u}(z_2)\hat{\rho}_{12}^T; \quad (1)$$

$$\hat{u}_2 = \hat{\rho}_{21}\hat{u}(z_1);\ \hat{u}_4 = \hat{\rho}_{21}\hat{u}(z_2);\ \hat{u}_6 = \hat{u}^+(z_1)\hat{\rho}_{21}^T;\ \hat{u}_8 = \hat{u}^+(z_2)\hat{\rho}_{21}^T. \quad (2)$$

Here the symbols «+» and «T» mean the operation of hermitian conjugation and transposition. The square matrices with sizes $N_1 \times N_1$ for $p = 1,3,5,7$ and $N_2 \times N_2$ for $p = 2,4,6,8$ correspond to the introduced operators $\hat{u}_p$; so that $\hat{u}_5 = \hat{u}_1^+$, $\hat{u}_7 = \hat{u}_3^+$, $\hat{u}_6 = \hat{u}_2^+$, $\hat{u}_8 = \hat{u}_4^+$. The density state operators $\hat{\rho}_{12}, \hat{\rho}_{12}^T$, $\hat{\rho}_{21}, \hat{\rho}_{21}^T$ are represented by

$$\hat{\rho}_{12} = \hat{\xi}_{N1}^T\hat{\xi}_{N2} / N_1N_2;\ \hat{\rho}_{12}^T = \hat{\xi}_{N2}^T\hat{\xi}_{N1} / N_1N_2;\ \hat{\rho}_{21} = \hat{\rho}_{12}^T;\ \hat{\rho}_{21}^T = \hat{\rho}_{12}, \quad (3)$$

where $\hat{\xi}_{N1}$, $\hat{\xi}_{N2}$ are row-vectors of dimensions $1\times N_1$, $1\times N_2$, with elements equal to one. The rectangular matrices $\hat{\rho}_{12}$, $\hat{\rho}_{21}$ have dimensions $N_1\times N_2$, $N_2\times N_1$. For the operators in (3) the normalization conditions are fulfilled

$$\hat{\xi}_{N1}\hat{\rho}_{12}\hat{\xi}_{N2}^T=1;\qquad \hat{\xi}_{N2}\hat{\rho}_{21}\hat{\xi}_{N1}^T=1. \tag{4}$$

Having performed an averaging over the index nodes n,m by calculating trace Sp of square matrices (1), (2), the averaged functions u_p, $|u_p|$, $tg\varphi_p$ for states with $p=1,2,...8$ are obtained

$$u_p=Sp\hat{u}_p=u'_p+iu''_p=|u_p|\exp(i\varphi_p);\ u_p^*=Sp\hat{u}_p^+;\ tg\varphi_p=u''_p/u'_p, \tag{5}$$

where $u'_p=\mathrm{Re}\,u_p$, $u''_p=\mathrm{Im}\,u_p$; the symbol «$*$» means the operation of complex conjugation; $|u_p|$, φ_p are a module, a phase of the complex averaged functions u_p. Here the averaging across an index j is not made.

Then we find the correlation function of the first order. For $p,q=1,3,5,7$ we obtain

$$K_{pq}=S_{pq}-H_{pq}=K'_{pq}+iK''_{pq}=|K_{pq}|\exp(i\theta_{pq});$$
$$S_{pq}=Sp\hat{S}_{pq}=S'_{pq}+iS''_{pq}=|S_{pq}|\exp(i\psi_{pq});\ \hat{S}_{pq}=\hat{u}_p\hat{u}_q^+;\ \hat{S}_{pq}^+\neq\hat{S}_{pq};$$
$$H_{pq}=(Sp\hat{u}_p)(Sp\hat{u}_q^+)=u_pu_q^*=H'_{pq}+iH''_{pq}=|H_{pq}|\exp(i\delta_{pq});$$
$$|H_{pq}|=|u_p|\cdot|u_q|;\quad \delta_{pq}=\varphi_p-\varphi_q. \tag{6}$$

In the case $p,q=2,4,6,8$ we obtain

$$C_{pq}=A_{pq}-B_{pq}=C'_{pq}+iC''_{pq}=|C_{pq}|\exp(i\beta_{pq});$$
$$A_{pq}=Sp\hat{A}_{pq}=A'_{pq}+iA''_{pq}=|A_{pq}|\exp(i\chi_{pq});\ \hat{A}_{pq}=\hat{u}_p\hat{u}_q^+;\ \hat{A}_{pq}^+\neq\hat{A}_{pq};$$
$$B_{pq}=(Sp\hat{u}_p)(Sp\hat{u}_q^+)=B'_{pq}+iB''_{pq}=|B_{pq}|\exp(i\gamma_{pq});$$
$$|B_{pq}|=|u_p|\cdot|u_q|;\quad \gamma_{pq}=\varphi_p-\varphi_q. \tag{7}$$

From (6) at $p=q$ we have $\delta_{pp}=0$, $H_{pp}=|H_{pp}|=|u_p|^2$; operators $\hat{S}_{pp}=\hat{S}_{pp}^+$ are hermitian, $S''_{pp}=0$, $S_{pp}=S'_{pp}$ and

$$K_{pp}=S'_{pp}-|H_{pp}|=|K_{pp}|\exp(i\theta_{pp}). \tag{8}$$

From (8) it follows that $\theta_{pp}=\pi k$, where $k=0,\pm1,\pm2,..$ and autocorrelation function can be either positive ($k=0,\pm2,\pm4,..$) or negative ($k=\pm1,\pm3,..$). From (7) at $p=q$ we obtain $\gamma_{pp}=0$, $B_{pp}=|B_{pp}|=|u_p|^2$; then operators

$\hat{A}_{pp} = \hat{A}^{+}_{pp}$ are hermitian, $A''_{pp} = 0$, $A_{pp} = A'_{pp}$ and

$$C_{pp} = A'_{pp} - |B_{pp}| = |C_{pp}| \exp(i\beta_{pp}). \tag{9}$$

From (9) it follows that $\beta_{pp} = \pi l$, where $l = 0, \pm 1, \pm 2, ..$ and autocorrelation function can be either positive ($l = 0, \pm 2, \pm 4, ..$) or negative ($l = \pm 1, \pm 3, ..$). Having done the normalization of the above functions, we obtain the distribution function of mixed states of Bose-Einstein type and Fermi-Dirac type for $p = 1,3,5,7$ in form

$$f'_{pp} - f_{pp} = 1; \quad f'_{pp} = S_{pp} / H_{pp}; \quad f_{pp} = K_{pp} / H_{pp}; \tag{10}$$

$$F'_{pp} + F_{pp} = 1; \quad F_{pp} = H_{pp} / S_{pp}; \quad F'_{pp} = K_{pp} / S_{pp}, \tag{11}$$

and for $p = 2,4,6,8$ in form

$$f'_{pp} - f_{pp} = 1; \quad f'_{pp} = A_{pp} / B_{pp}; \quad f_{pp} = C_{pp} / B_{pp}; \tag{12}$$

$$F'_{pp} + F_{pp} = 1; \quad F_{pp} = B_{pp} / A_{pp}; \quad F'_{pp} = C_{pp} / A_{pp}. \tag{13}$$

By numerical simulation it will be shown that for mixed states all autocorrelation functions $K_{pp}(j), C_{pp}(j)$ are positive in the interval $j \in [1; N_3]$. Earlier in [15] it was shown that for pure states similar autocorrelation functions are negative.

At $p \neq q$ from (6), (7) it follows that the functions K_{pq}, C_{pq} are complex. For some values p, q these functions have a sense of cross-correlated functions (for a pair of different points z_1, z_2). In this case, to investigate the correlations it is necessary to introduce second-order correlation functions. For $p, q = 1,3,5,7$ we have

$$G_{pq} = V_{pq} - W_{pq}; \quad V_{pq} = Sp\hat{V}_{pq}; \quad \hat{V}_{pq} = \hat{S}_{pq}\hat{S}^{+}_{pq}; \quad \hat{V}^{+}_{pq} = \hat{V}_{pq};$$
$$W_{pq} = (Sp\hat{S}_{pq})(Sp\hat{S}^{+}_{pq}) = S_{pq}S^{*}_{pq} = |S_{pq}|^2. \tag{14}$$

Using (6), we find a representation for

$$|S_{pq}|^2 = (|K_{pq}| - |u_p| \cdot |u_q|)^2 + 2|u_p| \cdot |u_q| \cdot |K_{pq}| (1 + \cos\Phi_{pq}), \tag{15}$$

where $\Phi_{pq} = \delta_{pq} - \theta_{pq}$. For $p, q = 2,4,6,8$ we obtain

$$g_{pq} = v_{pq} - w_{pq}; \quad v_{pq} = Sp\hat{v}_{pq}; \quad \hat{v}_{pq} = \hat{A}_{pq}\hat{A}^{+}_{pq}; \quad \hat{v}^{+}_{pq} = \hat{v}_{pq};$$
$$w_{pq} = (Sp\hat{A}_{pq})(Sp\hat{A}^{+}_{pq}) = A_{pq}A^{*}_{pq} = |A_{pq}|^2. \tag{16}$$

Using (7), we find a representation for

$$|A_{pq}|^2 = (|C_{pq}| - |u_p| \cdot |u_q|)^2 + 2|u_p| \cdot |u_q| \cdot |C_{pq}| (1 + \cos\Psi_{pq}), \tag{17}$$

where $\Psi_{pq} = \gamma_{pq} - \beta_{pq}$. At some points $j \in [1; N_3]$ changes sign at second order correlation functions $G_{pq}(j), g_{pq}(j)$ from the expressions (14) - (17) which confirms the presence of a mixed statistics.
When describing pure states [15] of the deformation field of fractal dislocation in the two-point model, the following operators and functions were introduced

$$\hat{M}_7 = \hat{u}(z_2)\,\hat{u}^+(z_1); \quad \hat{M}_8 = \hat{u}^+(z_1)\hat{u}(z_2)\ ; \quad \hat{S}_r = \hat{M}_r\hat{M}_r^+;$$

$$S_r = Sp\hat{S}_r; \qquad H_r = (Sp\hat{M}_r)(Sp\hat{M}_r^+); \qquad K_r = S_r - H_r;$$

$$f_r' - f_r = 1; \quad f_r = -K_r / S_r; \quad f_r' = H_r / S_r; \quad r = 7,8. \tag{18}$$

Correlation functions K_r are sign changing within the interval $j \in [1; N_3]$ and describe the states with mixed statistics.

3. Numerical simulation and the analysis of results

The original rectangular matrix displacement $\hat{u}(z_1)$ and $\hat{u}(z_2)$ with elements $u_{nm}(z_1) = u_{\varepsilon 1}(z_1)$, $u_{nm}(z_2) = u_{\varepsilon 1}(z_2)$ in bulk lattice $N_1 \times N_2 \times N_3 = = 30 \times 40 \times 67$ were obtained by the method of iterations on an index m for the first branch of the dimensionless complex function displacement $u(z) = u_{\varepsilon 1}(z)$ by the formulas in [15] under the same input parameters and initial conditions. In the calculations it should be: $z_1 = 0.053 + 0.1(j-1); z_2 = 6.653 - 0.1(j-1)$, which corresponds to the forward and backward waves of displacements $u_{nm}(z_1), u_{nm}(z_2)$; $n = \overline{1,30}$; $m = \overline{1,40}$; $j = \overline{1,67}$. The choice of the model parameters determines the state of a discrete rectangular sublattice $N_1 \times N_2$ with fractal dislocation, localized within this region parallel to the axis Om.
The analysis of the results of the numerical simulation for the mixed states (Fig. 1) shows that all of the first-order correlation functions K_{pp} are positively defined on the whole interval $j \in [1, 67]$. This means that for states pp there are correlation relations with positive correlation coefficients. The distribution function of the Fermi-Dirac type $F_{55}(j)$ with increasing j (Fig. 1, a) varies randomly around the value of 0.1, goes to the stochastic peak at $j = 26$ with the value $F_{55}(26) = 0.3315$ and then again randomly changed by another law near the value of 0.1. The distribution function of the $F_{77}(j)$ with increasing j (Fig. 1,c) also varies randomly near the value of 0.1, comes to a peak at the other stochastic value of $j = 42$ with the same value of $F_{77}(42) = 0.3315$ and then again changes randomly by another law near the value of 0.1. In this case the values of the functions of $F_{55}(j)$, $F_{77}(j)$ in the peaks do not exceed the value of 0.5, which is typical for the ground state Fermi-system. The

distribution functions of Bose-Einstein type $f_{55}(j)$, $f_{77}(j)$ (Fig. 1,b,d) randomly change with increasing j near the population number equal to 10, in separate planes the peaks with large population numbers are observed. Such a behavior of functions $f_{55}(j)$, $f_{77}(j)$ indicates that the ground state of a Bose-system is populated (the population number greater than 1). The global minima with the values $f_{55}(26) = f_{77}(42) = 2.0162$ are observed in the points at which the main peaks of the functions $F_{55}(j)$, $F_{77}(j)$ are observed. The above values of the functions in global minima and main peaks indicate that the correlations in both ground and excited states of both Bose- and Fermi-systems are taken into account.

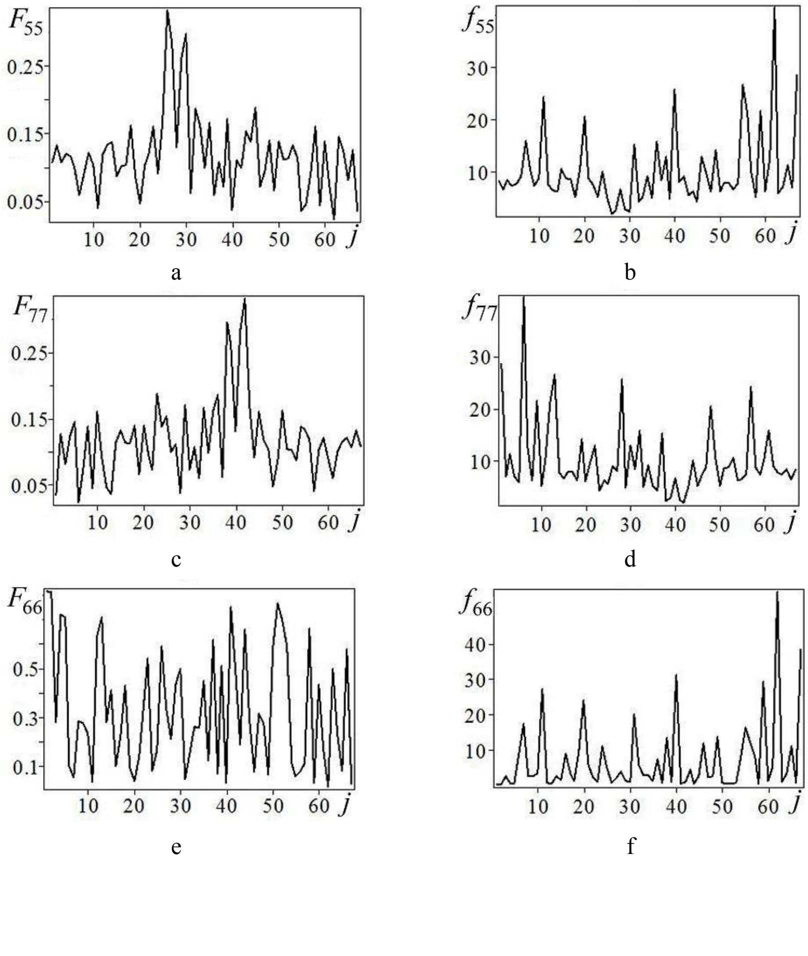

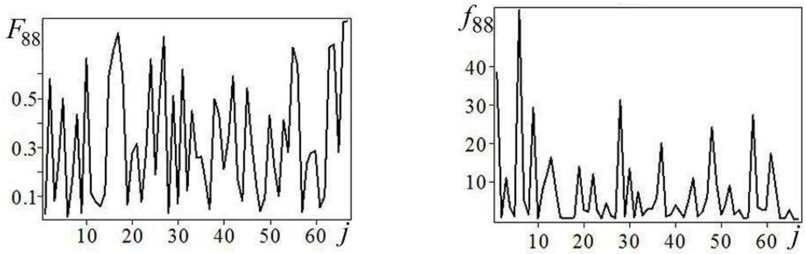

g h

Fig. 1. Dependencies of the distribution functions of the Fermi-Dirac type (a, c, e, g) and Bose-Einstein type (b, d, f, h) on j for mixed states *pp*

In this case, the autocorrelation function K_{55} describes a forward wave, and the autocorrelation function K_{77} describes a backward wave. The distribution functions of the Fermi-Dirac type $F_{66}(j), F_{88}(j)$ with increasing j (Fig. 1,e,g) vary randomly around 0.5. The values of the functions in individual peaks are higher than 0.5, which is typical for inverted states of Fermi-systems. The distribution functions of Bose-Einstein type $f_{66}(j)$, $f_{88}(j)$ (Fig. 1,f,h) randomly change with increasing j near the occupation numbers from 0 to 10, in separate planes the peaks with large population numbers are observed.

Accounting ordering pair operators in (1), (2) (the displacement and density of states of the lattice nodes) in the correlation function (6) - (9) leads to different distribution functions (10) - (13), as confirmed by numerical simulations (Fig. 1).

The dependencies of the distribution functions with mixed statistics (18) on an integer index j of a nodal plane for pure states at $r = 7,8$ are shown in Fig. 2.

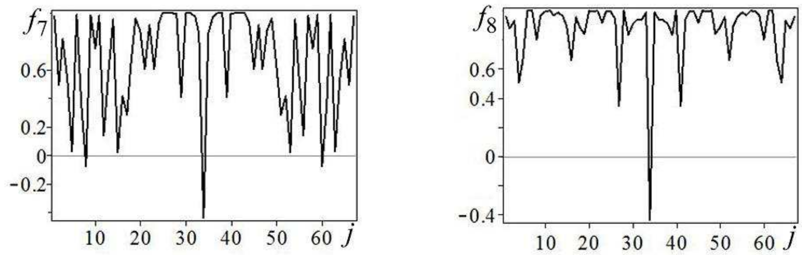

a b

Fig. 2. Dependencies of the distribution functions with mixed statistics on j for pure states

At some points j changes sign at functions f_7, f_8, which confirms the presence of a mixed statistics. In this case functions f_r and f'_r may be interpreted as Fermi-Dirac type distribution functions for those areas of changes for j, where $K_r > 0$, and at $K_r < 0$ as Bose-Einstein type distribution functions in the main and excited states, respectively. Note the pronounced stochastic behavior of the amplitudes $|M_r|$ and phases μ_r have of averaged functions $M_r = Sp\hat{M}_r = =|M_r|\exp(i\mu_r)$.

The possibility of changing the sign of real parts of the first order complex correlation functions $K_{pq}(j), C_{pq}(j)$ (6), (7) and second order correlation functions $G_{pq}(j)$, $g_{pq}(j)$ (14), (16) is also confirmed by the results of the numerical simulations.

4. Conclusions

The numerical simulation has confirmed the theoretical conclusion of the presence of a mixed statistics: the change of the statistics from Fermi-Dirac type to the statistics of Boze-Einstein type for separate internal nodal planes of the bulk lattice. The analysis of the distribution functions of the occupation numbers for mixed states shows that particular nodal planes may be in inverse structural states.

Based on the analysis of the correlation functions of the first and second order a possibility of changing the sign of real parts of the correlation functions is shown. This indicates a possible change in the nature of the interaction (attraction or repulsion) between lattice nodes within a single nodal plane as well as between different planes.

Accounting ordering pair operators (displacement and density of states the lattice nodes) in the correlation function has the effect of deviations of the initial distribution function.

References

1. M.O Scully, M.S. Zubairy. *Quantum Optics*. Cambridge: Cambridge Univ. Press, 1997.
2. W. Paul. Electromagnetic traps for charged and neutral particles. *Rev. of Modern Physics* **62,** 3: 531-543, 1990.
3. M.H. Anderson, J.R. Ensher, M.R. Matthews et al. Observation of Bose-Einstein condensation in a dilute atomic vapor. *Science* **269,** 5221: 198-201, 1995.
4. S. Gleyzes, S. Kuhr, C. Guerlin et al. Quantum jumps of light recording the birth and death of a photon in a cavity. *Nature* **446**: 297-300, 2007.
5. C.W. Chou, D.B. Hume, T. Rosenband, D.J. Wineland. Optical clocks and relativity. *Science* **329**: 1630-1633, 2010.
6. J. Erhart, S. Sponar, G. Sulyok. Experimental demonstration of a universally valid error-disturbance uncertainty relation in spin measurements. *Nature Physics* **8**: 185-189, 2012.
7. A. Perrin, R. Bücker, S. Manz. Hanbury Brown and Twiss correlations across the Bose-Einstein condensation thereshold. *Nature Physics* **8**: 195-198, 2012.
8. K.K. Gomes, W. Mar, W. Ko, F. Guinea et al. Designer Dirac fermions and topological phases in molecular graphene. *Nature* **483,** 7389: 306-310, 2012.
9. V.S. Abramov. Fractal dislocation as one of non-classical structural objects in the nano-dimensional systems. *Metallofiz. i Noveishie Tekhnologii* **33,** 2: 247-251, 2011.

10. O.P. Abramova, S.V. Abramov. Alteration of the structure of the stochastic dislocation deformation field under the change of governing parameters. *Metallofiz. i Noveishie Tekhnologii* **33,** 4: 519-524, 2011.
11. V.S. Abramov. Behavior of the deformation field of fractal dislocation in the presence of bifurcftions. *Bul. of Donetsk Nat. Univers.* Ser. **A,** 2: 23-29, 2011.
12. O.P. Abramova, S.V. Abramov. Deterministic and stochastic governance of the alteration of the fractal dislocation structure. *Bul. of Donetsk Nat. Univers*. Ser. **A**, 2: 30-35, 2011.
13. V.S. Abramov. Inverse structural states of the stochastic deformation field of fractal dislocation. *Book of Abstracts 4th Chaotic Modeling and Simulation International Conference (CHAOS 2011), May 31 - June 3, 2011, Agios Nikolaos, Crete Greece*. p. 10, Greece, 2011.
14. H.-J. Stockmann. *Quantum Chaos. An Introduction.* Cambridge Univers. Press, 1999.
15. V.S. Abramov. Features of statistical properties of the deformation field of the fractal dislocation. *Bul. of Donetsk Nat. Univers*. Ser. **A,** 1: 105-113, 2012.
16. S.G. Samko, A. Kilbas, O. Marichev. *Fractional Integrals and Derivatives. Theory and Applications*. Gordon and Breach Sci. Publ., New York et alibi, 1990.
17. B.B. Mandelbrot. *The Fractal Geometry of Nature*. Freeman, New York, 1982.

Governance of Alteration of the Deformation Field of Fractal Quasi-Two-Dimensional Structures in Nanosystems

Olga P. Abramova, Sergey V. Abramov

Donetsk National University, Ukraine
E-mail: oabramova@ua.fm

Abstract: A model nanosystem is investigated: a sample in the form of a rectangular parallelepiped of finite size with volumetric discrete lattice. It is shown that a separate nodal plane of a model nanosystem can be in different structural states: stochastic state of the deformation field on the whole rectangular lattice; the state with the linear fractal dislocation of different orientations; quasi-two-dimensional structures of the type of fractal elliptical, hyperbolic dislocations and fractal quantum dot. Using the numerical modelling method, the behaviour of the deformation field and a possibility of the alteration of these structures is investigated. The analysis of the behavior of the averaged functions allows to determine the critical values of the governing parameters.
Keywords: fractal quasi-two-dimensional structures, nanosystem, stochastic deformation field, numerical modeling, averaged functions, alteration of the structure.

1. Introduction

Investigation of fundamental properties of nanosystems and nanomaterials of a new generation [1, 2] is actual for modern areas of science and nanotechnology. Among the real nanomaterials the active nanostructural elements are clusters, porous, quantum dots, wells, corrals, surface superlattices. The physical properties of these elements can demonstrate chaotic behavior [3]. The active nanostructural elements can find their application in the quantum nanoelectronics, quantum informations [4], quantum optics. Previously in paper [5] fractons – vibrational excitations on fractals – were introduced. Fractal dislocation [6, 7] is one of the non-classical active nanostructural objects. For the theoretical descriptions of fractal objects it has been proposed [6, 7] to use the theory of fractional calculations [8] and the concept of fractals [9]. The new structural states [10-13] of fractal dislocation were investigated on the basis of fractional calculation theory and Hamilton operators. The purpose of the paper is to research a possibility of governing the alteration of the deformation field of fractal quasi-two-dimensional structures in model nanosystems.

2. Basic nonlinear equations

A model nanosystem is investigated: a sample in the form of a rectangular parallelepiped of a finite size with volumetric discrete lattice $N_1 \times N_2 \times N_3$,

Received: 2 April 2013 / Accepted: 17 July 2013

ISSN 2241-0503

whose nodes are given integers n, m, j ($n = \overline{1, N_1}$; $m = \overline{1, N_2}$; $j = \overline{1, N_3}$). In papers [11] the dimensionless variable displacement u of the lattice nodes is described by function

$$u = (1-\alpha)\left(1 - 2\, sn^2(u - u_0, k)\right) \big/ Q\,, \quad Q = p_{01} - p_1 n - p_2 m - p_3 j\,. \quad (1)$$

Here α is the fractal dimension of the deformation field u along the Oz-axis ($\alpha \in [0,1]$); u_0 is the constant (critical) displacement; k is the modulus of the elliptic sine; governing parameters p_{01}, p_1, p_2, p_3 do not depend on the integers n, m, j. This paper takes into account the parameters p_{01}, p_1, p_2, p_3 depending on the integers n, m, j. While modeling deformation fields of stochastic fractal quasi-two-dimensional structures, this allowed to obtain the basic non-linear equations that take into account the interaction of nodes in the plane of the discrete rectangular lattice $N_1 \times N_2$. The structure of these equations is similar to the expression (1), but with a different value of the function Q. For a linear fractal dislocation the function Q has the form

$$Q = p_0 - b_1\left((n - n_0)/n_c\right) - b_2\left((m - m_0)/m_c\right); \quad (2)$$

$$b_1 = \cos(\pi/2 + \varphi(j))\,; \quad b_2 = \cos\varphi(j)\,. \quad (3)$$

For other fractal quasi-two-dimensional structures the function Q has the form

$$Q = p_0 - b_1\left((n - n_0)/n_c\right)^2 - b_2\left((m - m_0)/m_c\right)^2, \quad (4)$$

where for the elliptic dislocation and fractal quantum dot

$$b_1 = b_2 = \cos\varphi(j) \quad (5)$$

and in the case of fractal hyperbolic dislocation

$$b_1 = \cos\varphi(j)\,; \quad b_2 = \cos(\pi + \varphi(j))\,. \quad (6)$$

Now here the governing parameters are $p_0, n_0, n_c, m_0, m_c,\ \varphi(j)$. Varying these parameters both a structural state of the self-fractal dislocation and the type of dislocation (for example, the transition from fractal elliptical dislocation to fractal quantum dot) can be governed. In general case the governing parameters can be changed from one node plane to another, which may be connected not only with external governance (for example, when a parameter p_0 is changed), but also with internal governance (the process of self-organization of structures when $\varphi(j)$ is changed). To investigate the behavior of the stochastic deformation field of fractal quasi-two-dimensional structure in terms of the statistical approach, averaged functions are introduced [11]. The necessity of averaging is connected with the fact that the elements of the lattice nodes displacement matrix are in general case random real functions. The average is taken only on nodes in the plane of the discrete rectangular lattice $N_1 \times N_2$. For this the operators fields of displacement $\hat{u}$ and density of states $\hat{\rho}$ are introduced. These operators are coincided to the matrix with the elements of u_{nm}; $\rho_{mn} = 1/N_2 N_1$. Rectangular matrices $\hat{u}$ and $\hat{\rho}$ have the dimensions of $N_1 \times N_2$; $N_2 \times N_1$, respectively. For a homogeneous distribution the operator $\hat{\rho}$ is given by

$$\hat{\rho} = \hat{\xi}_{N2}^T \hat{\xi}_{N1} / N_2 N_1, \tag{7}$$

where «T» denotes transposition; $\hat{\xi}_{N1}$, $\hat{\xi}_{N2}$ are row-vectors with elements equal to one. The averaged function M has the form [11]

$$M = Sp(\hat{\rho}\,\hat{u}) = M' + i\,M''; \quad M' = \mathrm{Re}\,M; \quad M'' = \mathrm{Im}\,M. \tag{8}$$

Here Sp is an operation of calculating the trace of a square matrix; Re, Im represent an allocation of real and imaginary parts of the complex function M; i is an imaginary unit. Averaged function M depends on the governing parameters $p_0(j)$, $\varphi(j)$. In general case $M = M(j)$ is a random function, as an average over the index j is not made. This means that there are some critical values $p_0(j)$, $\varphi(j)$, during the transition through which the behavior of function M can vary from regular to stochastic. Therefore there is a problem of finding the critical values of these governing parameters.

3. Numerical simulation and the analysis of results

Solution of the nonlinear equation (1) with the value of function Q in the form (3) is constructed by the iteration method [11] for fixed values $\alpha = 0,5$; $k = 0,5$; $u_0 = 29,537$. The iterative procedure on the index m simulates a stochastic process on a rectangular discrete lattice with a size $N_1 \times N_2 = 30 \times 40$. The initial parameters were the following: $n_0 = 14,3267$; $n_c = 9,4793$; $m_0 = 19,1471$; $m_c = 14,7295$. In the simulation it was assumed that $\varphi(j) = (j-1)\pi/10$. A separate nodal plane of a model nanosystem can be in different structural states: the state with the linear fractal dislocation of different orientations (Fig. 1); stochastic state of the deformation field on the whole rectangular lattice (Fig. 2. b, Fig. 3. b); quasi-two-dimensional structures of the type of fractal elliptical (Fig. 2. a), hyperbolic dislocations (Fig. 3. a. c) and fractal quantum dot (Fig. 2. c). Governance of alteration (Fig. 1-Fig. 3) of the deformation field is achieved by changing the internal parameters b_1, b_2. At the same time the external parameter $p_0 = 0.1453$ has been fixed and is chosen from the field of stochastic behavior of the averaged function M (Fig. 4-Fig. 6). Rotation of a linear dislocation (Fig. 1) is achieved by governing the internal parameters b_1, b_2 (3) by changing the angle $\varphi(j)$. At rotation there is a change of the structural state of the dislocation and substructures appear, which is related to the influence of the stochastic iteration process along the axis Om. If $\cos\varphi(j) > 0$ the quasi-two-dimensional structure (4), (5) is a structure of the type of fractal elliptical dislocation, for which the location of the singular points is typical for real ellipse. If $\cos\varphi(j) < 0$ the quasi-two-dimensional structure is a structure of the type of the fractal quantum dot [12], for which the location of the singular points is typical for an imaginary ellipse. Fig. 2 show the transition from the elliptic dislocation to the quantum dot through the stochastic state of the whole lattice.

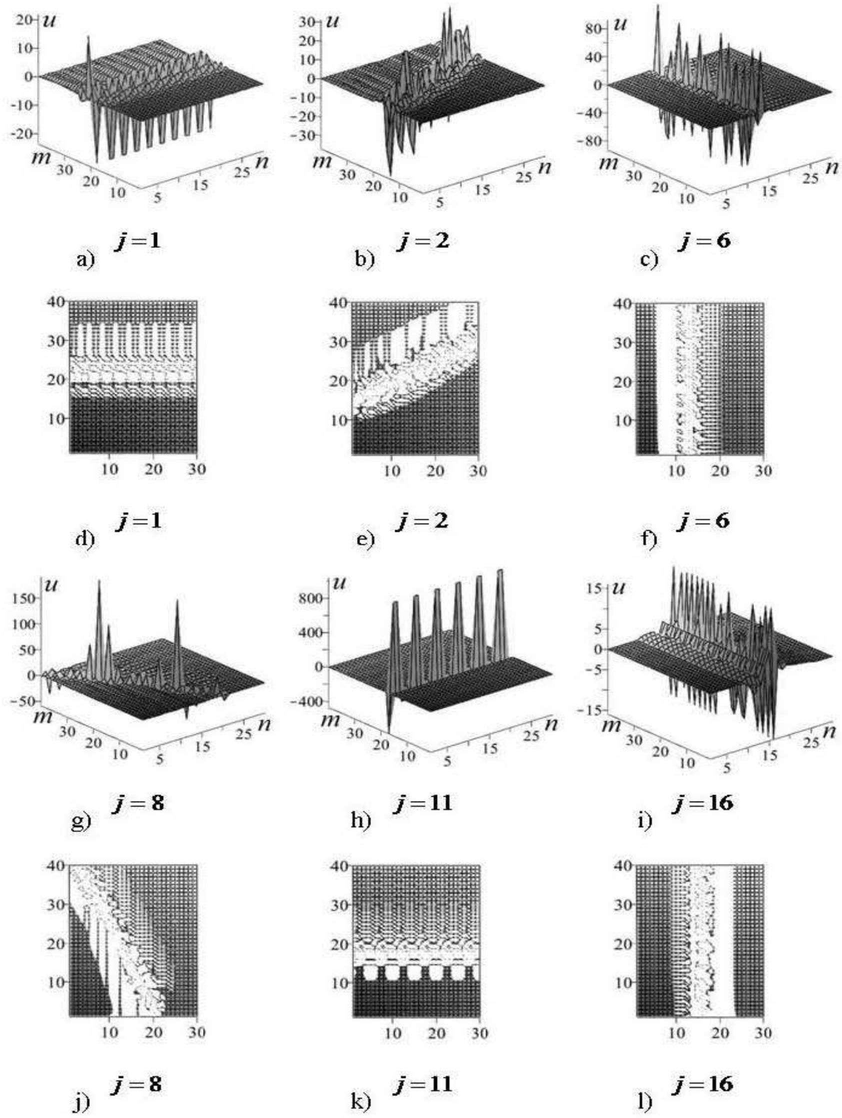

Fig. 1. The behavior of functions u (a,b,c,g,h,i) and their cuts (d,e,f,j,k,l) at $u \in [-0.5, 0.5]$ (top view) depending on the lattice index n and m for linear fractal dislocation

This transition is realized when governing the internal parameters of b_1, b_2 (5) by changing the angle $\varphi(j)$. At the same time a reorientation of the peaks, a change of the substructure, an expansion (at $j \in [1,5]$) and a restriction (at $j \in [17,21]$) of the area of the elliptical dislocation; a restriction (at $j \in [7,11]$) and an expansion (at $j \in [12,15]$) of the area of the quantum dot are observed.

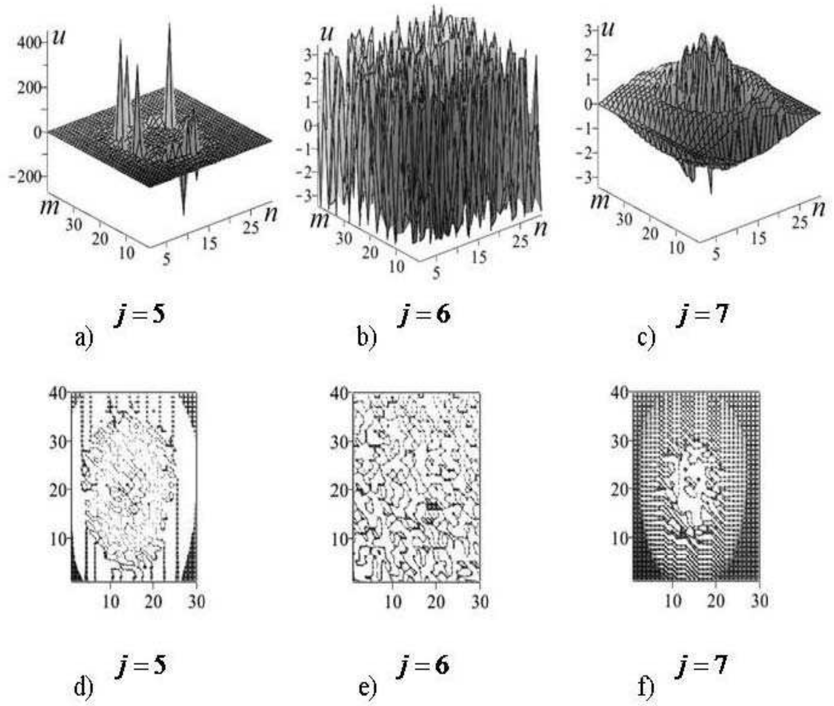

Fig. 2. The transition from the elliptic dislocation to the quantum dot. The behavior of the functions u (a,b,c) and their cuts (d,e,f) at $u \in [-0.5, 0.5]$ (top view) depending on the lattice index n and m

The reorientation of the branches of the fractal hyperbolic dislocation through the stochastic state of the whole lattice is achieved by governing the internal parameters b_1, b_2 from (6) by changing the angle $\varphi(j)$ (Fig. 3). Strongly pronounced stochastic behavior of the deformation field and the substructure can be observed for the region between the branches of the hyperbolic dislocation. The analysis of the behavior of the averaged functions allows to determine the critical values of the governing parameters. In our case, the parameter p_0 is a parameter of the external governance, averaged function M is a real random function. The behavior of function M for the fractal elliptical dislocation ($p_0 > 0$, $b_1 = b_2 = 1$) is shown in Fig. 4. In the interval of $p_0 \in [0;5]$ a base peak (Fig. 4. a) and a stochastic behavior with smaller amplitudes (Fig. 4. b) are observed. The presence of several features (such as local resonance dispersion) allows us to determine the critical values of p_0, during the transition through which the stochastic behavior of M is changed to a regular one(Fig. 4. c). These features allow us to study the mechanism of alteration of fractal quasi-two-dimensional structures of the type of elliptical dislocation. With a further increase in p_0 function M is regular and asymptotically approach to zero from negative values.

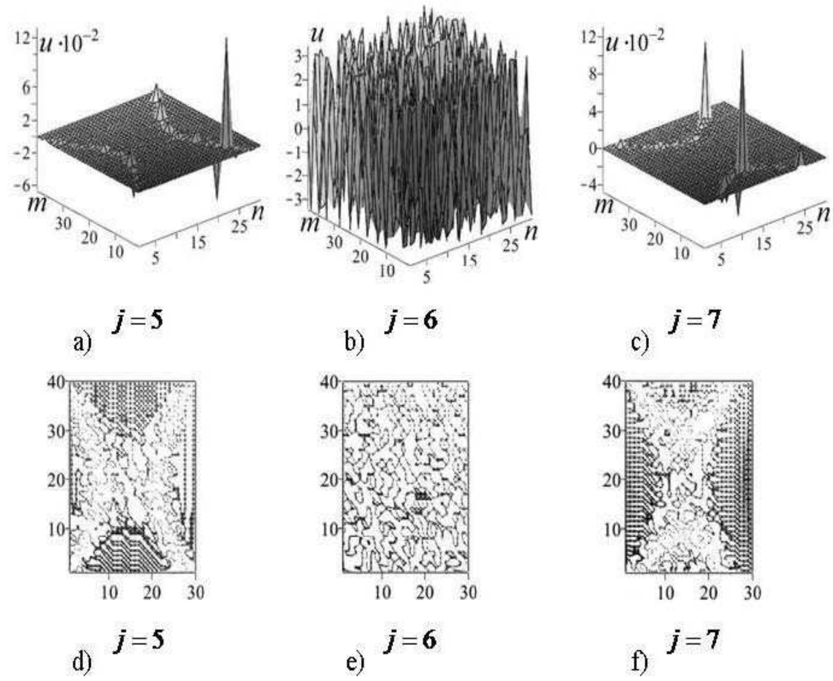

Fig. 3. The reorientation of the branches of the hyperbolic dislocation through the stochastic state. The behavior of the functions u (a,b,c) and their cuts (d,e,f) at $u \in [-0.5, 0.5]$ (top view) depending on the lattice index n and m

The behavior of M for the fractal quantum dot ($p_0 < 0$, $b_1 = b_2 = 1$) is shown in Fig. 5. When changing p_0 the regular behavior of function M (Fig. 5. a) goes into pronounced stochastic (Fig. 5. b). The presence of such features as inflection points, local maxima and minima allows to determine the critical values of the parameter p_0 (Fig. 5. c). The behavior of the function M of the parameter p_0 at $b_1 = -1$, $b_2 = 1$ ($j = 11$) for the fractal hyperbolic dislocation (4), (6) is shown in Fig. 6. By changing p_0 a base peak and two additional peaks (Fig. 6. a) are observed, as well as a pronounced stochastic behavior with smaller amplitudes (Fig. 6. b). The features of the function behavior are given by a type of local inflection points, maxima and minima (as in the quantum dot of Fig. 5. c). This allows to determine the critical value of the parameter p_0, across which the regular behavior of the function M changes to stochastic (Fig. 6. c).

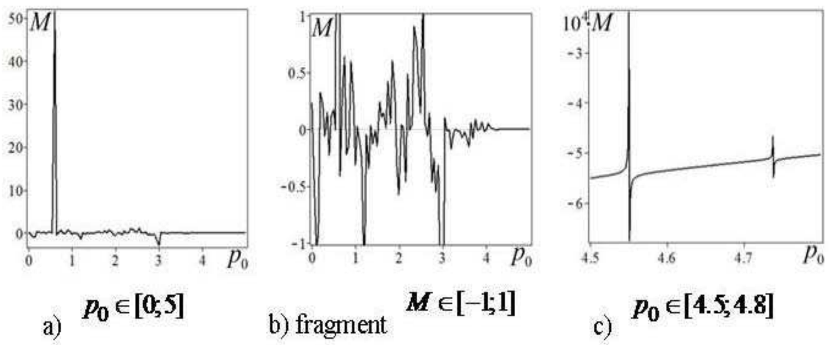

Fig. 4. The behavior of M of p_0 for the elliptic dislocation at $j = 1$

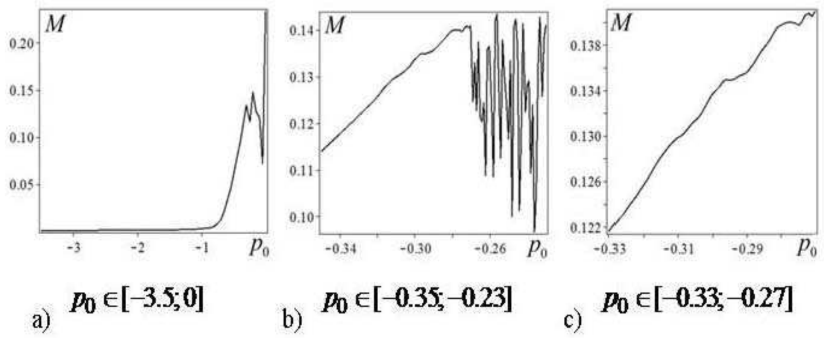

Fig. 5. The behavior of M of p_0 for the fractal quantum dot at $j = 1$

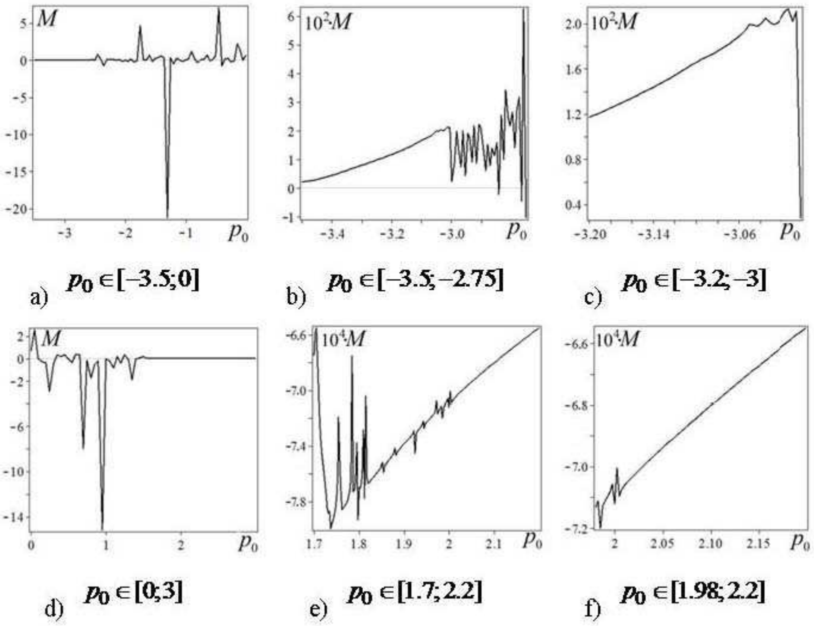

Fig. 6. The behavior of M of p_0 for the hyperbolic dislocation at $j = 11$

By changing the sign of p_0 (Fig. 6. d) there is a change in the orientation of the branches of the fractal hyperbolic dislocation. In this case the features of M have the form of a resonance dispersion type (Fig. 6. e) against the background of the step (Fig. 6. f). This allows to determine the critical value of the parameter p_0, across which the stochastic behavior of M changes to regular.

4. Conclusions

In order to describe stochastic deformation fields of fractal quasi-two-dimensional structures the basic non-linear equations taking into account the interaction of nodes in the plane of the discrete rectangular lattice were obtained. The alteration of the deformation field of fractal quasi-two-dimensional structures is achieved by changing internal and external governing parameters. It is shown that in this case both the structural state of the self-structure and the type of structure vary. The behavior of the averaged functions when changing the governing parameters correlates with the behavior of the deformation field and is related to the mechanisms of alteration of fractal quasi-two-dimensional structures.

References

1. A. Castro Neto, F. Guinea, N. Peres, K. Novoselov, A. Geim. The electronic properties of graphene. *Rev. Mod. Phys.* **81**: 109-162, 2009.
2. L. Tarruell, D. Greif, T. Uehlinger, G. Jotzu, T. Esslinger. Creating, moving and merging Dirac points with a Fermi gas in a tunable honeycomb lattice. *Nature* **483,** 7389: 302-305, 2012.
3. H.-J. Stockmann. *Quantum Chaos.An Introduction*. Cambridge Univers. Press, 1999.
4. M.A Nielsen, I.L. Chuang. *Quantum Computation and Quantum Information.* Cambridge: Cambridge Univ. Press, 2000.
5. S. Alexander, O. Entin-Wohlman, R. Orbach. Relaxation and nonradiative decay in disordered systems. I. One-fracton emission. *Phys. Rev. B.* **32,** 10: 6447-6455, 1985.
6. V.S. Abramov. Fractal dislocation as one of non-classical structural objects in the nano-dimensional systems. *Metallofiz. i Noveishie Tekhnologii*. **33,** 2: 247-251, 2011.
7. O.P. Abramova, S.V. Abramov. Alteration of the structure of the stochastic dislocation deformation field under the change of governing parameters. *Metallofiz. i Noveishie Tekhnologii.* **33,** 4: 519-524, 2011.
8. S.G. Samko, A. Kilbas, O. Marichev. Fractional Integrals and Derivatives. Theory and Applications. Gordon and Breach Sci. Publ., New York et alibi, 1990.
9. B.B. Mandelbrot. *The Fractal Geometry of Nature.* Freeman, New York, 1982.
10. V.S. Abramov. Behavior of the deformation field of fractal dislocation in the presence of bifurcftions. *Bul. of Donetsk Nat. Univers.* Ser. **A,** 2: 23-29, 2011.
11. O.P. Abramova, S.V. Abramov. Deterministic and stochastic governance of the alteration of the fractal dislocation structure. *Bul. of Donetsk Nat. Univers.* Ser. **A,** 2: 30-35, 2011.
12. V.S. Abramov. Inverse structural states of the deformation field of a fractal quantum dot. *Book of Abstracts CHAOS 2012 «5th Chaotic Modeling and Simulation International Conference», 12-15 June 2012 Athens, Greece.* p. 11-12, Greece, 2012.
13. O.P. Abramova, S.V. Abramov. Governing the behaviour of the deformation fields of fractal quasi-two-dimensional structures. *Book of Abstracts CHAOS 2012 «5th Chaotic Modeling and Simulation International Conference», 12-15 June 2012 Athens, Greece.* p. 12-13, Greece, 2012.

Chaotic Modeling and Simulation (CMSIM) 3: 377–385, 2013

New Criteria for Generalized Synchronization Preserving the Chaos Type

M. U. Akhmet[1] and M. O. Fen[2]

[1] Department of Mathematics, Middle East Technical University, 06800, Ankara, Turkey
(E-mail: marat@metu.edu.tr)
[2] Department of Mathematics, Middle East Technical University, 06800, Ankara, Turkey
(E-mail: ofen@metu.edu.tr)

Abstract. We provide new conditions for the presence of generalized synchronization in unidirectionally coupled systems. One of the main results in the paper is the preservation of the chaos type of the drive system. The analysis is based on the Devaney definition of chaos. Appropriate simulations which illustrate the generalized synchronization are depicted.
Keywords: Generalized synchronization, Devaney chaos, Chaotic set of functions.

1 Introduction

The most general ideas about the synchronization of different chaotic systems with an unrestricted form of coupling can be found in paper [1]. Rulkov et al. [2] realized this proposal by introducing the concept of generalized synchronization (GS) for unidirectionally coupled systems. The concept of GS [2]-[5] characterizes the dynamics of a response system that is driven by the output of a chaotic driving one.

In the present paper, the drive system will be considered in the following form

$$x' = F(x), \tag{1}$$

where $F : \mathbb{R}^m \to \mathbb{R}^m$ is a continuous function, and the response is assumed to have the form

$$y' = Ay + g(x, y), \tag{2}$$

where $g : \mathbb{R}^m \times \mathbb{R}^n \to \mathbb{R}^n$ is a continuous function in all its arguments and the constant $n \times n$ real valued matrix A has real parts of eigenvalues all negative. We assume that system (1) admits a chaotic attractor.

Received: 3 April 2013 / Accepted: 15 July 2013

ISSN 2241-0503

GS is said to occur if there exist sets I_x, I_y of initial conditions and a transformation $\varphi : \mathbb{R}^m \to \mathbb{R}^n$, defined on the chaotic attractor of the drive system, such that for all $x(0) \in I_x$, $y(0) \in I_y$ the relation $\lim_{t\to\infty} \|y(t) - \varphi(x(t))\| = 0$ holds. In this case, a motion which starts on $I_x \times I_y$ collapses onto a manifold $M \subset I_x \times I_y$ of synchronized motions. The transformation φ is not required to exist for the transient trajectories [2,3].

According to the results of [3], GS occurs if and only if for all $x_0 \in I_x$, $y_{10}, y_{20} \in I_y$, the following criterion holds:

(A) $\lim\limits_{t\to\infty} \|y(t, x_0, y_{10}) - y(t, x_0, y_{20})\| = 0,$

where $y(t, x_0, y_{10}), y(t, x_0, y_{20})$ denote the solutions of (2) corresponding to the initial data $y(0, x_0, y_{10}) = y_{10}$, $y(0, x_0, y_{20}) = y_{20}$ with the same $x(t)$, $x(0) = x_0$.

A consequence of GS is the ability to predict the behavior of $y(t)$, based on the knowledge of $x(t)$ and φ only. If φ is invertible $x(t)$ is also predictable from $y(t)$. The usage of statistical estimations of predictability [2], analysis of conditional Lyapunov exponents [3] and the auxiliary system approach [4] are the main approaches to the observation of GS.

Let us introduce the ingredients of Devaney chaos [6] for continuous time dynamics. Denote by

$$\mathscr{B} = \{\psi(t) \mid \psi : \mathbb{R} \to K \text{ is continuous}\}$$

a collection of functions, where $K \subset \mathbb{R}^q$ is a bounded region.

We say that $\mathscr{B}$ is sensitive if there exist positive numbers ϵ and Δ such that for every $\psi(t) \in \mathscr{B}$ and for arbitrary $\delta > 0$ there exist $\overline{\psi}(t) \in \mathscr{B}$, $t_0 \in \mathbb{R}$ and an interval $J \subset [t_0, \infty)$, with length not less than Δ, such that $\left\|\psi(t_0) - \overline{\psi}(t_0)\right\| < \delta$ and $\left\|\psi(t) - \overline{\psi}(t)\right\| > \epsilon$, for all $t \in J$.

On the other hand, the collection $\mathscr{B}$ is said to possess a dense function $\psi^*(t) \in \mathscr{B}$ if for every $\psi(t) \in \mathscr{B}$, arbitrary small $\epsilon > 0$ and arbitrary large $E > 0$, there exist a number $\xi > 0$ and an interval $J \subset \mathbb{R}$, with length E, such that $\|\psi(t) - \psi^*(t + \xi)\| < \epsilon$, for all $t \in J$. We say that $\mathscr{B}$ is transitive if it possesses a dense function.

Furthermore, $\mathscr{B}$ admits a dense collection $\mathscr{G} \subset \mathscr{B}$ of periodic functions if for every function $\psi(t) \in \mathscr{B}$, arbitrary small $\epsilon > 0$ and arbitrary large $E > 0$, there exist $\widetilde{\psi}(t) \in \mathscr{G}$ and an interval $J \subset \mathbb{R}$, with length E, such that $\left\|\psi(t) - \widetilde{\psi}(t)\right\| < \epsilon$, for all $t \in J$.

The collection $\mathscr{B}$ is called a Devaney chaotic set if: (i) $\mathscr{B}$ is sensitive; (ii) $\mathscr{B}$ is transitive; (iii) $\mathscr{B}$ admits a dense collection of periodic functions.

We present two main results in the paper. The first one is the the occurrence of GS in system (1)+(2), and the second one is the preservation of the chaos type of the drive system. The GS is verified in the next section by means of the criterion (A). The third section is devoted for the presence of Devaney chaos in the response system. Moreover, an example that supports our theoretical discussions is presented in the last section.

2 Preliminaries

Throughout the paper, the uniform norm $\|\Gamma\| = \sup_{\|v\|=1} \|\Gamma v\|$ for matrices will be used.

Since the matrix A, which is aforementioned in system (2), is supposed to admit eigenvalues all with negative real parts, there exist positive real numbers N and ω such that $\left\|e^{At}\right\| \leq Ne^{-\omega t}$, $t \geq 0$. These numbers will be used in the last condition below.

The following assumptions on systems (1) and (2) are needed throughout the paper:

(A1) There exists a number $H_0 > 0$ such that $\sup\limits_{x\in\mathbb{R}^m} \|F(x)\| \leq H_0$;
(A2) There exists a number $L_0 > 0$ such that $\|F(x_1) - F(x_2)\| \leq L_0 \|x_1 - x_2\|$, for all $x_1, x_2 \in \mathbb{R}^m$;
(A3) There exists a number $M_0 > 0$ such that $\sup\limits_{x\in\mathbb{R}^m, y\in\mathbb{R}^n} \|g(x,y)\| \leq M_0$;
(A4) There exist numbers $L_1 > 0$ and $L_2 > 0$ such that

$$L_1 \|x_1 - x_2\| \leq \|g(x_1, y) - g(x_2, y)\| \leq L_2 \|x_1 - x_2\|,$$

for all $x_1, x_2 \in \mathbb{R}^m$, $y \in \mathbb{R}^n$;
(A5) There exists a number $L_3 > 0$ such that

$$\|g(x, y_1) - g(x, y_2)\| \leq L_3 \|y_1 - y_2\|,$$

for all $x \in \mathbb{R}^m$, $y_1, y_2 \in \mathbb{R}^n$;
(A6) $NL_3 - \omega < 0$.

Using the technique presented in the book [7], for a given solution $x(t)$ of system (1), one can verify the existence of a unique bounded on $\mathbb{R}$ solution $\phi_{x(t)}(t)$ of the system $y' = Ay + g(x(t), y)$, which satisfies the following integral equation

$$\phi_{x(t)}(t) = \int_{-\infty}^{t} e^{A(t-s)} g(x(s), \phi_{x(t)}(s)) ds. \tag{3}$$

Our main assumption is the existence of a nonempty set $\mathscr{A}_x$ of all solutions of system (1), uniformly bounded on $\mathbb{R}$. That is, there exists a positive real number H such that $\sup_{t\in\mathbb{R}} \|x(t)\| \leq H$, for all $x(t) \in \mathscr{A}_x$.

Let us introduce the following set of functions

$$\mathscr{A}_y = \left\{\phi_{x(t)}(t) \mid x(t) \in \mathscr{A}_x\right\}.$$

We note that for all $y(t) \in \mathscr{A}_y$ one has $\sup_{t\in\mathbb{R}} \|y(t)\| \leq M$, where $M = NM_0/\omega$. Moreover, if $x(t) \in \mathscr{A}_x$ is periodic then $\phi_{x(t)}(t) \in \mathscr{A}_y$ is periodic with the same period, and vice versa.

Next, we will reveal that if the set $\mathscr{A}_x$ is an attractor with basin $\mathscr{U}_x$, that is, for each $x(t) \in \mathscr{U}_x$ there exists $\overline{x}(t) \in \mathscr{A}_x$ such that $\|x(t) - \overline{x}(t)\| \to 0$ as $t \to \infty$, then the set $\mathscr{A}_y$ is also an attractor in the same sense. In the following lemma we specify the basin of attraction of $\mathscr{A}_y$.

Suppose that the set $\mathscr{U}_y$ consists of solutions of the system $y' = Ay + g(x(t), y)$, where $x(t)$ belongs to $\mathscr{U}_x$.

Lemma 1. *$\mathscr{U}_y$ is a basin of $\mathscr{A}_y$.*

Proof. Fix an arbitrary $\epsilon > 0$ and let $y(t) \in \mathscr{U}_y$. There exists $\overline{x}(t) \in \mathscr{A}_x$ such that $\|x(t) - \overline{x}(t)\| \to 0$ as $t \to \infty$. Set $\alpha = \frac{\omega - NL_3}{\omega - NL_3 + NL_2}$ and $\overline{y}(t) = \phi_{\overline{x}(t)}(t)$. One can find $R_0 = R_0(\epsilon) > 0$ such that if $t \geq R_0$ then $\|x(t) - \overline{x}(t)\| < \alpha\epsilon$ and $N\|y(R_0) - \overline{y}(R_0)\| e^{(NL_3-\omega)t} < \alpha\epsilon$. Using the equation

$$
\begin{aligned}
y(t) - \overline{y}(t) &= e^{A(t-R_0)}(y(R_0) - \overline{y}(R_0)) \\
&+ \int_{R_0}^{t} e^{A(t-s)} \left[g(x(s), y(s)) - g(x(s), \overline{y}(s))\right] ds \\
&+ \int_{R_0}^{t} e^{A(t-s)} \left[g(x(s), \overline{y}(s)) - g(\overline{x}(s), \overline{y}(s))\right] ds,
\end{aligned}
$$

we obtain for $t \geq R_0$ that

$$
\begin{aligned}
&e^{\omega t}\|y(t) - \overline{y}(t)\| \leq Ne^{\omega R_0}\|y(R_0) - \overline{y}(R_0)\| + \frac{NL_2\alpha\epsilon}{\omega}\left(e^{\omega t} - e^{\omega R_0}\right) \\
&+NL_3 \int_{R_0}^{t} e^{\omega s}\|y(s) - \overline{y}(s)\| ds.
\end{aligned}
$$

Applying Gronwall's inequality we attain that

$$
\begin{aligned}
&e^{\omega t}\|y(t) - \overline{y}(t)\| \leq \frac{NL_2\alpha\epsilon}{\omega}e^{\omega t} + N\|y(R_0) - \overline{y}(R_0)\| e^{\omega R_0} e^{NL_3(t-R_0)} \\
&-\frac{NL_2\alpha\epsilon}{\omega}e^{\omega R_0}e^{NL_3(t-R_0)} + \frac{N^2L_2L_3\alpha\epsilon}{\omega(\omega - NL_3)}e^{\omega t}\left(1 - e^{(NL_3-\omega)(t-R_0)}\right).
\end{aligned}
$$

Thus, we have

$$
\|y(t) - \overline{y}(t)\| < N\|y(R_0) - \overline{y}(R_0)\| e^{(NL_3-\omega)(t-R_0)} + \frac{NL_2\alpha\epsilon}{\omega - NL_3}, \ t \geq R_0.
$$

For $t \geq 2R_0$, one can show that $\|y(t) - \overline{y}(t)\| < \left(1 + \frac{NL_2}{\omega - NL_3}\right)\alpha\epsilon = \epsilon$. Consequently, $\|y(t) - \overline{y}(t)\| \to 0$ as $t \to \infty$. $\square$

One can verify using Lemma 1 that for a fixed $x(t) \in \mathscr{U}_x$, any two solutions $y(t), \overline{y}(t)$ of the system $y' = Ay + g(x(t), y)$ satisfy the criterion (A). Therefore, we have the following theorem.

Theorem 1. *GS occurs in the coupled system (1)+(2).*

3 The chaotic dynamics

We will prove that if the drive system (1) is Devaney chaotic then the response system (2) is also chaotic in the same sense. The three ingredients of Devaney chaos will be considered individually. We start with sensitivity in the next lemma.

Lemma 2. *Sensitivity of the set $\mathscr{A}_x$ implies the same feature for the set $\mathscr{A}_y$.*

Proof. Fix an arbitrary $\delta > 0$ and $y(t) \in \mathscr{A}_y$. There exists $x(t) \in \mathscr{A}_x$ such that $y(t) = \phi_{x(t)}(t)$. Choose a sufficiently small number $\overline{\epsilon} = \overline{\epsilon}(\delta) > 0$ such that $\left(1 + \frac{NL_2}{\omega - NL_3}\right)\overline{\epsilon} < \delta$, and take $R = R(\overline{\epsilon}) < 0$ sufficiently large in absolute value such that $\frac{2M_0N}{\omega} e^{(\omega - NL_3)R} < \overline{\epsilon}$. Set $\delta_1 = \delta_1(\overline{\epsilon}, R) = \overline{\epsilon} e^{L_0 R}$. Since $\mathscr{A}_x$ is sensitive, there exist $\epsilon_0 > 0$, $\Delta > 0$ such that $\|x(t_0) - \overline{x}(t_0)\| < \delta_1$ and $\|x(t) - \overline{x}(t)\| > \epsilon_0$, $t \in J$, for some $\overline{x}(t) \in \mathscr{A}_x$, $t_0 \in \mathbb{R}$ and for some interval $J \subset [t_0, \infty)$ whose length is not less than Δ.

By means of continuous dependence on initial conditions, one can verify that $\|x(t) - \overline{x}(t)\| < \overline{\epsilon}$, $t \in [t_0 + R, t_0]$. Denote $\overline{y}(t) = \phi_{\overline{x}(t)}(t)$. Using the relation (3) for both $y(t)$ and $\overline{y}(t)$, we obtain for $t \in [t_0 + R, t_0]$ that

$$\begin{aligned} e^{\omega t}\|y(t) - \overline{y}(t)\| &\le NL_3 \int_{t_0+R}^{t} e^{\omega s}\|y(s) - \overline{y}(s)\|\, ds \\ &+ \frac{NL_2\overline{\epsilon}}{\omega}(e^{\omega t} - e^{\omega(t_0+R)}) + \frac{2M_0N}{\omega} e^{\omega(t_0+R)}. \end{aligned}$$

Applying Gronwall's Lemma to the last inequality we attain that

$$\|y(t) - \overline{y}(t)\| \le \frac{NL_2\overline{\epsilon}}{\omega - NL_3} + \frac{2M_0N}{\omega} e^{(NL_3-\omega)(t-t_0-R)},\ t \in [t_0 + R, t_0].$$

Consequently, we have $\|y(t_0) - \overline{y}(t_0)\| \le \frac{NL_2\overline{\epsilon}}{\omega - NL_3} + \frac{2M_0N}{\omega} e^{(\omega - NL_3)R} < \delta$.

Next, we will show the existence of a positive numbers ϵ_1, $\overline{\Delta}$ and an interval $J^1 \subset J$ with length $\overline{\Delta}$ such that the inequality $\|y(t) - \overline{y}(t)\| > \epsilon_1$ holds for all $t \in J^1$.

Suppose that $g(x, y) = (g_1(x, y), g_2(x, y), \ldots, g_n(x, y))$, where each g_j, $1 \le j \le n$, is a real valued function.

Since $\mathscr{A}_x$ and $\mathscr{A}_y$ are both equicontinuous on $\mathbb{R}$, and the function $\overline{g} : \mathbb{R}^m \times \mathbb{R}^m \times \mathbb{R}^n \to \mathbb{R}^n$ defined as $\overline{g}(x_1, x_2, x_3) = g(x_1, x_3) - g(x_2, x_3)$ is uniformly continuous on the compact region

$$\mathscr{D} = \{(x_1, x_2, x_3) \in \mathbb{R}^m \times \mathbb{R}^m \times \mathbb{R}^n \mid \|x_1\| \le H, \|x_2\| \le H, \|x_3\| \le M\},$$

the set $\mathscr{F}$ with elements of the form $g_j(x(t), \phi_{x(t)}(t)) - g_j(\overline{x}(t), \phi_{x(t)}(t))$, $1 \le j \le n$, where $x(t), \overline{x}(t) \in \mathscr{A}_x$, is an equicontinuous family on $\mathbb{R}$. Therefore, there exists a positive number $\tau < \Delta$, independent of $x(t), \overline{x}(t) \in \mathscr{A}_x$, $y(t), \overline{y}(t) \in \mathscr{A}_y$, such that for any $t_1, t_2 \in \mathbb{R}$ with $|t_1 - t_2| < \tau$ the inequality

$$\begin{aligned} &|(g_j(x(t_1), y(t_1)) - g_j(\overline{x}(t_1), y(t_1))) - (g_j(x(t_2), y(t_2)) - g_j(\overline{x}(t_2), y(t_2)))| \\ &< \frac{L_1\epsilon_0}{2n} \end{aligned} \tag{4}$$

holds, for all $1 \le j \le n$.

Condition $(A4)$ implies that for each $t \in J$, there exists an integer $j_0 = j_0(t)$, $1 \le j_0 \le n$, such that $|g_{j_0}(x(t), y(t)) - g_{j_0}(\overline{x}(t), y(t))| \ge \dfrac{L_1}{n}\|x(t) - \overline{x}(t)\|$.

Let s_0 be the midpoint of the interval J and $\theta = s_0 - \tau/2$. One can find an integer $j_0 = j_0(s_0)$, $1 \le j_0 \le n$, such that

$$|g_{j_0}(x(s_0), y(s_0)) - g_{j_0}(\overline{x}(s_0), y(s_0))| \ge \frac{L_1}{n}\|x(s_0) - \overline{x}(s_0)\| > \frac{L_1\epsilon_0}{n}. \tag{5}$$

According to (4), for all $t \in [\theta, \theta+\tau]$ we obtain that

$$|g_{j_0}(x(s_0), y(s_0)) - g_{j_0}(\overline{x}(s_0), y(s_0))| - |g_{j_0}(x(t), y(t)) - g_{j_0}(\overline{x}(t), y(t))| < \frac{L_1 \epsilon_0}{2n}$$

and therefore by means of (5), the following inequality:

$$|g_{j_0}(x(t), y(t)) - g_{j_0}(\overline{x}(t), y(t))| > \frac{L_1 \epsilon_0}{2n},\ t \in [\theta, \theta+\tau].$$

The last inequality implies that

$$\left\| \int_\theta^{\theta+\tau} [g(x(s), y(s)) - g(\overline{x}(s), y(s))]\, ds \right\| > \frac{\tau L_1 \epsilon_0}{2n}.$$

Therefore, we have

$$\begin{aligned} &\max_{t \in [\theta, \theta+\tau]} \|y(t) - \overline{y}(t)\| \geq \|y(\theta+\tau) - \overline{y}(\theta+\tau)\| \\ &> \frac{\tau L_1 \epsilon_0}{2n} - [1 + \tau(L_3 + \|A\|)] \max_{t \in [\theta, \theta+\tau]} \|y(t) - \overline{y}(t)\|, \end{aligned}$$

and hence, $\max_{t \in [\theta, \theta+\tau]} \|y(t) - \overline{y}(t)\| > \dfrac{\tau L_1 \epsilon_0}{2n[2 + \tau(L_3 + \|A\|)]}$.

Now, suppose that at the point $\eta \in [\theta, \theta+\tau]$, the function $\|y(t) - \overline{y}(t)\|$ takes its maximum. Define $\overline{\Delta} = \min\left\{ \dfrac{\tau}{2}, \dfrac{\tau L_1 \epsilon_0}{8n(M\|A\| + M_0)[2 + \tau(L_3 + \|A\|)]} \right\}$ and $\theta^1 = \begin{cases} \eta, & \text{if } \eta \leq \theta + \tau/2 \\ \eta - \overline{\Delta}, & \text{if } \eta > \theta + \tau/2 \end{cases}$. For $t \in J^1 = [\theta^1, \theta^1 + \overline{\Delta}]$, we have

$$\begin{aligned} &\|y(t) - \overline{y}(t)\| \geq \|y(\eta) - \overline{y}(\eta)\| - \left| \int_\eta^t \|A\| \, \|y(s) - \overline{y}(s)\|\, ds \right| \\ &- \left| \int_\eta^t \|g(x(s), y(s)) - g(\overline{x}(s), \overline{y}(s))\|\, ds \right| \\ &> \frac{\tau L_1 \epsilon_0}{4n[2 + \tau(L_3 + \|A\|)]}. \end{aligned}$$

Consequently, $\|y(t) - \overline{y}(t)\| > \epsilon_1$, $t \in J^1$, where $\epsilon_1 = \frac{\tau L_1 \epsilon_0}{4n[2+\tau(L_3+\|A\|)]}$ and the length of the interval J^1 does not depend on the functions $y(t), \overline{y}(t) \in \mathscr{A}_y$. $\square$

Lemma 3. *Transitivity of $\mathscr{A}_x$ implies the same feature for $\mathscr{A}_y$.*

Proof. Fix arbitrary numbers $\epsilon > 0$, $E > 0$, and $y(t) \in \mathscr{A}_y$. There exists a function $x(t) \in \mathscr{A}_x$ such that $y(t) = \phi_{x(t)}(t)$. Let $\gamma = \frac{\omega(\omega - NL_3)}{2M_0N(\omega - NL_3) + NL_2\omega}$. Since there exists a dense solution $x^*(t) \in \mathscr{A}_x$, one can find $\xi > 0$ and an interval $J \subset \mathbb{R}$ with length E such that $\|x(t) - x^*(t+\xi)\| < \gamma\epsilon$, for all $t \in J$. Without loss of generality, assume that J is a closed interval, that is, $J = [a, a+E]$ for some real number a. Denote $y^*(t) = \phi_{x^*(t)}(t)$.

Making use of the integral equation (3) for both $y(t)$ and $y^*(t)$, one can verify for $t \in J$ that

$$e^{\omega t} \|y(t) - y^*(t+\xi)\| \leq \frac{2M_0 N}{\omega} e^{\omega a} + \frac{N L_2 \gamma \epsilon}{\omega} \left(e^{\omega t} - e^{\omega a}\right)$$
$$+ N L_3 \int_a^t e^{\omega s} \|y(s) - y^*(s+\xi)\| \, ds.$$

Application of Gronwall's Lemma to the last inequality implies that

$$\|y(t) - y^*(t+\xi)\| \leq \frac{2M_0 N}{\omega} e^{(NL_3 - \omega)(t-a)} + \frac{N L_2 \gamma \epsilon}{\omega - N L_3} \left(1 - e^{(NL_3-\omega)(t-a)}\right).$$

Suppose that $E > \frac{2}{\omega - NL_3} \ln\left(\frac{1}{\gamma\epsilon}\right)$. If $t \in J_1 = \left[a + \frac{E}{2}, a + E\right]$, then it is true that $e^{(NL_3-\omega)(t-a)} < \gamma\epsilon$. Consequently, we have $\|y(t) - y^*(t+\xi)\| < \left[\frac{2M_0 N}{\omega} + \frac{NL_2}{\omega - NL_3}\right] \gamma\epsilon = \epsilon$, for $t \in J_1$. Thus, the set $\mathscr{A}_y$ is transitive. $\square$

In a similar way to Lemma 3 one can prove the following assertion.

Lemma 4. *If $\mathscr{A}_x$ admits a dense collection of periodic functions, then the same is true for $\mathscr{A}_y$.*

The following theorem can be proved using Lemmas 2-4.

Theorem 2. *If the set $\mathscr{A}_x$ is Devaney's chaotic, then the same is true for the set $\mathscr{A}_y$.*

In the next part, we will present an example which supports our theoretical discussions. The usual Euclidean norm for vectors and the norm induced by the Euclidean norm for square matrices will be used.

4 An example

We consider the Lorenz equations [8]

$$\begin{aligned} x_1' &= 10\left(-x_1 + x_2\right) \\ x_2' &= -x_2 + 28x_1 - x_1 x_3 \\ x_3' &= -\frac{8}{3} x_3 + x_1 x_2, \end{aligned} \tag{6}$$

as the drive system. It is known that system (6) admits sensitivity and possesses infinitely many unstable periodic solutions [8]. The equations for the response system are chosen as

$$\begin{aligned} y_1' &= -2y_1 - y_3 + 0.003 y_2^2 + x_2 - \frac{1}{2} \cos x_2 \\ y_2' &= -y_1 - 2y_2 + 5x_1 + 0.01 x_1^3 \\ y_3' &= y_1 - y_2 - 3y_3 + 2 \tan\left(\frac{x_3 + y_2}{120}\right). \end{aligned} \tag{7}$$

System (7) is in the form of (2), where $A = \begin{pmatrix} -2 & 0 & -1 \\ 1 & -1 & -3 \\ 0 & 0 & 0 \end{pmatrix}$. The inequality $\left\| e^{At} \right\| \leq N e^{-\omega t}$ is valid, where $N = 4.829$ and $\omega = 2$. One can verify that conditions $(A4) - (A6)$ are satisfied with constants $L_1 = \sqrt{3}/180$, $L_2 = 17\sqrt{3}$ and $L_3 = 16\sqrt{3}/75$.

According to the results of the present study, system (7) exhibits GS, saving the sensitivity feature of the drive and the existence of infinitely many unstable periodic solutions. Consider a trajectory of system (6)+(7) with $x_1(0) = 0.11$, $x_2(0) = 0.96$, $x_3(0) = 18.98$, $y_1(0) = -0.69$, $y_2(0) = -11.09$, $y_3(0) = 1.96$. Figure 1 shows the projections of this trajectory on the $y_1 - y_2 - y_3$ space, and supports the theoretical results such that the response system (7) possesses chaotic motions. According to the GS, the attractor shown in Figure 1, (a) is a nonlinear image of the chaotic attractor of system (6). Figure 1, (b), on the other hand, depicts the projection on the $x_2 - y_2$ plane, and reveals that the systems are not synchronized in the sense of identical synchronization [9].

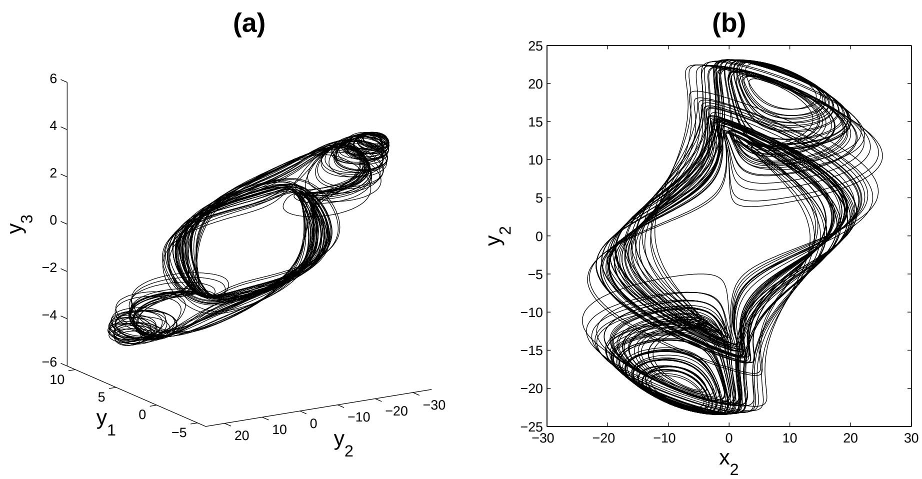

Fig. 1. The projections of the chaotic attractor generated by the coupled system (6)+(7). (a) Projection on the $y_1 - y_2 - y_3$ space; (b) Projection on the $x_2 - y_2$ plane. The pictures represent the synchronized behavior.

References

1. V.S. Afraimovich, N.N. Verichev and M.I. Rabinovich. Stochastic synchronization of oscillation in dissipative systems. Radiophys. Quantum Electron., 29:795-803, 1986.
2. N.F. Rulkov, M.M. Sushchik, L.S. Tsimring and H.D.I. Abarbanel. Generalized synchronization of chaos in directionally coupled chaotic systems. Phys. Rev. E, 51:980-994, 1995.

3.L. Kocarev and U. Parlitz. Generalized synchronization, predictability, and equivalence of unidirectionally coupled dynamical systems. Phys. Rev. Lett., 76:1816-1819, 1996.
4.H.D.I. Abarbanel, N.F. Rulkov and M.M. Sushchik. Generalized synchronization of chaos: The auxiliary system approach. Phys. Rev. E, 53:4528-4535, 1996.
5.J.M. Gonzales-Miranda. Synchronization and Control of Chaos. Imperial College Press, London, 2004.
6.R. Devaney. An Introduction to Chaotic Dynamical Systems. Addison-Wesley, United States of America, 1987.
7.J.K. Hale. Ordinary Differential Equations. Krieger Publishing Company, Malabar, Florida, 1980.
8.E.N. Lorenz. Deterministic nonperiodic flow. J. Atmos. Sci, 20:130-141, 1963.
9.L.M. Pecora and T.L. Carroll. Synchronization in chaotic systems. Phys. Rev. Lett., 64:821-825, 1990.

Chaotic Modeling and Simulation (CMSIM) 3: 387-394 , 2013

Wavelet Analysis of the Human Brain Lability to Reproduce the External Rhythm

Olga E. Dick

Pavlov Institute of Physiology of Russian Academy of Science, St. Petersburg, Russia
E-mail: glazov.holo@mail.ioffe.ru

Abstract: The task is to evaluate the differences in the human brain lability involving its opportunity to forget or reproduce the external rhythm for patients with neural disorders connected with disruptions of the thalamo-cortical or stem-cortical links. For solving the task the EEG segments before, during and after periodic light stimulation are examined by the wavelet transform method. The degree of the human brain lability is estimated by changing in the maximums of the global wavelet spectra and by the coefficients of reproduction and holding the rhythm. Maximal reproduction of the external frequency is observed in the ranges specific for the both groups of the patients. For the patients with stem-cortical disruptions the all parameters essentially differ from the parameters obtained for the patients with thalamo-cortical disorders. Thus, the study demonstrates the possibility of the wavelet analysis to estimate quantitatively the human brain lability of perception of light stimuli.
Keywords: EEG, Wavelet transform, Reproduction of external rhythm.

1. Introduction

Bioelectrical activity of the human brain recorded from the head surface as electroencephalography time series (EEG) during solving the complex imaginary and real visual-motor tasks or during awake and various sleep stages in healthy state exhibits nonstationary, chaotic and multifractal dynamics [1, 2, 3]. The comparative analysis of the dynamics in EEG patterns of normal and pathological brain activities is one of the tools of elucidation of the degree the brain seizures [4, 5] and estimation of the efficiency of the drug or psychological treatment [6]. Photostimultaion, that is the light stimulation of the given frequency, is one of the functional probes applied for determining of the human brain lability to reproduce or to reject the suggested rhythm [7]. The degree of such lability characterizes the level of nerve excitability and can classify persons for whom drugs hyperactivating the nervours system are unsuitable due to their own hyperexcitability.

The aim of the work is to evaluate the differences in the potentialities of the human brain to forget or reproduce the external light rhythm for patients with chronic pain complaints rather resistant to medicinal treatment. These patients can be divided into two groups accordingly to the classification connected with the disruptions on the thalamic level or on the brain-stem level that leads as a

Received: 7 April 2013 / Accepted: 15 July 2013

ISSN 2241-0503

rule to changing the thalamo–cortical links in the first case and the stem–cortical links in the second case [8]. It results to the significant suppression of the alpha component prevailing for the healthy persons and the emergence of the theta acitivity or occurrence of polymorphous small amplitude activity, that is, to essential deviation from the healthy EEG patterns.

2. Experimental procedure

The scalp EEG data were recorded with Ag/AgCl electrodes from 10 healthy subjects and 16 patients with neural impairments connected with chronic pain complaints. Signals of reproducing the light rhythm propagate symmetrically and have maximal amplitude in the occipital lobes of the human brain, that is why the data were collected with electrodes placed at the occipital O1, O2, Oz sites. The recordings were obtained for three states: before the light rhythmic stimulation (the interval $[0, t_A]$), during it (the interval $[t_A, t_B]$) and during relaxation (the interval $[t_B, t_K]$) with eyes closed. The duration of each interval was 20 seconds. The data were sampled at a rate 256 samples/sec with a resolution of 12 bits/sample. Then the data were digitally filtered using 1–30 Hz band pass filter. After repeated recordings 60 non- artifact segments of equal duration were randomly chosen from the sets: “before stimulus”, “during stimulus” and “during relaxation”.

3. Estimation of the global energy of the EEG segment

To estimate the global energy of EEG segment we applied the continuous wavelet transform of a time series x(t):

$$W(a,t_0) = \frac{1}{a}\int_{-\infty}^{+\infty} x(t)\psi^*\left(\frac{t-t_0}{a}\right)dt,$$

where a and t_0 are the scale and space parameters, $\psi((t- t_0)/a)$ is the wavelet function obtained from the basic wavelet $\psi(t)$ by scaling and shifting along the time, symbol * means the complex conjugate. As the basic wavelet we use the complex Morlet wavelet:

$$\psi(t) = D\exp(-0.5t^2)[\exp(-i\omega_0 t) - \exp(-0.5\omega_0^2)],$$

$$D = \frac{\pi^{-1/4}}{\sqrt{1-2\exp(-0.75\omega_0^2)+\exp(-\omega_0^2)}}.$$

The value $\omega_0=2\pi$ gives the simple relation between the scale a and frequency f: $f=1/a$.

The square of the modulus $|W(f, t_0)|^2$ characterizes the instantaneous distribution of energy over frequencies at the time t_0, that is, the local spectrum of the signal energy.
The value

$$E(f) = \int_{t_1}^{t_2} |W(f,t_0)|^2 dt_0$$

describes the global wavelet spectrum, i.e., the integral of energy distribution over frequency range on the interval $[t_1, t_2]$.
The value

$$E(t_0) = \int_{f_1}^{f_2} |W(f,t_0)|^2 df$$

represents the integral of energy distribution over time shifts in the frequency range $[f_1, f_2]$.

4. The light time series

The light time series limited on the interval $[t_A, t_B]$ was described as a sequence of k Gauss impulses following each other with frequency f_C equal to 4, 6, 8, 10, or 16, 20 Hz. The each impulse had the width r_O =10 ms. The centres of the impulses were in points

$$t_{0i} = t_A + i / f_c, \qquad \mathrm{i} = 0,...,k-1,$$

where t_A is the time of switching of the light series, that is the time of the beginning of the first impulse in the sequence.
Thus, the light stimulus can be described as

$$p(t) = \sum_{i=0}^{k-1} \frac{0.5}{r_0\sqrt{\pi}} \exp\left(-\frac{(t-t_{0i})^2}{4r_0^2} \right).$$

The continuous wavelet transform of the light time series $p(t)$ can be calculated in the form:

$$W(f,t_0) = \frac{Df}{\sqrt{s}} \exp\left(-\frac{z^2 + 2(\omega_0 fr_0)^2}{2s} \right) \left[\exp\left(-\frac{i\omega_0 z}{s} \right) - \exp\left(-\frac{i\omega_0^2}{2s} \right) \right],$$

where $s = 1 + 2(fr_0)^2$, $z = f(t - t_0)$ is non-dimensional time measured from time t_O.

5. Estimation of the coefficients of reproduction and holding the rhythm

Let $E_{X1}(\Delta f)$ and $E_{X2}(\Delta f)$ be the global wavelet spectra of the EEG time series in the frequency range Δf over the intervals $[0, t_A]$ and $[t_A, t_B]$, i.e. before and during photostimulation.
The reproduction coefficient of the suggested rhythm can be estimated as the ratio of the maximum of the global spectrum during the light time series to the maximum of the global spectrum before photostimulation:

$$k_R(\Delta f) = \max E_{X2}(\Delta f)/ \max E_{X1}(\Delta f).$$

If the frequency value corresponding to the max $E_{X2}(\Delta f)$ does not coincide with the light time series frequency f_C then there is no reproduction of the rhythm in the range $\Delta f = f_C \pm \Delta$, where Δ=0.5 Hz. The larger $k_R(\Delta f)$ value, the better the reproduction of the suggested rhythm.
Let us $E_X(t)$ and $E_P(t)$ denote the normalized integral distributions of energies of the EEG and light time series in the frequency range $[f_1, f_2]$:

$$E_X(t) = E_X(t)/\max E_X(t) \text{ and } E_P(t) = E_P(t)/\max E_P(t).$$

Examples of the normalized integral distributions $E_X(t)$ and $E_P(t)$ for f_C =4 Hz are given in Fig. 1.

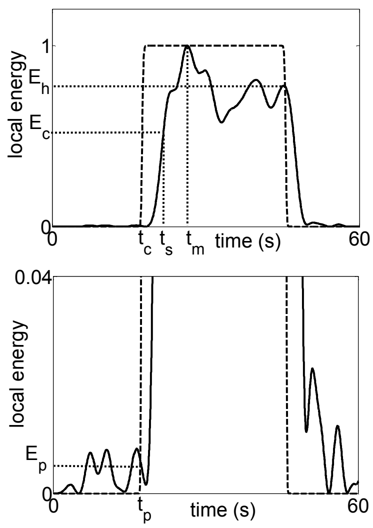

Fig. 1. The normalized energy distributions of the EEG time series (solid line) and the light time series (dashed line). The lower figure is represented in the enhanced scale to see the point (t_P, E_P) of intersection of the integrals $E_X(t)$ and $E_P(t)$.

The integrals $E_X(t)$ and $E_P(t)$ cross each other in two points (t_P, E_P) and (t_h, E_h) after switching on and switching off the light time series.
The value E_h is taken as the coefficient of holding the suggested rhythm:

$$k_H(\Delta f) = E_h(\Delta f).$$

The smaller the value, the more badly the rhythm of photostimulation is kept by the human brain.

6. Estimation of the time of remembering the external rhythm and the delay time of the brain response on the rhythm

If the EEG response on the light time series reaches the maximal value at the moment t_m, then the difference

$$T_R(\Delta f) = t_m(\Delta f) - t_P(\Delta f)f)$$

can characterize the time of remembering the rhythm. The smaller the value, the faster the brain begins to generate the external frequency.
The delay time of the EEG response from the moment of switching on the light time series can be estimated as

$$T_D(\Delta f) = t_S(\Delta f) - t_C(\Delta f),$$

where t_C is the moment when the condition

$$E_C(\Delta f) = 0.5\ (1 - E_P(\Delta f))$$

is satisfied.

7. Results and discussion

Examples of global wavelet spectra of EEG for the healthy subject and patients with changes in the stem-cortical or thalamo-cortical links in two functional states, namely, before and during the light stimulation are given in Fig. 2.
The spectra calculated in the broad frequency range [2, 20] Hz differ by the width as well as by the position and value of maximum.
In the rest state with closed eyes the EEG time series of a healthy person is characterized by narrow frequency interval [8, 16] Hz and the large value of the global energy, maximum of which is equal to $5 * 10^4\ \mu V^2$. The disruptions of neuronal links on the brain-stem level are exhibited in the form of

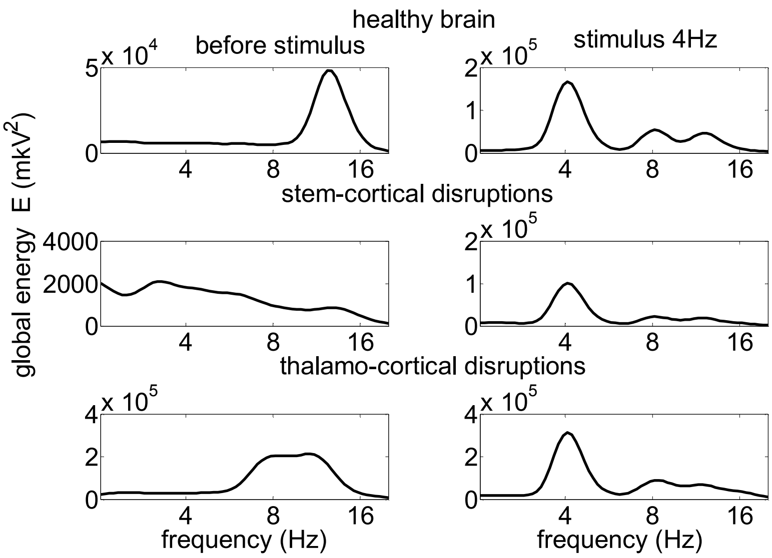

Fig.2. Examples of global wavelet spectra of EEG for the healthy subject and two groups of patients before and during the light time series of f_C =4 Hz.

polymorphous activity of the smaller amplitude and broaden frequency range [0, 12] Hz. The maximal global energy is 10 times less than the value obtained for the healthy person. The thalamo-cortical disruptions are manifested by the extended spectrum in the frequency interval [6, 14] Hz and the significant increase (almost in 10 times) as compared with the maximum of the global spectrum for the healthy brain and in 100 times in comparison with the global energy for the stem-cortical disruptions.

The light stimulus of frequency 4 Hz leads to the emergence of the detectable maximums in all the considered cases. The value of the global energy increases in 4 times for the healthy subject and in 1.5 times for the patient with thalamo-cortical disorders. This value grows in almost 100 times for the patient with stem-cortical defects. The occurrence of the visible maximum of the global energy at the frequency of the external stimulus means the good reproduction of the suggested rhythm.

Reproduction of the external rhythm is observed for all the subjects and the frequencies 4, 6, 8, 10 and 12 Hz and only for the healthy and persons with thalamo-cortical disruptions at 16 and 20 Hz.

The coefficients of reproduction (k_R (Δf)) and holding (k_H (Δf)) the rhythm estimated by the wavelet spectra are given in the Table 1.

The time of remembering the rhythm (T_R (Δf)) and the delay time of the EEG response from the moment of switching on the light time series (T_D (Δf)) are represented also in the Table 1.

f_C =4 Hz				
	k_R	k_H	T_R (s)	T_D (s)
healthy	4.2±0.6	0.52±0.06	11.1±1.2	1.9±0.4
group 1	95±5	0.85±0.07	6.2±0.8	0.9±0.2
group 2	2.1±0.4	0.49±0.05	12.5±1.7	1.5±0.3
f_C =10 Hz				
healthy	6.1±0.7	0.95±0.09	0.9±0.2	0.3±0.11
group 1	2.1±1.3	0.41±0.05	13.2±1.3	2.1±0.5
group 2	5.3±0.6	0.69±0.07	1.5±0.4	0.5±0.1
f_C =16 Hz				
healthy	4.5±0.4	0.81±0.07	5.3±0.4	1.1±0.3
group 1	there is no reproduction of the rhythm			
group 2	3.7±0.3	0.77±0.06	7.1±0.8	2.1±0.5

Table 1. The comparison of the mean values averaged over 10 healthy subjects and 8 persons in each group of patients. The site is Qz. The patients with the thalamo – cortical disruptions are denoted as "group 1" and patients with the stem – cortical defects are depicted as" group 2".

For each frequency of the light time series (f_C) the both coefficients of reproduction and holding the rhythm are largest for the subjects who have the eigen oscillations at this frequency in the rest state.
The time of remembering the rhythm and delay of the EEG response from the moment of switching on the light time series are smallest in the presence of eigen oscillations. These times grow in the non-specific frequency range.
The spectra of the patients of two groups differ by four considered parameters.
The stem – cortical defects are characterized by the absence of the external rhythm reproduction at frequencies larger than 16 Hz and the fast maintenance of the rhythm in the range [2, 6] Hz.
The EEG time series of the patients with the thalamo–cortical disruptions have the large eigen oscillations in the interval [6, 14] Hz and larger values of both coefficients k_R and k_H and smaller times T_R and T_D comparing with the EEG of the first group.

8. Conclusion

The work supports that the human brain is a rather stable dynamic system and rearranges slowly on external rhythm of non-specified frequency range. The parameters found from the wavelet spectra give an opportunity to evaluate quantitatively the brain lability of perception of the light time series.

These parameters can help to estimate the nerve excitability level of a subject for the purpose of the appropriate drug treatment, that is, to exclude the drug administration hyperactivating the nervous system for patients with the enhanced personal excitability in the rest state.

Acknowledgements

The author is thankful to Dr. I. A. Svyatogor for her help with EEG recordings.

References

1. D. Popivanov, et. al. Multifractality of decomposed EEG during imaginary and real visual-motor tracking. *Biological Cybernetics* 94: 149-156 , 2006.
2. M. A. Qianli, et al. A new measure to characterize multifractality of sleep electroencephalogram. *Chinese Science Bulletin* 51: 3059-3064, 2006.
3. A. M. Wink, et al. Monofractal and multifractal dynamics of low frequency endogenous brain oscillations in functional MRI. *Human Brain Mapping* 29: 791-801, 2008.
4. M. Nurujjaman, R. Narayanan and A. N. Sekar Iyengar. Comparative study of nonlinear properties of EEG signals of normal persons and epileptic patients. *Nonlinear Biomedical Physics* 3: 6-11, 2009.
5. G. E. Polychronaki, P.Y. Ktonas, S. Gatzonis, et. al. Comparison of fractal dimension estimation algorithms for epileptic seizure onset detection. *J. Neural Engineering* 7: 60-78, 2010.
6. O. E. Dick, I. A. Svyatogor. Potentialities of the wavelet and multifractal techniques to evaluate changes in the functional state of the human brain. *Neurocomputing* 82: 207-215, 2012.
7. S.V. Bozhokin. Wavelet analysis of dynamics of reproducing and forgetting the rhythms of photostimulation for nonstationary EEG. *J. Technical Physics* 80: 16-24, 2010 (in Russian).
8. O. E. Dick, I. A. Svyatogor. V. A. Ishinova, et al. Fractal characteristics of the functional state of the brain in patients with anxious phobic disorders. *Human physiology* 38: 249 -254, 2012.

Stochastic Properties of Dynamical Systems Arising from (quantum) Spaces and Actions of (quantum) Groups

Nikolaj M. Glazunov

National Aviation University, Kiev
(E-mail: glanm@yahoo.com)

Abstract. We review novel results and investigate actions and transformations of (quantum) groups and semigroups on (quantum) spaces, present dynamical systems and zeta functions arising from these spaces, actions and transformations, discuss their stochastic properties.
Keywords: Dynamical System, Ergodic Transformation, Group Action, Equidistribution, Zeta function, Arithmetic Surface.

1 Introduction

A history of a semigroup and a group action on tori and projective spaces can be found among other in the book by A.G. Postnikov [1], in the paper by I.Ya. Gol'dsheid, G.A. Margulis [2] and in the supplement by B.M. Gurevich, Ya. G. Sinai [3] to the Russian translation of the English edition of the book by P. Billingsley [4].

Here we review novel results and investigate actions and transformations of (quantum) groups and semigroups on (quantum) spaces, present dynamical systems and zeta functions arising from these spaces, actions and transformations, discuss their stochastic properties.

2 Dynamical systems from spaces

It is well known that one-dimensional projective space $\mathbf{P}^1(\mathbf{Q})$ parametrize the set of dynamical systems in such a way that for any rational point $Q \in \mathbf{P}^1(\mathbf{Q}), Q = (\frac{a}{b}, 1), a, b \in \mathbf{Z}, (a, b) = 1$ we naturally assiciate dynamical system $(\mathbf{T}, T_Q)$. Here $\mathbf{T} = \mathbf{R}/\mathbf{Z}, \mathbf{T}^{\mathbf{Z}} = (..., x_{-1}, x_0, x_1, ...), x_i \in \mathbf{T}, X = \{\mathbf{x} = (x_k) : bx_{k+1} = ax_k \text{ for all } k \in \mathbf{Z}\}, T_Q : X \to X$. More generally, for any primitive polynomial $g(x) \in \mathbf{Z}[x]$ of degree $d \geq 1$ it is possible to construct its Frobenius and companion matrices and define a homeomorphism T_F of a compact $d-$dimensional subgroup of $\mathbf{T}^d$. These considerations can be extended to elliptic curves [5] and to abelian varieties. For elliptic curves authors of the paper

Received: 3 April 2013 / Accepted: 16 July 2013
 ISSN 2241-0503

[5] implement these by the following way. Let $q \in \mathbf{Q}_p$ and $\log^+ x$ denotes $\max\{\log x, 0\}$. For a generic element x of $\mathbf{Z}_p$ authors define q-transformation $T_q(x)$ (a p-adic analogue of the β-transformation). Then the topological entropy of the p-adic β-transformation is given by $h(T_q) = \log^+ |q|_p$ ([5], Theorem 4.1). If $|q|_p \geq 1$ then the map T_q is ergodic with respect to Haar measure for $|q|_p > 1$ and is not ergodic for $|q|_p = 1$ ([5], Theorem 4.2). Let $Per_n(T_q)$ denotes the subgroup of $\mathbf{Z}_p$ consisting of elements of period n under T_q. Let U be the set of unit roots of $\mathbf{Q}_p$ and $q \in \mathbf{Q}_p \setminus U$. Then

$$\log |Per_n(T_q)| = n \log^+ |q|_p.$$

([5], Theorem 4.3). The authors use the topological entropy and measure theoretical arguments based on volume growth rate and arithmetic of $\mathbf{Z}_p$.
Let Q be a rational point of an elliptic curve over $\mathbf{Q}$ and let $\hat{h}(Q)$ be the global canonical height on rational points of the elliptic curve. Then with the definitions and assumptions of the paper [5] and $q = a/b = x(Q)$, (i) the entropy of T_Q is given by $h(T_Q) = 2\hat{h}(Q)$, and (ii) the asymptotic growth rate of the periodic points is given by the division polynomial $\nu_n(x)$: $\log |Per_n(T_Q| \sim \log |b^n \nu_n(q)|$ as $n \to \infty$. ([5], Theorem 5.2). In the case authors use also the elliptic analogue of Baker's theorem, which described in paper [6] and in paper [7] .

3 Dynamical systems on probability spaces

Let (X, B, μ, T) be a dynamical system on standard probability space with $T : X \to X$ is measurable, almost surely one to one, preserves μ, for which it is an ergodic transformation. Random dynamical systems relate a partial case of bundle dynamical systems by I. Cornfeld, S. Fomin, and Ya. Sinai [8]. Measurable partition of the space X transforms the initial random dynamical system into a symbolic dynamical system. We will present novel symbolic dynamical systems and their applications.

4 Rigid and weakly mixing ergodic transformations

In papers [9] and [10] authors present resent results on genericity of rigid and multiply recurrent infinite measure preserving and nonsingular transformations and on measurable sensitivity. In the paper [11] authors investigate properties of uniformly rigid transformations and analyze the compatibility of uniform rigidity and measurable weak mixing along with some of their asymptotic convergence properties. All spaces of the paper under review are considered simultaneously as topological spaces and as measure spaces. Presented results concern either the measurable dynamics on the spaces or the interplay between the measurable and topological dynamics. The notion of uniform rigidity was introduced as a topological version of rigidity by S. Glasner and D. Maon [12]. Authors of the paper [11] consider functional analytic properties of uniform rigidity that is similar to the properties of rigidity. Theorem 1 ([11]). Every totally ergodic finite measure-preserving transformation on a Lebesgue space has a representation that is not uniformly rigid, except in the case where the space consists of a single atom.

The proof of the theorem connects with results of authors of the theorem that uniform rigidity and weak mixing are mutually exclusive notions on a Cantor set, and follows from the Jewett-Krieger Theorem by K. Peterson [13].

5 Superrigidity for groups

The concept of superrigidity was introduced by G. D. Mostow [14] and by G. A. Margulis [15] in the context of studying the structure of lattices in rank one and higher rank Lie groups respectively. The notion of property (T) for locally compact groups was defined by D. Kazhdan [16] and the notion of relative property (T) for inclusion of countable groups $\Gamma_0 \subset \Gamma$ was defined by G. Margulis [17]. Now consider the orbit equivalence (OE) superrigidity. One of the first result of this type of superrigidity was obtained by A. Furman [18], who combined the cocycle superrigidity by R. Zimmer [19] with ideas from geometric group theory to show that the actions $SL_n(\mathbf{Z})$ on $\mathbf{T}^n(n \geq 3)$ are OE superrigid. The deformable actions of rigid groups are OE superrigid by S. Popa [20]. The main result of the paper by A. Ioana [21] is the Theorem A on orbit equivalence (OE) superrigidity. As a consequence of Theorem A the author of the paper [21] can constructs uncountable many non-OE profinite actions for the arithmetic groups $SL_n(\mathbf{Z})(n \geq 3)$, as well as for their finite subgroups, and for the groups $SL_m(\mathbf{Z}) \times \mathbf{Z}^m(m \geq 2)$. The author deduces Theorem A as a consequence of the Theorem B on cocycle superrigidity.

Let the action of Γ on X be a free ergodic measure-preserving profinite action (i.e., an inverse limit of actions Γ on X_n with X_n finite) of a countable property (T) group Γ (more generally, of a group Γ which admits an infinite normal subgroup Γ_0 such that the inclusion $\Gamma_0 \subset \Gamma$ has relative property (T) and Γ/Γ_0 is finitely generated) on a standard probability space X. The author prove that if $\omega : \Gamma \times X \to \Lambda$ is a measurable cocycle with values in a countable group Λ, then ω is a cohomologous to a cocycle $\omega^{'}$ which factors through the map $\Gamma \times X \to \Gamma \times X_n$, for some n. As a corollary, he shows that any free ergodic measure-preserving action Λ on Y comes from a (virtual) conjugancy of actions.

6 Equidistribution for orbits of nonabelian semigroups on the torus

Furstenberg [22] and Berent [23] have investigated the action of abelian semigroups on the torus $\mathbf{T}^d$ for $d = 1$ and $d > 1$ respectively. Their results answer problems raising by H. Furstenberg [24]. Authors of the paper [25] extend to the noncommutative case some results of Furstenberg and Berent

7 Zeta functions from spaces and dynamical systems

Recall that Dedekind has defined zeta function for polynomials over prime finite field. The zeta function is trivial and equal to $\frac{1}{1-pz}$. However, combining the zeta function with Chebyshev-Mobius inversion formula we obtain the number of monic irreducible over $\mathbf{F}_p$ polynomials of natural degree m. Riemann and Dedekind zeta functions are first examples of motivic zeta functions. The authors of the paper [26] investigate sufficient conditions for (i) the existence of trace formulae for the Reidemeister number of a group endomorphism; (ii) the rationality of the Reidemeister zeta function and the convergence of the Nielsen zeta function; (iii) the equality of Reidemeister torsion of a group endomorphism to a special value of the Reidemeister zeta. This interesting survey[26] includes recent results on trace formulae, rationality and convergence of zeta functions and relations between special values of zeta functions and some simply homotopy invariants. The general setting of the paper [27] is braided zeta functions in q-deformed geometry. In the framework authors define a zeta function for any rigid object in a ribbon braided category. In the ribbon case they define braided Hilbert series for objects in an Abelian braided category. We will present some other types of zeta-functions.

8 Dynamical Systems from Arithmetic Surfaces

8.1 Sato-Tate case

Let $y^2 = f(x), f(x) = x^3 + cx + d$ be a cubic polynomial in prime finite field $\mathbf{F}_p$. For the number $\#C_p$ of points of the curve $C : y^2 = f(x)$ in $\mathbf{F}_p$ the well known formula

$$\#C_p = \sum_{x=0}^{p-1} \left(1 + \left(\frac{f(x)}{p} \right) \right),$$

take place, where $\left(\frac{f(x_0)}{p}\right)$ is the Legendre symbol with a numerator which is equal to the value of the polynomial $f(x_0)$ in point $x_0 \in \mathbf{F}_p$. It is ease to see that $\#C_p = p - a_p$, where

$$a_p = -\sum_{x=0}^{p-1} \left(\frac{f(x)}{p} \right)$$

If C is the elliptic curve , then the number of points $\#C(\mathbf{F}_p)$ of the projective model of the curve in $\mathbf{F}_p$ is represented by the formula $\#E_p = 1 + p - a_p$, where $a_p = 2\sqrt{p}\cos\varphi_p$, If C is not the elliptic curve, then the value a_p is equal 1, -1 or 0 and ease to compute. In both cases compute: $\varphi_p = \arccos(a_p/2\sqrt{p})$ and reduce it to the interval $[0, \pi]$.

Let E be an elliptic curve over rational numbers $\mathbf{Q}$ which does not admit complex multiplication. Sato and Tate [28] have given computational and theoretical evidences suggesting the distribution of angles φ_p.

Recently L. Clozel, M. Harris, N. Shepherd-Barron, R. Taylor and their colleagues have proved the Sato-Tate conjecture for all elliptic curves E over

Q (and over some its extensions) satisfying the mild condition of having multiplicative reduction at some prime.

Langlands conjectured that some symmetric power $L-$functions extend to an entire function and coincide with certain automorphic $L-$functions.

Theorem (Clozel, Harris, Shepherd-Barron, Taylor). Suppose E is an elliptic curve over Q with non-integral $j-$invariant. Then for all $n > 0, L(s, E, Sym^n)$ extends to a meromorphic function which is holomorphic and non-vanishing for $Re(s) \geq 1 + n/2$.

These conditions suffice to prove the Sato-Tate conjecture.

Theoretical considerations give

Proposition EC. It is possible the arithmetic modeling of the Brownian motion by quantity a_p.

8.2 Kloosterman sums

Let

$$T_p(c,d) = \sum_{x=1}^{p-1} e^{2\pi i(\frac{cx+\frac{d}{x}}{p})}$$

$$1 \leq c, d \leq p-1;\ x, c, d \in \mathbf{F}_p^*$$

be a Kloosterman sum.
By A. Weil estimate

$$T_p(c,d) = 2\sqrt{p}\cos\theta_p(c,d)$$

There are possible two distributions of angles $\theta_p(c,d)$ on semiinterval $[0,\pi)$:

a) *p is fixed and c and d varies over $\mathbf{F}_p^*$; what is the distribution of angles $\theta_p(c,d)$ as $p \to \infty$;*

b) *c and d are fixed and p varies over all primes not dividing c and d.*

For the case *a*) N. Katz [29] and A. Adolphson [30] proved that θ are distributed on $[0,\pi)$ with density $\frac{2}{\pi}\sin^2 t$.
Let

$$cd \not\equiv 0 \bmod p,\ T_p(c,d) = \sum_{x=1}^{p-1} e^{2\pi i(\frac{cx+\frac{d}{x}}{p})}$$

the Kloosterman sum. By A. Weil, $T_p(c,d) = 2\sqrt{p}\cos\theta_p(c,d)$. Compute $T_p, \cos\theta_p, \theta_p$ and reduce θ_p to the interval $[0,\pi]$. Experiments demonstrate random behavior of angles of Kloosterman sums.

Theoretical considerations give

Proposition KS. It is possible the arithmetic modeling of the Brownian motion by Kloosterman sums.

Conclusions

We have presented a review of new results on actions and transformations of (quantum) groups and semigroups on (quantum) spaces, have presented dynamical systems and zeta functions arising from these spaces, actions and transformations, discussed their stochastic properties.

References

1.A.G. Postnikov, Selected papers (In Russian), Fizmatlit, Moscow, 2005.
2.I.Ya. Gol'dsheid, G.A. Margulis, Uspekhi Mat. Nauk 44, no. 5, 13-60, 1989.
3.B.M. Gurevich, Ya. G. Sinai, Algebraic automorphisms of the torus and Markov chains.
4.P. Billingsley, Ergodicheskaya teoriya i informatsiya (Ergodic Theory and Information), Mir, Moscow, 1969.
5.D'Ambros, P.; Everest, G.; Miles, R.; Ward, T. Dynamical systems arising from elliptic curves. Colloquium Math., vol. 84/85 (2000) 95 - 107.
6.S. David. Mem. Soc. Math. France 62 (1995).
7.G. Everest and T. Ward. Experiment. Math. 7 (1998), 305-316.
8.I. Cornfeld, S. Fomin, and Ya. Sinai, Ergodic Theory, Grundlehren der Mathematischen Wissenschaften (Fundamental Principles of Mathematical Sciences), vol. 245 (1982), Springer-Verlag, New York.
9.O. Ageev and C. Silva. Proceedings of the 16ty Summer Conference on General Topology and its applications (New York), Topology Proc. 26, No. 2, 357-365 (2002).
10.J. James, T. Koberda, K. Lendsey, C. Silva. Proc. Amer. Math. Soc., 136, 3549-3559 (2008).
11.James, Jennifer; Koberda, Thomas; Lindsey, Kathryn; Silva, Cesar E.; Speh, Peter. On ergodic transformations that are both weakly mixing and uniformly rigid. New York J. Math. 15, 393-403 (2009).
12.S. Glasner and D. Maon. Ergodic Theory Dynam. Systems 9, 309-320 (1989).
13.K. Peterson. Ergodic Theory. Cambridge Studies in Advanced Mathematics, 2. Cambridge University Press, Cambridge (1983).
14.G. D. Mostow. Strong rigidity of locally symmetric spaces, Princeton University Press, Princeton, N.J., Annals of Mathematics Studies, No. 78. (1973).
15.G. A. Margulis Discrete subgroups of semisimple Lie groups. Ergeb. Math. Grenzgeb. 17, Springer-Verlag, Berlin (1991; Zbl)]
16.D. Kazhdan. Funct. Anal. and its Appl. 1, 63-65 (1967).
17.G. Margulis. Ergodic Theory Dynam. Systems 2, 383-396 (1982).
18.A. Furman. Ann. of Math., vol. 150, 2, 1059-1081, 1083-1108 (1999).
19.R. Zimmer. Ergodic theory and semisimple groups, Monographs in Mathematics, 81, Birkhuser Verlag, Basel, x+209 pp. (1984).
20.S. Popa. International Congress of Mathematicians. Vol. I, Eur. Math. Soc., Zurich, pp. 445-477 (2007).
21.Ioana, Adrian. Cocycle superrigidity for profinite actions of property (T) groups, Duke Math. J. 157, No. 2, 337-367 (2011).
22.H. Furstenberg. Math. System Theory 1 (1967), 1-40.
23.D. Berent. Trans. Amer. Math. Soc. 286 (1984), no. 2, 505-535.
24.H. Furstenberg. Tata Ins. Fund. Res. Stud. Math., vol. 14, Tata Ins. Fund. Res., Bombay, 105-117 (1998).

25.Bourgain, Jean; Furman, Alex; Lindenstrauss, Elon; Mozes, Shahar. Stationary measures and equidistribution for orbits of nonabelian semigroups on the torus. J. Am. Math. Soc. 24, No. 1, 231-280 (2011).
26.Fel'shtyn, Alexander; Hill, Richard. Trace formulae, zeta functions, congruences and Reidemeister torsion in Nielsen theory. Forum. Math. 10, no. 6, 641-663 (1998).
27.Shahn, Majid; Ivan, Tomasic. On braided zeta functions. Bull. Math. Sci. 1, 379-396 (2011).
28.B.J. Birch, J. London Math. Soc., 43, 57-60 (1968).
29.Katz N. Gauss sums, Kloosterman sums, and monodromy groups. Princeton university press, (1988), 246p.
30.Adolphson A. Journ. rein. angew. Math., 395, (1989), pp.214-220.
31.N.M. Glazunov. Arithmetic maps and their modeling (In Russian), *International Conference Avia-2011*, Kiev, NAU, Vol.1. P.6.1-6.3, 2011.
32.N.M. Glazunov. Dynamics, Coding And Entropies, *Fourth World Congress, AVIATION IN THE XXI-st CENTURY*, NAU, Kiev, P.18.39-18.42, 2010.
33.N.M. Glazunov. Methods to Justifying of Arithmetic Hypotheses and Computer Algebra, *Programmirovanie*, N 3, P.2-8, 2006.
34.N.M. Glazunov. On moduli spaces, equidistribution, bounds and rational points of algebraic curves, *Ukrainian Math. Journal*, 9: 1174-1183, 2001.

Chaotic Modeling and Simulation (CMSIM) 3: 403–411, 2013

Mixing and Coherent Structures in Two and Three Dimensional Containers

Tatyana S. Krasnopolskaya[1], Volodymyr S. Malyuga[1] and Oleksandr L. Golichenko[2]

[1] Institute of Hydromechanics NASU, 03680 Kiev, Ukraine
(E-mail: `t.krasnopolskaya@tue.nl; v_s_malyuga@ukr.net`)
[2] Kiev National Taras Shevchenko University, Kiev, Ukraine
(E-mail: `Golichenko_O_L@mail.ru`)

Abstract. This study addresses problems: what determines coherent structures in mixing patterns and what are main elements of the coherent structures. We restrict our consideration to finite times and are mainly interested in how to organize steady or periodic flow and where to put the blob (or blobs) in order to achieve the best result in that finite time. Knowing types and positions of periodic points coherent structures in distributive mixing patterns could be classified. These structures are connected with hyperbolic and elliptic periodic points and lines for three-dimensional mixing flows.
Keywords: Distributive mixing, Periodic points and lines, Coherent structures.

1 Introduction

We consider the laminar mixing process in a two-dimensional annular wedge-shaped cavity and in a three-dimensional creeping flow of a viscous incompressible fluid contained in a finite circular cylinder, induced by a prescribed periodic motion of the end walls. Here we apply a method to locate periodic structures and manifolds. In contrast to two-dimensional flow of an incompressible fluid, for which the equations of motion of an individual passive particle can always be written in Hamiltonian form and for which well-developed methods of Hamiltonian mechanics can be applied, the study of three-dimensional mixing flows encounters considerable difficulties. An important characteristic of both two-dimensional and three-dimensional flows, that is closely related to the problem of determination of the regions of regular behaviour being barriers for the mixing process (Aref[1]), is the location of periodic points (or fixed points in the hyperplane of the Poincaré map). The determination and classification of periodic points in three-dimensional flows is a complicated problem. Furthermore, in three-dimensional flows these points can form one-dimensional periodic lines. A complete classification of the periodic points can be performed in accordance

Received: 30 March 2013 / Accepted: 12 July 2013

ISSN 2241-0503

with three eigenvalues of the linearized matrix of the Poincaré map, and specific behaviour of the map near such a point can be associated with its type [4]. Generally, the periodic points of three-dimensional flows could be characterized by a much richer variety, compared to the points of two-dimensional flows, in which only three possible types exist. However, if in a three-dimensional flow the point lies on a periodic line it is not significantly different from periodic points in two-dimensional flows. In the three-dimensional case, the flow near a periodic line is topologically similar to the flow near a periodic point in two-dimensional case.

2 Stirring of a viscous incompressible fluid

2.1 Mixing in a two-dimensional annular wedge-shaped cavity

As a first example of mixing, we consider a two-dimensional creeping flow of an incompressible viscous fluid in an annular wedge cavity, $a \leq r \leq b$, $|\theta| \leq \theta_0$, driven by periodically time-dependent tangential velocities $V_{bot}(t)$ and $V_{top}(t)$ at the curved bottom and top boundaries, when a radius r is $r = a$ and $r = b$, respectively. The side walls, $a \leq r \leq b$, $|\theta| = \theta_0$ are fixed. We consider a discontinuous mixing protocol with the bottom and top walls alternatingly rotating over an angle Θ in clockwise and counterclockwise directions, respectively. More specifically, we consider the case

$$V_{bot}(t) = \frac{2a\Theta}{T}, V_{top}(t) = 0, \quad \text{for} \quad kT < t \leq \left(k + \frac{1}{2}\right) T,$$

$$V_{bot}(t) = 0, \quad V_{top}(t) = -\frac{2b\Theta}{T},$$

$$\text{for} \quad \left(k + \frac{1}{2}\right) T < t \leq (k+1)T, \tag{1}$$

where $k = 0, 1, 2, \ldots.$ Θ is the angle of wall rotation and T is the period of the walls motion. The radial and azimuthal velocity components u_r and u_θ can be expressed by means of the stream function $\Psi(r, \theta, t)$ as

$$u_r = \frac{1}{r}\frac{\partial \Psi}{\partial \theta}, \qquad u_\theta = -\frac{\partial \Psi}{\partial r}. \tag{2}$$

For a quasi-stationary creeping flow in the Stokes approximation the stream function Ψ satisfies the biharmonic equation

$$\nabla^2 \nabla^2 \Psi = 0, \tag{3}$$

with the Laplace operator ∇^2 and the boundary conditions

$$\Psi = 0, \ \frac{\partial \Psi}{\partial r} = -V_{bot}, \ \text{at} \ r = a, \ |\theta| \leq \theta_0, \tag{4}$$

$$\Psi = 0, \ \frac{\partial \Psi}{\partial r} = -V_{top}, \ \text{at} \ r = b, \ |\theta| \leq \theta_0, \tag{5}$$

$$\Psi = 0, \ \ \frac{\partial \Psi}{\partial \theta} = 0, \ \ \text{at} \ \ a \leq r \leq b, \ \ |\theta| = \theta_0. \tag{6}$$

Therefore, we have the classical biharmonic problem for the stream function Ψ with prescribed values of this function and its outward normal derivative at the boundary.

The system of ordinary differential equations

$$\frac{dr}{dt} = \frac{1}{r}\frac{\partial \Psi}{\partial \theta}, \qquad r\frac{d\theta}{dt} = -\frac{\partial \Psi}{\partial r} \tag{7}$$

with the initial conditions $r = r_{in}, \ \theta = \theta_{in}$ at $t = 0$ describes the motion of an individual (Lagrangian) particle occupying the position (r, θ) at time t. In fact, we have steady motion of the particle within time intervals $(kT, kT + T/2)$, $(kT + T/2, kT + T)$, with velocities that instantaneously change at $t_k = kT/2, \ (k = 0, 1, 2, ...)$.

It is easy to check that, within these intervals, when the stream function does not explicitly depend on time, system (11) has the first integral $\Psi(r, \theta) = const$. Therefore, this system is integrable and a particle initially at (r_{in}, θ_{in}) moves along a steady streamline during the first half period $(0, T/2)$. At the instant $t = T/2$ when the forcing is switched, the topology of streamlines is changed, and the particle instantaneously moves along a new streamline during the second half of period $(T/2, T)$, and so on. The spatial position of the particle is continuous, but its velocity experiences a discontinuity at each half period.

It is because of these abrupt periodical changes in the velocity field that the question of stability and instability of the solution of system (11) and possibility of chaotic advection (Aref[1]) naturally arises.

The problem of mixing of a certain amount of dyed passive material (the blob), as considered here, consists of tracking in time the positions of particles initially occupying the contour of the blob, say, the circle of radius R with the center at (r_c, θ_c). We assume that the flow provides only a continuous transformation of the initially simply connected blob. Therefore, the deformed contour of the blob gives the whole picture of the mixing.

This wedge-cavity flow problem has been solved analytically by Krasnopolskaya *et al.*[2]. Their analytical solution was used for the numerical evolution of the interface line between the marker fluid and the ambient fluid, which was carried out by the dynamical contour tracking algorithm.

2.2 Statement of mixing problem in a cylinder

Consider the three-dimensional Stokes flow in a finite cylinder that occupies the domain $0 \leq r \leq a, \ 0 \leq \theta \leq 2\pi, \ 0 \leq z \leq H$ in the cylindrical coordinates (r, θ, z). In terms of the velocity vector $\mathbf{u}$ and the pressure p, the Stokes flow of an incompressible viscous fluid (inertia terms being negligible) is governed by

$$\mu \nabla^2 \mathbf{u} = \nabla p, \qquad \nabla \cdot \mathbf{u} = 0, \tag{8}$$

where ∇, $\nabla \cdot$, and ∇^2 stand for standard differential operations of gradient, divergence, and the Laplacian operator, respectively, and μ is the coefficient of shear viscosity of the fluid. The flow is generated by periodic motion of the cylinder end wall at $z = H$, while the cylinder wall $r = a$ remains fixed. In terms of Cartesian components, with the positive x-axis coinciding with the direction $\theta = 0$, the velocity vector $\mathbf{u} = u\,\mathbf{e}_x + v\,\mathbf{e}_y + w\,\mathbf{e}_z$ takes the following form at the domain boundaries:

$$\mathbf{u} = u_{top}(t)\,\mathbf{e}_x + v_{top}(t)\,\mathbf{e}_y, \quad z = H, \quad 0 \le r \le a, \quad 0 \le \theta \le 2\pi\,, \tag{9}$$

In what follows we consider one typical protocol of the wall motions with a constant velocity V and with period T (only the non-zero velocities are presented below). Protocol consists of two 'zigzag' steps of the top wall only:

$$u_{top} = V, \quad 0 \le t \le \frac{1}{2}T, \qquad\qquad v_{top} = V, \quad \frac{1}{2}T \le t \le T. \tag{10}$$

Note that the protocol is discontinuous, although the motion of the fluid inside the cylinder is steady at any time within the whole period. Since the inertia forces are neglected in the governing equations (8), these steady motions are established instantaneously. Because of the linearity of system (8) and the absence of time dependent terms, the velocity field in the cylinder is periodic with period T.

Important for further analysis is the dimensionless kinematic parameter $D = VT/a$, which represents the ratio of two typical time scales of any given protocol: the forcing period T and the advection time a/V (for a wall travelling over a typical distance a with a velocity V).

The mixing process taking place is due to advection of passive material tracers by the velocity field $\mathbf{u}$ and is hence governed by the three-dimensional system of ordinary differential equations

$$\frac{dx}{dt} = u\,(x, y, z, t), \quad \frac{dy}{dt} = v\,(x, y, z, t), \quad \frac{dz}{dt} = w\,(x, y, z, t), \tag{11}$$

with initial conditions $x = x_0$, $y = y_0$, $z = z_0$ at $t = 0$.

A full analytical solution for the linear vector boundary problem for the velocity field has been constructed by Meleshko *et al.*[5]. by the method of superposition. The principal idea of the method consists in representing the velocity field in the finite cylinder as the sum of two velocity fields: one for an infinite layer with thickness equal to the finite cylinder height, and another for an infinite cylinder with a radius equal to that of the original cylinder. Velocities in these simple domains are represented in the form of ordinary Fourier series with sets of arbitrary coefficients on the complete systems of Bessel and trigonometric functions, respectively. These series both identically satisfy the governing equation inside the domain and have sufficient functional arbitrariness for fulfilling any boundary conditions on the top and bottom walls and on the lateral surface of the cylinder, respectively. Because of the interdependency, the expression for a coefficient of a term in one series will depend on all the coefficients of the other series and vice versa. The final solution involves solving an infinite system of linear algebraic equations, providing the relations between applied velocities and the coefficients in two ordinary Fourier series on the complete systems of Bessel and trigonometric functions in radial and axial directions, respectively. The general theory of such infinite systems provides leading terms in the asymptotic behaviour of coefficients. An established technique was used to considerably improve the convergence of the series on the whole boundary, including the rims. The numerical results presented in Meleshko *et al.*[5] reveal that the boundary conditions for the case of a lid-driven cavity are satisfied within the accuracy $\mathcal{O}(10^{-3})$ in comparison with the prescribed velocity, even at the corner point.

The problem of accurate determination of the interface is obviously very complicated, as it moves and deforms with the flow. There exist many techniques to deal with flows containing sharp fronts, which can be divided into two basic strategies – front-capturing and front-tracking. Detailed reviews of the front-tracking methods are provided by Krasnopolskaya *et al.*[3] and Malyuga *et al.*[4].

2.3 Periodic points and lines

A periodic point $\mathbf{P}$ of period n can be classified as an elliptic, hyperbolic, or parabolic point depending upon the structure of the surrounding flow field. This classification is based on the behaviour (in the course of time) of an infinitesimally close neighbouring point $\mathbf{P} + d\mathbf{x}_0$. After n periods, the latter arrives at $\mathbf{P} + d\mathbf{x}_n = \mathbf{\Phi}_T^n(\mathbf{P} + d\mathbf{x}_0)$, upon linearization about the periodic point $\mathbf{P} = \mathbf{\Phi}_T^n(\mathbf{P})$, adding up to

$$d\mathbf{x}_n = F \cdot d\mathbf{x}_0 \tag{12}$$

with $F = \partial\mathbf{\Phi}_T^n/\partial\mathbf{x}|_{\mathbf{P}}$ the real Jacobian matrix. According to (12), stable and unstable structures may emerge, depending on the properties of the matrix F. In order to analyse the nature of the map near $\mathbf{P}$, the relation (12) is rewritten in the canonical (or Jordan) form

$$\boldsymbol{\eta}_n = S \cdot \boldsymbol{\eta}_0 \qquad S = R^{-1} \cdot F \cdot R \qquad \boldsymbol{\eta} = R^{-1} \cdot d\mathbf{x} \tag{13}$$

with R the transformation matrix relating the local Cartesian (dx, dy, dz) to the canonical ($\eta^{(1)}$, $\eta^{(2)}$, $\eta^{(3)}$) frame of reference.

In two-dimensional systems, elliptic points are surrounded by islands, sealing off the elliptic region from the remainder of the flow domain and in consequence acting as transport barriers. The hyperbolic points $\mathbf{x}_h$ are accompanied by stable manifolds $W^s(\mathbf{x}_h)$ and unstable manifolds $W^u(\mathbf{x}_h)$ that merge either into closed orbits or display transversal intersection. The former phenomenon is reminiscent of the aforementioned elliptic islands by obstructing communication between flow regions, whereas the latter brings about excessive stretching and folding of material elements, indicative of chaotic advection [1]. In the three-dimensional domain of interest the islands and manifolds, associated with periodic points on the elliptic and hyperbolic segments of the periodic line, readily merge into tubular objects and intricate surfaces, although possessing essentially two-dimensional characteristics.

The periodic lines of period-2 of the flow generated in a cylinder are shown in figure 1

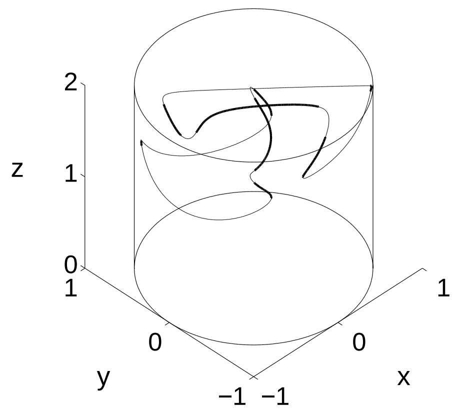

Fig. 1. The periodic lines of period-2 in the flow in the cylinder for $D = 5$. Thick and thin lines represent the elliptic and hyperbolic segments, respectively [4].

Such lines were found to exist only for $D > 2$. It is worth noting that each of the two lines returns into itself after two periods. Although any periodic point of second order exists always in combination with another one, they can belong to the same periodic line of the second order.

3 Coherent structures

The results presented correspond to one typical wedge cavity with $\theta_0 = \pi/4$ and $b/a = 2$. Using the dimensionless parameter $H = \Theta/\theta_0$ and a fixed value for the period T, the discontinuous mixing protocol (1) is completely defined. We restrict our consideration to the case $H = 4$. The accurate Lagrangian description of the contour line provides the possibility to construct an Eulerian representation of the mixture. Figure 2(a) shows the mixed state with the positions of the initially circular blob (green area) after six periods (red) and after twelve periods (blue). There are two main components of the coherent structure in the mixed state: one component formed by the thin filaments with their striation decreasing in time and the other one by the small 'rubbery' region, representing the unmixed part of the blob. What creates this structure? First of all, the invariant unstable manifold corresponding to the hyperbolic point of period-1 which is located in the centre of the original green blob (indicated by a black square in the middle in figure 2b). This manifold, presented in the figure 3(a), serves as a skeleton which forms the first main coherent structures of the deforming blob. The origin of the 'rubbery' coherent structure can be explained in terms of the existence of elliptic periodic points of period-6, period-2 and period-6, respectively, which are shown as white boxes in figure 2(b). In the upper part of the green circular blob (figure 2b), a small black box indicates the position of the hyperbolic fixed point of period-6 and therefore, the 'rubbery' region nearby this point will be destroyed completely in course of time.

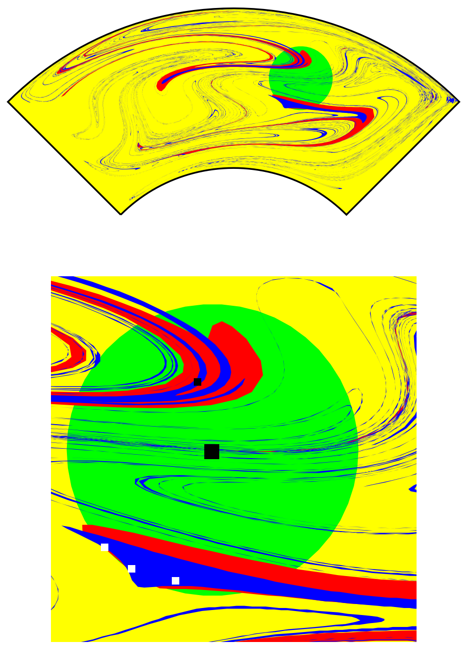

Fig. 2. Mixing patterns: (a) in the whole cavity; (b) in the region of the initial blob position.

The resulting deformation after twelve periods of small circular domains surrounding these higher order periodic points are shown in figure 3(b). The small circular blob surrounding the hyperbolic point transforms after twelve periods into a thin red line, while the three circular bolbs surrounding the elliptic points only slightly deform (the so-called 'rubbery' regions).

4 Conclusions

Coherent structures in distributive mixing patterns are classified. These structures are connected with hyperbolic and elliptic periodic points (and lines) of order-1 or higher.

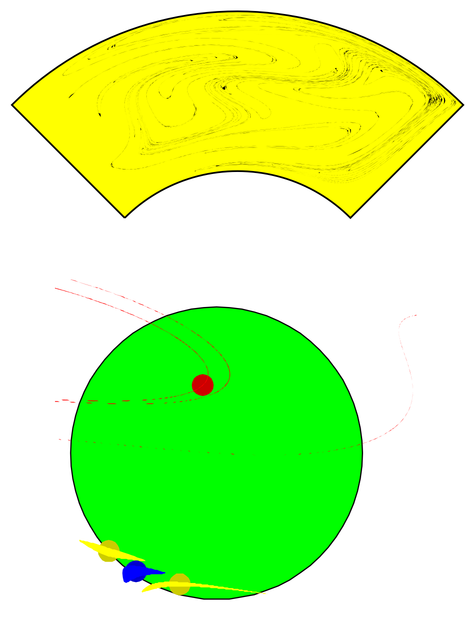

Fig. 3. The elements of coherent structures: (a) part of unstable manifold of the hyperbolic point of period-1 in the centre of the initial blob; (b) deformation patterns of small circular blobs surrounding periodic points of higher order.

References

1.H. Aref. Stirring by chaotic advection. *J. Fluid Mech.* 143: 1–24, 1984.
2.T. S. Krasnopolskaya, V. V. Meleshko, G. W. M. Peters and H. E. H. Meijer. Steady Stokes flow in an annular cavity. *Q. J. Mech. Appl. Math.*, 49: 593–619, 1996.
3.T. S. Krasnopolskaya, V. V. Meleshko, G. W. M. Peters and H. E. H. Meijer. Mixing in Stokes flow in an annular wedge cavity. *Eur.J. Mech.B/Fluids*, 18:793–822, 1999.
4.V. S. Malyuga, V. V. Meleshko, M. F. M. Speetjens, H. J. H. Clercx and G. J. F. van Heijst. Mixing in the Stokes flow in a cylindrical container. *Proc. R. Soc. London*, A 458: 1867-1885, 2002.

5.V. V. Meleshko, V. S. Malyuga and A. M. Gomilko. Steady Stokes flow in a finite cylinder. *Proc. R. Soc. London*, A 456: 1741–1758, 2000.

Chaotic Modeling and Simulation (CMSIM) 3: 413-422, 2013

Chaos in Parametrically Excited Continuous Systems

Tatyana S. Krasnopolskaya[1]
Alexandre A. Gourjii[2]
Viacheslav M. Spektor[1]
Dmytro F. Prykhodko[3]

[1] Institute of Hydromechanics NAS of Ukraine, Kyiv, Ukraine
(E-mail: t.krasnopolskaya@tue.nl; v.m.spektor@gmail.com)
[2] National Technical university of Ukraine "KPI", Kyiv, Ukraine
(E-mail: a.gourjii@gmail.com)
[3] Taras Shevchenko National University of Kyiv, Kyiv, Ukraine
(E-mail: dmitry.prykhodko@gmail.com)

Abstract: Two new mathematical models of cross-waves generation in fluid free surface between two cylindrical shells when the inner wall vibrates radially and parametric oscillations of a cantilever bar with low bending rigidity are worked out. In the cases of internal resonances parametric oscillations of continuous systems are approximated by two eigenmodes with different eigen frequencies. Those two eigen modes are dominant and they are resonant. On the basis of analysis of the largest Lyapunov exponents for a complex system three types of steady-state regimes are found: periodic, quasi-periodic and chaotic regimes. Phase portraits and power spectra are constructed and studied. Attention is concentrated mainly on the properties of chaotic attractors.
Keywords: Waves in fluid free surface, Cross-waves, Cantilever bar, Bending rigidity, Eigenmodes.

1 Introduction

The phenomenon of deterioration of fluid free-surface waves between two cylindrical shells when the inner wall vibrates radially, is rather known, Faraday, 1831, [3]. The waves may be excited by harmonic axisymmetric deformations of the inner shell and depending on the vibration frequency both axisymmetric and non-symmetric wave patterns may arise. Experimental observations have revealed that waves are excited in two different resonance regimes. The first type of waves corresponds to forced resonance, in which axisymmetric patterns are realized with eigenfrequencies equal to the frequency of excitation. The second kind of waves is parametric resonance waves and in this case the waves are "transverse", with their crests and troughs aligned perpendicular to the vibrating wall. These so-called cross-waves have frequencies equal to half of that of the wavemaker, Krasnopolskaya, 1996, [4]. To obtain a lucid picture of energy transmission from the wavemaker motion (inner shell vibrations) to the fluid free-surface motion the method of superposition has been used.

Received: 2 April 2013 / Accepted: 17 July 2013

ISSN 2241-0503

As the second task oscillation regimes of a cantilever bar with low bending rigidity are studied in the present paper. In the case of internal resonance parametric oscillations of cantilever bar with low bending rigidity are approximated by two eigenmodes with different eigen frequencies, Krasnopolskaya, 2012, [5].

2 Two Mode Model of Cross-waves

Let us theoretically consider the nonlinear problems of fluid free-surface waves which are excited by inner shell vibrations in a volume between two cylinders of finite length. It is useful to relate the fluid motion to the cylindrical coordinate system (r,θ,x). The fluid has an average depth d ; the average position of the free surface is taken as $x=0$, so that the solid tank bottom is at $x=-d$. The fluid is confined between a solid outer cylinder at $r=R_2$ and a deformable inner cylinder (which acts as the wavemaker) at average radius $R_1 = r_1 + a_0(d)^{-1}\int_{-d}^{0}\cos(\eta x)dx = r_1 + 2a_0/\pi$. This inner cylinder vibrates harmonically in such a way that the position of the wall of the inner cylinder is $r = R_1 + \chi_1(x,t) = R_1 - (a_0 + a_1\cos\omega t)\cos\eta x - 2a_0/\pi$,where $\eta = \pi/(2d)$. Assuming that the fluid is inviscid and incompressible, and that the induced motion is irrotational, the velocity field can be written as $\mathbf{v}=\nabla\phi$, with $\phi(r,\theta,x,t)$ the velocity potential. The governing equation is

$$\nabla^2\phi = 0 \qquad \text{on} \qquad (R_1+\chi_1 \le r \le R_2, 0\le\theta\le 2\pi, -d\le x\le\zeta) \tag{1}$$

where $\zeta(r,\theta,t)$ is free surface displacement.

The dynamic and kinematic free-surface boundary conditions are:

$$\phi_t + 1/2(\nabla\phi)^2 + g\zeta = F(t)$$

$$\phi_x = \nabla\phi\cdot\nabla\zeta + \zeta_t \qquad \text{at} \qquad x=\zeta(r,\theta,t) \tag{2}$$

with g the gravitational acceleration, ρ the fluid density, $F(t)$ is an arbitrary function of time. Here and later the subscripts x,r,θ,t signify partial differentiation.

The kinematic condition at the vibrating inner cylinder is:

$$\phi_r = \chi_t + \nabla\phi\cdot\nabla\chi_1 \qquad \text{at} \qquad r = R_1+\chi_1(x,t). \tag{3}$$

From the experimental observations we may conclude that the pattern formation has a resonance character, every pattern having its "own" frequency. Assuming that patterns can be described in terms of normal modes with characteristic eigenfrequencies, we expand the potential ϕ and the free-surface displacement ζ in a complete set of eigenfunctions, which are determined by linear theory. The amplitudes of these eigenfunctions are governed by the nonlinear problem (2) - (3). The potential ϕ can be written as the sum of three harmonic functions $\phi = \phi_0 + \phi_1 + \phi_2$, Lamé, 1852, [7]. The solution of the linear problem for ϕ_1 can be written in the form

$$\phi_1 = \sum_{i=0}^{\infty}\sum_{j=1}^{\infty} \phi_{ij}^{c,s}(t) \frac{\cosh k_{ij}(x+d)}{N_{ij}\cosh k_{ij}d} \psi_{ij}^{c,s}(r,\theta), \tag{4}$$

on the complete systems of azimuthal ($\cos i\theta$, $\sin i\theta$), and radial eigenfunctions $\chi_{ij}(k_{ij}r) = J_i(k_{ij}r) - \frac{J_{i'}(k_{ij}R_1)}{Y_{i'}(k_{ij}R_1)} Y_i(k_{ij}r)$, with some arbitrary amplitudes $\phi_{ij}^{c,s}(t)$. In the solution (4) the notations $\psi_{ij}^{c,s}(r,\theta) = \chi_{ij}(k_{ij}r)(\cos i\theta, \sin i\theta)$ are used, where J_i and Y_i are the i-th order Bessel functions of the first and the second kind, respectively, and N_{ij} is a normalization constant, where the index c (or s) indicates that the eigenfunction $\cos i\theta$ (or $\sin i\theta$) is chosen as the circumferential component; k_{ij} represents eigen wave numbers. The system of functions $\psi_{ij}(r,\theta)$, with $i = 0,1,2,...$ and $j = 1,2,3,...$, is a complete orthogonal system, so any function of the variables r and θ can be represented using the usual procedure of Fourier series expansion. Thus, the free surface displacement $\zeta(r,\theta,t) - \zeta_0(t)$ can be written as ($\zeta_0(t)$ is the mean level of fluid free surface oscillations)

$$\zeta(r,\theta,t) - \zeta_0(t) = \sum_{i=0}^{\infty}\sum_{j=1}^{\infty} \zeta_{ij}^{c,s}(t) \frac{\psi_{ij}^{c,s}(r,\theta)}{N_{ij}}. \tag{5}$$

The velocity potential $\phi_2(r,\theta,x,t)$ can be formulated in terms of an ordinary Fourier series in $\cos\alpha_l x$ with $\alpha_l = l\pi/d$ and in ($\cos i\theta$, $\sin i\theta$), so that the general solution reads, Krasnopolskaya, 1996, [4]

$$\phi_2 = \sum_{i=0}^{\infty}\sum_{l=1}^{\infty} \Phi_{il}^{c,s}(t)\cos\alpha_l x \hat{\chi}_{il}(\alpha_l r)(\cos i\theta, \sin i\theta) \tag{6}$$

with $\hat{\chi}_{il}(\alpha_l r) = I_i(\alpha_l r) - \dfrac{I'_i(\alpha_j R_2)}{K'_i(\alpha_j R_2)} K_i(\alpha_l r)$, where I_i and K_i the i-th order modified Bessel functions of the first and second kind, respectively.

Under a parametric resonance, when the excitation frequency is twice as large as one of the eigenfrequencies, i.e. $\omega \approx 2\omega_{nm}$, and according the experimental observations we may assume that the free-surface displacement can be approximated by two resonant modes. So that we may write

$$\zeta \approx \frac{1}{N_{nm}} \zeta_{nm} \psi^c_{nm}(r,\theta) + \frac{1}{N_{0l}} \zeta_{0l} \psi_{0l}(r) + \zeta_0 \tag{7}$$

where ψ_{0l} is the axisymmetric mode which has the eigenfrequency by a value very close to ω, i.e. $\omega_{0l} \approx \omega$. From the experimental observations follows that cross-waves has ampliteds much bigger than the amplitudes of the forced waves with the frequency ω of the wavemaker vibrations. So that we can seek the unknown functions in the form

$$\zeta_{nm}(t) = \varepsilon_1^{1/2}\, \lambda_1 \left[p_1(\tau_1) \cos\frac{\omega t}{2} + q_1(\tau_1) \sin\frac{\omega t}{2} \right];$$

$$\zeta_{0l}(t) = \varepsilon_1 \lambda_0 \left[p_2(\tau_1) \cos \omega t + q_2(\tau_1) \sin \omega t \right], \tag{8}$$

where $\lambda_1 = k_{nm}^{-1}\, \mathrm{th}(k_{nm} h)$, $\varepsilon_1 = \dfrac{a\omega_{nm}^2}{\mathrm{g}}$ is a small parameter, $\tau_1 = \dfrac{1}{4} \varepsilon_1\, \omega t$ is a dimensionless slow time, $\lambda_0 = k_{0l}^{-1}\, \mathrm{th}(k_{0l} h)$. By substitution of the expressions (8) into boundary conditions (2)-(3), using (4)-(7) and averaging over the fast time ωt, Krasnopolskaya, 1996, [4], we finally obtain

$$\begin{aligned}
\frac{dp_1}{d\tau_1} &= -\alpha p_1 - \vartheta q_1 + \beta_3 q_1 + \beta(q_1 p_2 - p_1 q_2); \\
\frac{dq_1}{d\tau_1} &= -\alpha q_1 + \vartheta p_1 + \beta_3 p_1 + \beta(p_1 p_2 + q_1 q_2); \\
\frac{dp_2}{d\tau_1} &= -\alpha p_2 - \beta_2 q_2 - 2\beta_4 p_1 q_1; \\
\frac{dq_2}{d\tau_1} &= -\alpha q_2 + \beta_2 p_2 + \beta_4 (p_1^2 - q_1^2) + \beta_5,
\end{aligned} \tag{9}$$

where $\vartheta = \left[\beta_1 + \frac{\beta_6}{2}(p_1^2 + q_1^2) \right]$, $\alpha = \frac{\delta}{\omega_{nm}}$, δ is the ratio of actual to critical damping of the mode, β_i (*i=1,2,…6*) are constant coefficients. The dynamical system (9) is nonlinear, so numerical solutions were obtained. We used the following coefficients (Krasnopolskaya, 1996, [4] – Becker, 1991, [1]) and data:

$\alpha = 0.01$; β_1=0.1; β_2=0.1; β_3=1.3*k*; β_4=-1.2; β_5=0.235*k*;

β_6=1.12; β =-1.531; $p_1(0) = q_1(0) = p_2(0) = q_2(0) = 0.5$.

For these parameters and for different values of *k* (which is dimensionless amplitude of the wavemaker vibrations) extensive numerical calculations were carried out in order to find all steady state regimes. In Figure 1 dependence of the maximum Lyapunov exponent on value *k* is shown.

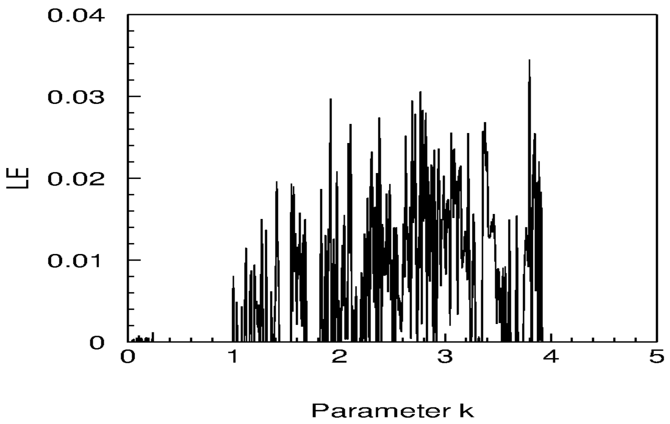

Fig. 1. The dependence of the maximum Lyapunov exponent on value *k*.

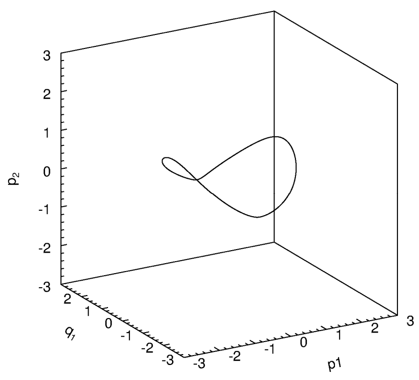

a) $k = 0.5$

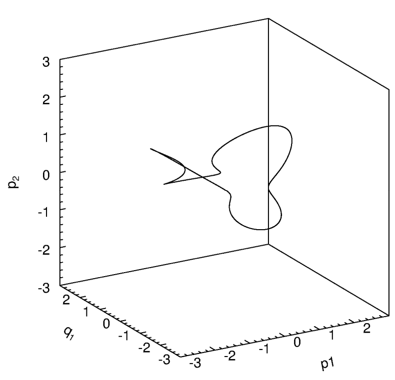

b) $k = 0.8$

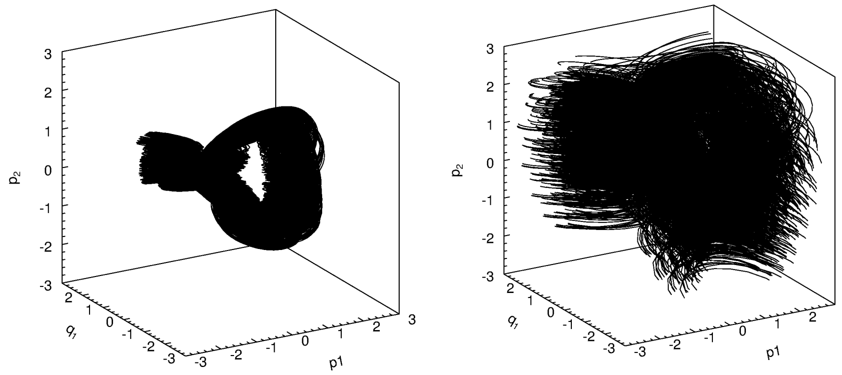

c) $k=1$ d) $k=3$

Fig.2. Phase portraits for regular (cases a, b) and chaotic regimes (cases c, d).

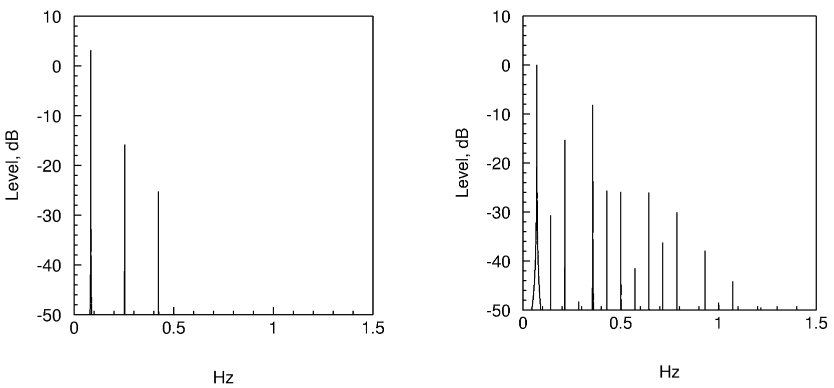

a) $k=0.5$ b) $k=0.8$

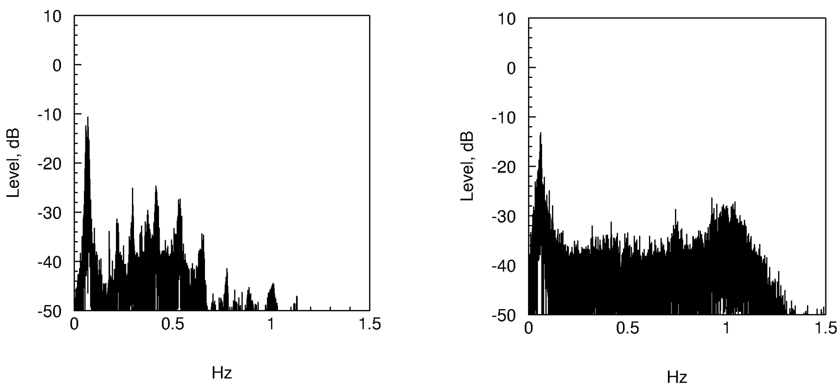

c) $k=1$ d) $k=3$

Fig. 3. Power spectra computed for p_1 data (cases a, b, c and d).

As we may conclude from numerical data and graphs in Figures 1-3 the dynamical system (9) has both regular (k=0.5; k=0.8) and chaotic regimes (k=1; k=3). The chaotic regimes could be realized when $k \geq 1$. For such values of corresponding amplitudes of wavemaker oscillations the largest Lyapunov exponents are positive, phase portraits have complicated structures of trajectory sets and power spectra are continuous ones.

3 Two Mode Approximation of Vibrations of Cantilever Bar with Low Bending Rigidity

It has been known that it is possible to stabilize a rigid pendulum and a flexible cantilever bar with very low bending rigidity vertically upwards under harmonic oscillations, Champneys, 2000, [2]. The nonlinear equation for flexible vibrations $\eta(x,t)$ of the cantilever bar can be written in the following form, Krasnopolskaya, 2013, [6]:

$$EJ_0 \frac{\partial^4 \eta}{\partial x^4} + \rho F g \frac{\partial}{\partial x}\left(\left[(l-x)+(l-x)\frac{\partial^2}{\partial t^2}\left(\frac{a}{g}\cos\omega t\right)\right]\frac{\partial \eta}{\partial x}\right) - \\ -3\alpha_3 E^3 J_2\left[\frac{\partial^4 \eta}{\partial x^4}\frac{\partial^2 \eta}{\partial x^2} + 2\left(\frac{\partial^3 \eta}{\partial x^3}\right)^2\right]\frac{\partial^2 \eta}{\partial x^2} + \rho F \frac{\partial^2 \eta}{\partial t^2} = 0. \tag{10}$$

In this equation EJ_0 is bending rigidity, ρ is the bar density, F is cross section area, a is an amplitude (ω is a frequency) of a clamped base oscillations, l is a bar length, $\alpha_3 E^3 J_2$ is a constant coefficient due to nonlinear stiffness of the bar. Our experiments revealed that oscillations of the bar can be approximated by two eigenmode oscillations, namely, by the second and the third eigen modes, Krasnopolskaya, 2012, [5] when the second eigen frequency is close to a half of ω and in three times smaller than the third eigenfrequency. In this case we may write

$$\eta = \varepsilon\left[A_2(\tau)\cos\frac{\omega t}{2} + B_2(\tau)\sin\frac{\omega t}{2}\right]\varphi_2(x) + \\ \varepsilon\left[A_3\cos\frac{3\omega t}{2} + B_3\sin\frac{3\omega t}{2}\right]\varphi_3(x) \tag{11}$$

Here ε is the small parameter, $\varphi_2(x)$ is the second eigenmode, $\varphi_3(x)$ is the third eigenmode, Krasnopolskaya, 2012, [5].

By substitution of the expressions (11) into the equation (10) and averaging over the fast time we get

$$\frac{dA_2}{d\tau}=-\frac{\xi_2}{2\omega}A_2+\frac{1}{\omega^2}\left\{\frac{\gamma_1}{2}B_2-\frac{\gamma_2}{2}B_3-\xi(\omega)B_2-2I_3\gamma_0\left[\frac{3}{8}\alpha_5B_2\left(A_2^2+B_2^2\right)\right.\right.$$

$$\left.\left.+\frac{\alpha_6}{8}\left(A_2^2B_3-B_2^2B_3+2A_2B_2A_3\right)+\frac{\alpha_7}{4}B_2(A_3^2+B_3^2)\right]\right\};$$

$$\frac{dB_2}{d\tau}=-\frac{\xi_2}{2\omega}B_2+\frac{1}{\omega^2}\left\{\frac{\gamma_1}{2}A_2+\frac{\gamma_2}{2}A_3+\xi(\omega)A_2+2I_3\gamma_0\left[\frac{3}{8}\alpha_5A_2\left(A_2^2+B_2^2\right)\right.\right.$$

$$\left.\left.+\frac{\alpha_6}{8}\left(A_2^2A_3-B_2^2A_3+2A_2B_2B_3\right)+\frac{\alpha_7}{4}A_2(A_3^2+B_3^2)\right]\right\};$$

$$\frac{dA_3}{d\tau}=-\frac{\xi_2}{2\omega}A_3+\frac{1}{\omega^2}\left\{-\frac{\gamma_3}{6}B_2-\xi_3(\omega)B_3-\frac{2}{3}I_3\gamma_0\left[\frac{\alpha_9}{8}\left(3A_2^2B_2-B_2^3\right)+\right.\right.$$

$$\left.\left.+\frac{\alpha_{10}}{8}B_3\left(A_2^2+B_2^2\right)+\frac{3\alpha_{12}}{8}B_3(A_3^2+B_3^2)\right]\right\};$$

$$\frac{dB_3}{d\tau}=-\frac{\xi_2}{2\omega}B_3+\frac{1}{\omega^2}\left\{+\frac{\gamma_3}{6}A_2+\xi_3(\omega)A_3+\frac{2}{3}I_3\gamma_0\left[\frac{\alpha_9}{8}A_2\left(A_2^2-3B_2^{\,2}\right)+\right.\right.$$

$$\left.\left.+\frac{\alpha_{10}}{8}A_3\left(A_2^2+B_2^2\right)+\frac{3\alpha_{12}}{8}A_3(A_3^2+B_3^2)\right]\right\};$$

In our calculations the following parameters have been used

ρ = 1.7*10^{-3} *kg/см^3*; g = 980 *см/sec^2*; *a* = 0.9*см*; B =0.055; *l* = 26.7*см*;
r = 0.15 *см*; G = 0.1398*10^9 kg/(см g sec^2); g_2 = 0.0547 g10^6;
λ_2 = 18.031; λ_3 = 184.32; *E*=1.4227*10^5*kg/(см gsec^2*),

$$\xi_2=\frac{8.0\cdot 10^{-5}}{\rho Fl}=0.17\sec^{-1},\quad \gamma_0=\frac{g}{l},\ \alpha_3^*=\frac{2}{27}\frac{Eg_2}{G^3},$$

$$I_3=5B\alpha_3^*E^2\cdot 10^{-5},\quad \xi(\omega)=\frac{g}{2A}-\frac{g}{A\omega}\sqrt{\frac{g\lambda_2}{l}},$$

$$\xi_3(\omega)=\frac{3g}{2A}-\frac{g}{A\omega}\sqrt{\frac{g\lambda_3}{l}}.$$

Only regular regimes were found for different initial conditions as steady state regimes. The maximum Lyapunov exponents were not positive for all of them. In Figure 4 phase portrait projections are shown for quasi-periodic (ω=40 *rad/sec*) and periodic (ω=60 *rad/sec*) regimes. Power spectra for these regimes are presented in Figure 5, where only several spikes are visible. Quasi-periodic and periodic regimes are typical for the above-mentioned dynamic system which has a symmetry relatively unknown variables.

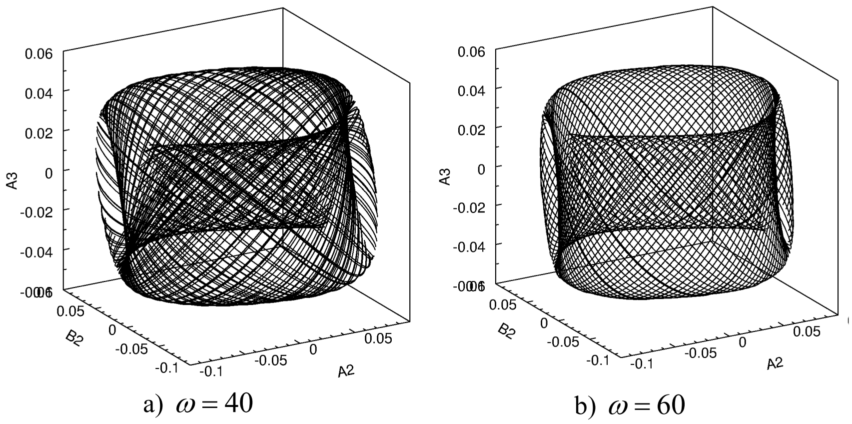

Fig. 4. Phase portraits for different excitation frequencies.

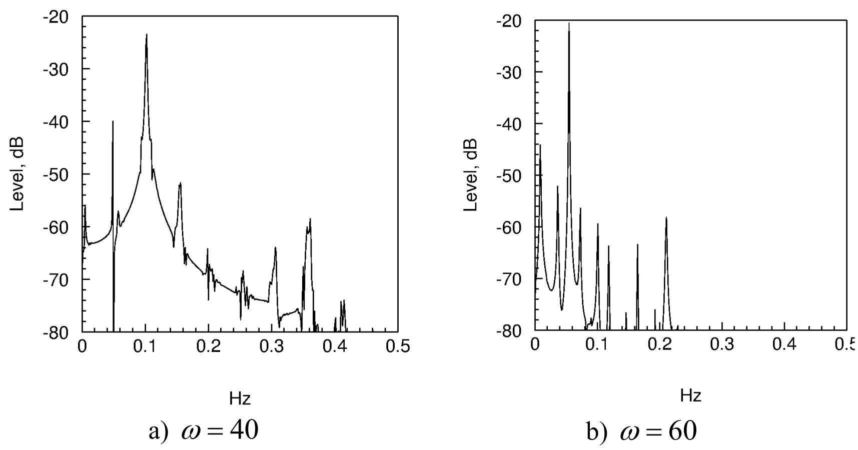

Fig. 5. Power spectra computed for A_2 time realization for different frequencies of clamped base oscillations.

4 Conclusions

Two new models expressing interaction of two eigenmodes at the condition of internal resonances and parametric oscillations of continuous systems are developed. Models are simulated. The existence of chaotic attractors was established for the dynamical system presenting cross-waves and forced waves interaction at fluid free-surface in a volume between two cylinders of finite length. For averaged symmetric systems describing two parametric eigen modes of a flexible cantilever bar with very low bending rigidity no chaotic regimes were found.

References

1. J.M. Becker and J.M. Miles. Standing radial cross-waves. *Journal of Fluid Mechanics,* vol. 222, 471-499, 1991.
2. A. Champneys and B. Fraser. The ‘Indian rope trick’ for a parametrically excited flexible rod: linearized analysis. *Proc. R. Soc. London*, vol. 456, 553-570, 2000.
3. M. Faraday. On a peculiar class of acoustical figures; and on certain forms assumed by groups of particles upon vibrating elastic surface, *Philosophical Transactions of Royal Society of London A,* vol. 121, 299-340, 1831.
4. T.S. Krasnopolskaya and F.G.J. van Heijst. Wave pattern formation in a fluid annulus with a vibrating inner shell. *Journal of Fluid Mechanics,* vol. 328, 229-252, 1996.
5. T.S. Krasnopolskaya, D.F. Prykhodko and A.A. Gourjii. Dynamic characteristics of a cantilever bar with low bending rigidity. *Bulletin of Taras Shevchenko National University of Kiev, Series Physics & Mathematics,* no. 4, 52-52, 2012.
6. T.S. Krasnopolskaya, D.F. Prykhodko and A.A. Gourjii. Nonlinear models of vibrations of cantilever bar with low bending rigidity. *Bulletin of Taras Shevchenko National University of Kiev, Series Physics & Mathematics,* no. 2, 158 -161, 2013.
7. G. Lamé. *Leçons sur la Théorie Mathématique de l’Élasticité des CorpsnSolids,* C. Bachelier, Paris, 1852.

Chaotic Modeling and Simulation (CMSIM) 3: 423–430, 2013

On Utilizing Nonlinear Interdependence Measures for Analyzing Chaotic Behavior in Large-Scale Neuro-Models

Dragos Calitoiu[1] and B. J. Oommen[1,2]

[1] School of Computer Science, Carleton University, 1125 Colonel By Drive, Ottawa, ON, Canada, K1S 5B6
(E-mail: dcalitoi@scs.carleton.ca)
[2] University of Agder, Postboks 509, 4898 Grimstad, Norway
(E-mail: oommen@scs.carleton.ca)

Abstract. In this paper we present a comparison between a nonlinear measure (the Nonlinear Interdependence, S) and a linear measure (the Cross Correlation coefficient, CC) for analyzing nonlinear dynamical systems. To do this, we consider a biologically-realistic neural network (NN) model of the piriform cortex. Our previous work studied the EEGs obtained from two components of this network. In this current work, we increase the system's granularity and replicate the exploration using the membrane potentials of our neurons to study the measures S and CC. To be more specific, even though the properties of a nonlinear dynamical system are best analyzed in the natural framework described by its state space, they may be undetectable in the time domain of the system's output, e.g., in the EEG tracing. Rather, a phase space representation may reveal the salient features of the nonlinear structure which are hidden or occluded to standard linear approaches. Nonlinear Interdependence, (S), proposed by Quiroga, is said to occur when the trajectories reconstructed in the phase-space of one time series, experimentally predict the evolution of the phase space trajectories of the second time series. This measure of predictability has the advantage over linear measures, of being sensitive to interdependence between dissimilar types of activity. In many cases where one analyzes nonlinear signals, CC is a measures that well describes the synchronization or the desynchronization between two signals. In other cases, S is introduced in addition to CC in order to describe the nonlinear signals. We thus investigate here the synchronization of these types of signals using the membrane potentials using both linear measures (i.e., CC) and nonlinear measures (i.e., S). Our results clearly prove that utilizing *both* these measures is effective in analyzing and understanding real-life chaotic systems.
Keywords: Chaotic Behavior, Large-scale Neuro-Models, Nonlinear Interdependence (S) Measure.

Received: 14 March 2013 / Accepted: 10 July 2013

ISSN 2241-0503

A preliminary version of this paper was presented at CHAOS'13, the 2013 Chaotic Modeling and Simulation International Conference, in Istanbul, Turkey, in June 2013.

1 Introduction

From the theory of nonlinear dynamics [7], we understand that nonlinear dynamical systems can be aptly and best described and quantified by a state space. This is also the natural framework to characterize its underlying phenomena. However, while their properties may be undetectable in the system's time domain output (e.g., in the EEG tracing), they can be studied in the phase space. A phase space representation may reveal the salient features of the nonlinear structure which are hidden or occluded to standard linear approaches [11]. In this context, Nonlinear Interdependence is said to occur when the trajectories reconstructed in the phase-space of one time series experimentally predict the evolution of the phase space trajectories of the second time series [10]. This measure of predictability has the advantage over linear measures, of being sensitive to the interdependence between *dissimilar* types of activity [3].

Often, in the analysis of nonlinear signals, a linear measure (the Cross Correlation coefficient, CC) is a measure that aptly describes the synchronization or the desynchronization between two signals. In other cases, the Nonlinear Interdependence, S, is introduced in addition to CC in order to describe the nonlinear signals. In this paper we present a comparison between S and CC. We shall demonstrate that whenever we are dealing with signals with a "dominant" nonlinear behavior and with a very small linear component, neither S nor CC, by themselves, can provide the same information as the pair $\langle$S, CC $\rangle$.

To demonstrate this hypothesis, we shall investigate a biologically realistic Neural Network (NN) model of the piriform cortex. In our previous work [4], we studied the EEGs obtained from two components of this network. In this current work, we increase the granularity of our approach and replicate the exploration using some previously unexplored criteria, i.e., the *membrane potentials* of our neurons. We thus investigate here the synchronization of these types of signals using the membrane potentials, wherein we utilize both a typical linear measure (i.e., CC) and a typical nonlinear measure (i.e., S). We also compare the synchronization identified between the potentials in this manner, with the one identified between the EEGs.

The issue of neuro-modeling is not merely theoretical. Indeed, is has been motivated by a desire to better understand specific neural circuits, particularly those whose failures could possibly trigger human illnesses. Depression, Anxiety, Schizophrenia, Alzheimer's disease, memory impairment, paralysis, Epilepsy, Multiple Sclerosis, Parkinson's disease, etc. are areas in which intense research efforts have been (and are being) made to better understand and treat these conditions. In this respect, from a modeling perspective, the analysis of the *connections* between the neurons is fundamental to understanding and treating these illnesses. Such an analysis also leads to a better understanding of the development and function of the normal brain.

1.1 The Platform: GENESIS and the Computational Model

The platform for our research is the so-called GENESIS (GEneral NEural SImulation System) framework [2] proposed by Bower *et al.* This simulation software

The GENESIS simulation software is free and can be downloaded from `http://www.genesis-sim.org/GENESIS/`.

was initially developed in a CALTECH (California Institute of Technology) laboratory by Wilson [13] as an extension of efforts to model the olfactory cortex. It was designed to allow for the multi-scale modelling of a single simulation system and, until now, is the only simulator possessing this capacity. Indeed, in this context, the Wilson model of the piriform cortex is generally accepted as a realistic model, since it is based on the anatomical structure, apart from which it also contains physiological characteristics of actual biological networks. The model has been cited in more than 100 refereed papers, and a review of large scale brain simulations is found in [5].

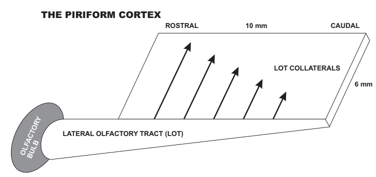

Fig. 1. The model of the piriform cortex.

One of the ultimate objectives of Wilson's model was to understand the role of the piriform cortex in olfactory object recognition. Further, one motivation of the research due to Wilson and Bower was the assumption that this cortex computationally represents a type of associative memory. The model has been used to explore a wide range of cortical behaviors [13], including associative memory functions [12].

The computational model which we present can be viewed as a nonlinear system. Simulation of the piriform cortex requires the numerical solutions of *systems* of differential equations that describe the states of the neurons as a function of time and space. These numerical techniques describe how the system advances the state variables of the simulation (e.g., the potential of the membrane) from time i to time $i+1$, through numerical integration of the differential equations that appropriately describe the system. The computational model of the piriform cortex is treated as a loosely-coupled system of ordinary differential equations. The evaluation of a state of any neuron in the system requires only the information of the previous states from other neurons, and it can be solved for each neuron at every time step. It is well known that such equations can be solved using straightforward numerical integration techniques.

The initial architecture consists of three 15 $\times$ 9 arrays of 135 nodes. Each array has only a *single* type of neuron, being either of the pyramidal cells, of the feedforward inhibitory cells (K^+ mediated inhibition), or of the feedback inhibitory cells (Cl^- mediated inhibition). The array is proposed to represent the whole piriform cortex, which falls within an area of approximately 10 mm $\times$ 6 mm. The pyramidal cells consist of five compartments, with each compartment receiving a distinct kind of synaptic input. The inhibitory cells are modelled using the differences between the exponential functions. The model also contains 10 cells representing the excitatory input from the olfactory bulb to the cortex.

Numerous models of brain circuitry have focused on simulating the macroscopic functionality of systems containing simplified neuronal units. The increase in computational power in the last decade has permitted simulations to include models with considerable complexity, namely those comprising of *realistic* large scale NNs. The goal of a modeling phase is to generate patterns that are similar to EEGs, and to explore their possible physiological basis.

2 Problem of Connectivity

The **Problem of Connectivity** is motivated from the following clinical considerations. In spite of intensive research conducted over the last decades and the discovery of effective medication, the cause and the mechanisms leading to Schizophrenia are still unclear. It is widely agreed that Schizophrenia is most likely based on fundamental neuronal changes of the brain. Unfortunately, physiological methodologies have not been able to contrive reliable tests beside the current assessments. Perhaps the high complexity of the human brain is what renders it vulnerable to diseases such as Schizophrenia, because animals do not develop the same types of diseases [6].

This problem involves investigating the modification of local connectivity within the piriform cortex. More specifically, we analyze the dependence of the level of chaos as a function of the density of the synapses (i.e, the number of synapses generated between the neurons). In addition, we investigate the variation of the maximum Nonlinear Interdependence, S, of two sub-systems embedded in a larger system. Thus, we consider how the coupling of two interconnected sub-systems of the same underlying system would change as a function of the connectivity of the synapses. We believe that the levels of local connections between the neurons can be used as a hypothesis for the mechanism to explain underlying illnesses such as Schizophrenia.

Prior Work on the Problem of Connectivity: In our prior research [4], we have performed modifications to the number of connections between the pyramidal neurons. By changing the connectivity, we proposed to simulate the level of pruning to be excessive or insufficient. We chose to describe the effect of pruning on the level of chaos and the degree of synchronization between the two sub-systems embedded in the piriform cortex model, using three measures: the LLE, S, and CC. These three measures were chosen based on two hypotheses. First of all, schizophrenic symptoms, like thought disorder, hallucinations and delusions, are assumed to be dependent on the level of chaos in the brain. Secondly, the symptoms are triggered by the existence of false attractors near "good" attractors, which suggests that areas from the brain could be highly correlated in an unhealthy manner. To our knowledge, the investigation of the two theories, namely excessive and insufficient pruning, based on these three measures, is new.

The uniqueness of our research is strengthened by the fact that the pairs of signals being compared belong to the same system. Other authors [8–10], have considered two initially independent systems and partially coupled them; subsequently, they have analyzed the synchronization of the signals obtained from the two systems. In contrast to previous models that evaluate relationships between two different systems (or rather, two partially coupled systems), we have proposed a new approach where the investigation is conducted using two sub-systems which are embedded within the context of a larger system, namely, two coupled sub-systems of the same system.

2.1 Current Work: Problem of Connectivity

To present our current work in the right perspective, it is appropriate for us to mention how the readings and measurements are taken and recorded. Recordings from the array are averaged to produce the EEGs as below:

$$EEG(t+1) = \frac{1}{m}\sum_{i=1}^{m}[\Phi_i(t)], \tag{1}$$

where m is the number of electrodes, and $\Phi_i(t)$ is the field potential depending of the output of the pyramidal neurons, $X^p(t)$ for $p = 1 \cdots N$. We assume that the influence of the inhibitory neurons is marginal in the process of the EEG computation, and that it can thus be omitted.

The relation between the field potential, $\Phi_i(t)$, recorded from the electrode i and the output of the pyramidal neurons $X^p(t)$ is:

$$\Phi_i(t) = \frac{1}{4\Pi}\sum_{p=1}^{N}\frac{X^p(t)}{d_{pi}}, \tag{2}$$

where N is number of pyramidal neurons, and d_{pi} is the distance of the p^{th} pyramidal neuron from the recording site (the electrode i).

By examining the above equations, the reader can see that the synchronization of the EEGs implies the evaluation of the *aggregated* signals, which is achieved by computing the averages of a certain number of fields (in our setting the number is 8). These fields are, in turn, obtained by weighting the membrane potentials with the inverses of the distances between the electrodes and each neuron, which is considered as a contributor in the EEG. However, prior to the averaging phase, one observes that the computational model of the piriform cortex yielded access to the raw data in and of itself, namely the *original* membrane potential of each neuron. From the perspective of understanding the efficiency of the CC and S measures, in our current work we disaggregate the signals and explore the behavior of the raw data (i.e., the membrane potentials) itself. To accomplish this for a *prima facie* study, we perform a careful selection of only *four* neurons as follows:
i. Two of them (V_1-V_2) were involved in the previous EEG_1 computation;
ii. One of them (V_{135}) was involved in the computation of the EEG_2;
iii. The last (V_{15}) was not involved in the previous computations.
Using these selection criteria, we now investigate all the possible synchronization scenarios (i.e., the intra-EEG and the inter-EEG electrode readings).

2.2 The Settings

In our research, we considered two zones of the piriform cortex as depicted in Figure 1. For each zone, which was treated as a sub-system, we analyzed the artificially generated EEGs, each of them being computed with a fixed number of electrodes, and at a suitable frequency.

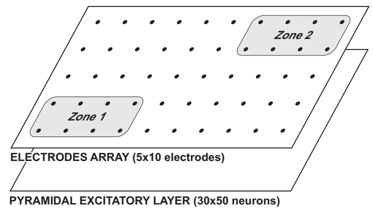

Fig. 2. The distribution of the electrodes in Zone1 and Zone2.

We considered the density of the synapses corresponding to the pyramidal neurons as a control parameter, and explored the effect of modifying the initial values suggested by the Wilson model [13]. This, in turn, involved:

1. The computation of the EEGs as function of the number of electrodes for each sub-system.
2. The determination of the optimum value for the embedding dimension for the phase space reconstruction using the FNN method *for the density of the synapses.*
3. The computation of the CC and S measures *between* the EEGs and for the membrane potentials.

2.3 Results for this Problem

We conducted numerous simulations over an ensemble of settings. However, we merely report here some representative results.

First of all, we mention that the time series used to describe the systems are the EEGs and membrane potentials. To obtain these, we used an array of n evenly spaced electrodes on the surface of the simulated cortex. Recordings from the array were then averaged to produce the EEGs. In our experiments, we set $n = 50$.

We investigated the level of chaos and the synchronization between these two zones of the piriform cortex, when the efficiency of the pruning was higher or smaller than 50%, implying that we decreased, and also increased the connectivity between the pyramidal cells. The level of connectivity was described by the maximum number of possible connections between the pyramidal neurons, where the possible values were $p = 0.1$, 0.2, 0.5, 1, 2, and 10. The case of the healthy brain, when the efficiency of pruning is 50%, corresponds to the setting when $p = 1$.

For each sub-system we analyzed the artificially generated EEGs, each of them computed with 8 electrodes. We also analyzed the membrane potentials for four neurons: V_1 and V_2 involved in the computation of EEG1 for $Zone_1$, V_{135} involved in the computation for the EEG2 for $Zone_2$, and V_{15} not involved in the computation of EEG1 or EEG2. The EEGs and the membrane potentials were recorded at 5,000 samples/sec for a duration of half of a second.

The first experimental step was to compute the optimum embedding dimension for each zone, using The False Nearest Neighbor (FNN) Statistics. In the interest of brevity, we will not present these results here.

To evaluate the interdependence between the artificially generated EEGs and between the membrane potentials, as mentioned earlier, we used two metrics, namely S and CC. For computing CC we used a lag which ranged between -100 and +100. The absolute value is reported. The evolution of S and CC function of connectivity between pyramidal cells are presented in Table 1, in which we report the averages for 20 experiments, each of them conducted with a different model.

		V_1-V_{15}		V_2-V_{15}		V_1-V_{135}		V_2-V_{135}		EEG1 *vs* EEG2
Weights	CC_{max}	$S(X,Y)$	CC_{max}	$S(X,Y)$	CC_{max}	$S(X,Y)$	CC_{max}	$S(X,Y)$	CC_{max}	$S(X,Y)$
0.1	0.9678	0.2341	0.9668	0.2366	0.9680	0.2439	0.9692	0.246	0.5005	0.2396
0.5	0.6600	0.1094	0.6539	0.1117	0.7300	0.212	0.8032	0.2170	0.6204	0.2870
1	0.1386	0.0797	0.2111	0.0671	0.1380	0.0823	0.1872	0.0680	0.2227	0.1112
1.5	0.1439	0.0234	0.1419	0.0215	0.2526	0.0390	0.2158	0.0330	0.2524	0.2607

Table 1. Nonlinear Interdependence (S) and maximum Cross Correlation Coefficient (CC_{max}) for membrane potentials (V_1-V_{15}, V_2-V_{15}, V_1-V_{135}, and V_2-V_{135}) and for EEG1 and EEG2 function of the value of the connectivity between the pyramidal cells.

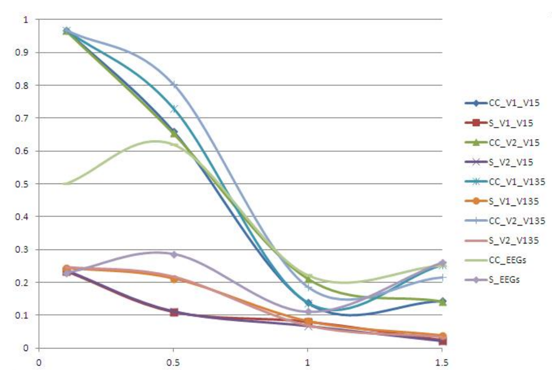

Fig. 3. The evolution of $S(X|Y)$ and CC as a function of the level of connectivity between the neurons (see Table 1.)

2.4 Discussion of Results

Table 1 and Figure 2 are used for analyzing the two behaviors, namely that of increasing and decreasing the connectivity levels. Table 1 contains the averages of the CC and S measures computed with membrane potentials (the first 8 columns) and the averages computed with the EEG signals (reported earlier in [4]). The reader can see that the computation used to obtain the EEG affects the ranges of the CC and S measures, namely it decreases the ranges, compared to the ranges of the CC and S measures computed with the membrane potentials. To be more specific, the CC ranges are 0.8306 for the membrane potentials and 0.3977 for the EEGs , while the S measure ranges are 0.2245 for the membrane potentials and 0.1758 for the EEGs. With regard to the degree of synchronization represented by the Nonlinear Interdependence

S, only a decrease in the connectivity leads to a consistent modification, again as displayed in Figure 2.

3 Conclusions

The analysis of the two behaviors, namely that of increasing and decreasing the connectivity levels, reveals that both of them determine a decrease in the level of chaos in the system, as seen in Figure 2.

From these observations, we can conclude that whenever we are dealing with signals with a "dominant" nonlinear behavior and with a very small linear component, neither S nor CC, by themselves, can provide the same information as the pair $\langle$S, CC $\rangle$.

References

1.J. Arnold, P. Grassberger, K. Lehnertz, and C. E. Elger. A robust method for detecting interdependences: application to intracranially recorded EEG. *Physica D*, 134:419–430, 1999.
2.J.M. Bower and D. Beeman. The Book of GENESIS. Springer TELOS, 1998.
3.M. Breakspear and J. R. Terry. Topographic orientation of nonlinear interdependence in multichanel human EEG. *Neuroimage*, 16:822–835, 2002.
4.D. Calitoiu, B.J. Oommen, and D. Nussbaum. Large scale neuro-modeling for understanding and explaining some brain-related chaotic behavior. *Simulation: Transactions of the Society for Modeling and Simulation International*, 88:1316–1337, 2012.
5.H. deGaris, S. Chen, B. Goertzel, and R. Lian. A world survey of artificial brain projects, Part I: Large-scale brain simulations. *Neurocomputing*, 74:3–29,2010.
6.A. Fell. The Disorder Mind. *UC Davis Magazine*, 19:1–7, 2001.
7.A. V. Holden. *Chaos - Nonlinear Science: Theory and Applications*. Manchester University Press, 1986.
8.L. M. Pecora. Synchronization conditions and desynchronizating patterns in coupled limited-cycle and chaotic systems. *Physical Review E*, 58:347–360, 1998.
9.R. Q. Quiroga, J. Arnold, and P. Grassberger. Learning driver-response relationships from synchronization patterns. *Physical Review E*, 61:5142–5148, 2000.
10.S. F. Schiff, P. So, and T. Chang. Detecting dynamical interdependence and generalized synchrony through mutual prediction in a neural ensemble. *Physical Review E*, 54:6708–6724, 1996.
11.C. J. Stam. Nonlinear dynamical analysis of EEG and MEG. Review of an emerging field. *Clinical Neurophysiology*, 116:2266–2301, 2005.
12.M. Wilson and J. M. Bower. A computer simulation of olfactory cortex with functional implications for storage and retrieval of olfactory information. *Neural Information Processing Systems*, edited by D. Anderson, American Institute of Physics, New York, 114–126, 1988.
13.M. Wilson and J.M. Bower. The simulation of large-scale neural networks. *Methods in Neuronal Modelling: From Synapses to Networks*, edited by C. Koch and I. Segev, Cambridge, MA: MIT Press, 291–334, 1989.

Chaotic Modeling and Simulation (CMSIM) 3: 431–439, 2013

Central Configurations in a symmetric five-body problem

Muhammad Shoaib[1], Anoop Sivasankaran[2], and Yehia A. Abdel-Aziz[1,3]

[1] University of Hail, Department of Mathematical Sciences PO BOX 2440, Saudi Arabia
(E-mail: safridi@gmail.com)
[2] Khalifa University, Department of Applied Mathematics and Sciences, PO Box:573, Sharjah, UAE
(E-mail: anoop.sivasankaran@kustar.ac.ae)
[3] National Research Institute of Astronomy and Geophysics (NRIAG), Cairo, Egypt
(E-mail: yehia@nriag.sci.eg)

Abstract. A central configuration $q = (q_1, q_2, ..., q_n)$ is a particular configuration of the n-bodies where the acceleration vector of each body is proportional to its position vector and the constant of proportionality is the same for n-bodies. In the three-body problem, it is always possible to find three positive masses for any given three collinear positions given that they are central. This is not possible for more than four-body problems in general. In this paper we model a symmetric five-body problem with with position coordinates for the five bodies as $(-x, 0), (0, y), (x, 0), (0, -y)$ and (c_1, c_2). (c_1, c_2) is the centre of mass of the system. Regions of central configurations, where it is possible to choose positive masses, are derived using both analytical and numerical tools. We also identify regions in the phase space where no central configurations are possible. A certain relationship exists between the mass placed at the center of mass of the systems i.e (c_1, c_2) and the remaining four masses. This relationship is investigated both numerically and analytically. Similarly restrictions on the geometry and restrictions on the inter-body distances are investigated.
Keywords: Central Configurations, n-body problem, five-body problem, inverse problem of central configurations.

1 Introduction

The classical equation of motion for the n-body problem has the form

$$m_i \frac{d^2\mathbf{q}_i}{dt^2} = \frac{\partial U}{\partial q_i} = \sum_{j\neq i} \frac{m_i m_j\,(\mathbf{q}_j - \mathbf{q}_i)}{|\mathbf{q}_i - \mathbf{q}_j|^3} \qquad i = 1, 2, ..., n, \tag{1}$$

where the units are chosen so that the gravitational constant is equal to one, $\mathbf{q}_i$ is a vector in three space,

$$U = \sum_{1\preceq i<j\preceq n} \frac{m_i m_j}{|\mathbf{q}_i - \mathbf{q}_j|} \tag{2}$$

Received: 16 April 2013 / Accepted: 18 July 2013

ISSN 2241-0503

is the self-potential, $\boldsymbol{q}_i$ is the location vector of the ith body and m_i is the mass of the ith body.

A *central configuration* $q = (q_1, q_2, \cdots, q_n)$ is a particular configuration of the n-bodies where the acceleration vector of each body is proportional to its position vector, and the constant of proportionality is the same for the n-bodies, therefore

$$\sum_{j=1, j\neq i}^{n} \frac{m_j(\mathbf{q}_j - \mathbf{q}_k)}{|\mathbf{q}_j - \mathbf{q}_k|^3} = -\lambda(\mathbf{q}_k - \mathbf{c}) \qquad k = 1, 2, ..., n, \tag{3}$$

where

$$\lambda = \frac{U}{2I}, \qquad I = \sum_{i=1}^{n} m_i ||\mathbf{q}_i||^2, \text{ and } \mathbf{c} = \frac{\sum_{i=1}^{n} m_i \mathbf{q}_i}{\sum_{i=1}^{n} m_i}. \tag{4}$$

So far, in the non-collinear general four and five-body problems the main focus has been on the common question: For a given set of masses and a fixed arrangement of bodies does there exist a unique central configuration ([7],[6]). In this paper, we ask the inverse of the question i.e. given a four or five-body configuration, if possible, find positive masses for which it is a central configuration. Similar question has been answered by Ouyang and Xie (2005) for a collinear four body problem and by Mello and Fernades (2011) for a rhomboidal four and five-body problem. For other recent studies on the rhomboidal problem see [1],[2],[4], and [5]. In this paper we state and prove the following theorems.

Theorem 1. *Consider five bodies of masses* $(m_1, m_2, m_3, m_4, m_0)$ *located at* $(-x, 0), (y, 0), (x, 0), (0, -y)$ *and* $(0, 0)$ *respectively. The mass* m_0 *is taken to be stationary at the centre of mass of the system. Let* $m_1 = m_3 = 1, m_2 = m_4 = m$.

1. *In this particular set up, using polar coordinates, of the rhomboidal five body problem where* $m(\theta) > 0$, $m_0(\theta) > 0$ *and* $r = 1$ *will form central configuration when* $\theta \in (-1.94, -1.04) \cup (0.74, 1.04)$. *For all other values of* θ *at least one of the masses will become negative.*
2. *For* $r \neq 1$, *the central configuration region is given in figure (1).*

Theorem 2. *Let five bodies of masses* $m_1 = m_3 = M, m_2 = m_4 = m$ *be placed at the vertices* $m_1(-1, 0), m_2(y, 0), m_3(1, 0), m_4(0, -y)$ *and* $m_0(0, 0)$ *of a rhombus. The mass* m_0 *is taken to be stationary at the centre of mass of the system. There exist a region*

$$R_1 = (R_{1m} \cup R_{1m}^*) \cap (R_{1M} \cup R_{1M}^*). \tag{5}$$

in the ym_0-*plane where it is possible to choose positive masses which will make the configuration central, where*

$$\begin{aligned} R_{1m} &= \{(y, m_0) | m_0 > \frac{y^3\left(8 - \left(1+y^2\right)^{3/2}\right)}{-8y^3 + \left(1+y^2\right)^{3/2}} \\ &\quad \textit{and} \;\; y \in (0, 2-\sqrt{3}) \cup (2+\sqrt{3}, \infty)\}, \end{aligned} \tag{6}$$

$$R^*_{1m} = \{(y, m_0)|m_0 < \frac{y^3\left(8 - \left(1 + y^2\right)^{3/2}\right)}{-8y^3 + (1 + y^2)^{3/2}} \textit{ and } y \in (2 - \sqrt{3}, 2 + \sqrt{3})\}, \tag{7}$$

$$R_{1M} = \{(y, m_0)|m_0 > \frac{8y^3 - \left(1 + y^2\right)^{3/2}}{-8 + (1 + y^2)^{3/2}} \tag{8}$$

$$\textit{and } y \in (0, 2 - \sqrt{3}) \cup (2 + \sqrt{3}, \infty)\},$$

$$R^*_{1M} = \{(y, m_0)|m_0 < \frac{8y^3 - \left(1 + y^2\right)^{3/2}}{-8 + (1 + y^2)^{3/2}} \textit{ and } y \in (2 - \sqrt{3}, 2 + \sqrt{3})\}. \tag{9}$$

In the complement of this region no central configurations exist for $m, m_0 > 0$.

Theorem 3. *Consider five bodies of masses* $(m_1, m_2, m_3, m_4, m_0)$ *located at* $(-x, 0), (y, 0), (x, 0), (0, -y)$ *and* $(0, 0)$ *respectively. The mass* m_0 *is taken to be stationary at the centre of mass of the system. Let* $m_1 = m_3 = M, m_2 = m_4 = m$. *There exist a region*

$$R_3 = ((R_d \cap R_{3m}) \cup (R^c_d \cap R^c_{3m})) \cap (R_d \cap R_{3M}) \cup (R^c_d \cap R^c_{3M}), \tag{10}$$

in the $xy-$*plane where it is possible to choose positive masses which will make the configuration central. Here*

$$R_{3m} = \{(x, y)|r(x, y) > 2y\sqrt[3]{\frac{m_0 + x^3}{m_0 + y^3}}, x > 0, y > 0, m_0 > 0\}, \tag{11}$$

$$R_{3M} = \{(x, y)|r(x, y) > 2x\sqrt[3]{\frac{m_0 + y^3}{m_0 + x^3}}, x > 0, y > 0, m_0 > 0\}. \tag{12}$$

In the complement of this region no central configurations exist for $M, m, m_0 > 0$.

Let's consider five bodies of masses m_i, $i = 0, 1, 2, 3, 4$. Four of the masses are placed at the vertices of a rhombus and the fifth mass m_0 is stationary at the centre of mass of the system. The coordinates for the five bodies are chosen as below:

$$\mathbf{q}_0 = (c_1, c_2), \mathbf{q}_1 = (-x, 0), \mathbf{q}_2 = (0, y), \tag{13}$$

$$\mathbf{q}_3 = (x, 0), \mathbf{q}_4 = (0, -y), \tag{14}$$

Using (3) and (13) we obtain the following equation for central configurations.

$$\frac{m_0\mathbf{q}_1}{x^3} + \frac{m_2\mathbf{q}_{12}}{\left(\sqrt{x^2 + y^2}\right)^3} + \frac{m_3\mathbf{q}_{13}}{8x^3} + \frac{m_4\mathbf{q}_{14}}{\left(\sqrt{x^2 + y^2}\right)^3} = -\lambda(\mathbf{q}_1 - \mathbf{c}), \tag{15}$$

$$\frac{m_0\mathbf{q}_2}{y^3} + \frac{m_1\mathbf{q}_{21}}{\left(\sqrt{x^2 + y^2}\right)^3} + \frac{m_3\mathbf{q}_{23}}{\left(\sqrt{x^2 + y^2}\right)^3} + \frac{m_4\mathbf{q}_{24}}{8y^3} = -\lambda(\mathbf{q}_2 - \mathbf{c}), \tag{16}$$

$$\frac{m_0\mathbf{q}_3}{x^3}+\frac{m_1\mathbf{q}_{31}}{8x^3}+\frac{m_2\mathbf{q}_{32}}{\left(\sqrt{x^2+y^2}\right)^3}+\frac{m_4\mathbf{r}_{34}}{\left(\sqrt{x^2+y^2}\right)^3}=-\lambda(\mathbf{q}_3-\mathbf{c}), \tag{17}$$

$$\frac{m_0\mathbf{q}_4}{y^3}+\frac{m_1\mathbf{q}_{41}}{\left(\sqrt{x^2+y^2}\right)^3}+\frac{m_2\mathbf{q}_{42}}{8y^3}+\frac{m_3\mathbf{q}_{43}}{\left(\sqrt{x^2+y^2}\right)^3}=-\lambda(\mathbf{q}_4-\mathbf{c}). \tag{18}$$

2 Proof of Theorem 1.

Let $m_1 = m_3 = 1, m_2 = m_4 = m$. As CC's are invariant up to translation and re-scaling therefore we assume that the centre of mass is at the origin. This assumption leads to some simplifications in the CC equations. Therefore from the four CC equations ((15 to 18) the following two linearly independent equations are obtained.

$$-\frac{1}{4x^2}+\frac{m_0}{x^2}-\frac{2mx}{(x^2+y^2)^{3/2}}=-x\lambda, \tag{19}$$

$$\frac{m}{4y^2}-\frac{m_0}{y^2}+\frac{2y}{(x^2+y^2)^{3/2}}=y\lambda. \tag{20}$$

Let $\lambda = 1$. Equations (19 and 20) are solved to obtain m and m_0 as functions of $x > 0$ and $y > 0$.

$$m(x,y)=\frac{8y^3-\left(x^2+y^2\right)^{3/2}(1-4x^3+4y^3)}{8x^3-(x^2+y^2)^{3/2}} \tag{21}$$

$$m_0(x,y)=\frac{32x^3y^3(2-\left(x^2+y^2\right)^{3/2})-\left(x^2+y^2\right)^3(1-4x^3)}{4\left(x^2+y^2\right)^{3/2}\left(8x^3-(x^2+y^2)^{3/2}\right)}. \tag{22}$$

It is not possible to explicitly solve for x and y therefore we use polar coordinates to re-write $m(x,y)$ and $m_0(x,y)$ as $m(r,\theta)$ and $m_0(r,\theta)$, where $x = r\cos\theta$ and $y = r\sin\theta$.

$$m(r,\theta)=\frac{1+4r^3\cos^3\theta-4\left(2+r^3\right)\sin^3\theta}{1-6\cos\theta-2\cos 3\theta}. \tag{23}$$

$$m_0(r,\theta)=\frac{\left(1-6\sin 2\theta+2\sin 6\theta-r^3(3\cos\theta-3\sin 2\theta+\cos 3\theta+\sin 6\theta)\right)}{4\left(1-6\cos\theta-2\cos 3\theta\right)}. \tag{24}$$

Let $r = 1$. The denominator of both $m(\theta)$ and $m_0(\theta)$ becomes zero at $\theta = -\frac{\pi}{3}, \frac{\pi}{3}$. The denominator is negative when $\theta \in (-\frac{\pi}{3}, \frac{\pi}{3})$ and is positive elsewhere. The numerator of $m(\theta)$ when $r = 1$ is given by $1 + \cos^3\theta - 12\sin^3\theta$. This has real zeros at $\theta = -2.61$ and $\theta = 0.673$. The numerator is positive

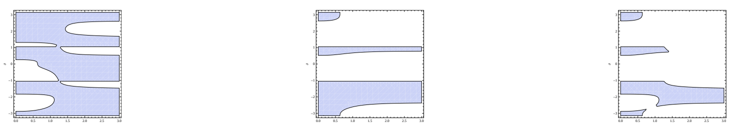

Fig. 1. left: $m_0(r,\theta) > 0$. **Centre:** Region, when $m(r,\theta) > 0$ **Right:** Region, when $m_0(r,\theta) > 0$ and $m(r,\theta) > 0$

when $\theta \in (-2.61, 0.673)$. Therefore $m(\theta)$ is positive when $\theta \in (-2.61, -1.04) \cup (0.673, 1.04)$.

The numerator of $m_0(\theta)$ when $r = 1$ is given by $-1 + 3\cos\theta + \cos 3\theta + 3\sin 2\theta - \sin 6\theta$. This has real zeros at $\theta = -2.541$, $\theta = -1.935$, $\theta = -0.449$, and $\theta = 1.248$. The numerator of $m_0(\theta)$ is positive when $\theta \in (-\pi, -2.54) \cup (-1.935, -0.449) \cup (1.248, \pi)$. Therefore $m_0(\theta)$ is positive when $\theta \in (-\pi, -2.54) \cup (-1.935, -1.04) \cup (-0.449, 1.04) \cup (1.248, \pi)$.

Hence, this particular set up of the rhomboidal five body problem where $m(\theta) > 0$, $m_0(\theta) > 0$ and $r = 1$ will form central configuration when $\theta \in (-1.94, -1.04) \cup (0.74, 1.04)$. For all other values of θ at least one of the masses will become negative.

In the case when $r \neq 1$,The central configuration region is given in figure (1)

3 Proof of Theorem 2.

Let $\lambda = x = 1$. Solve equations (19 and 20) to obtain m and M as functions of m_0 and y .

$$m(y, m_0) = \frac{4\left(1+y^2\right)^{3/2} N_m(y, m_0)}{(1-4y+y^2)\left(1+4y+18y^2+4y^3+y^4\right)}, \tag{25}$$

$$M(y, m_0) = \frac{4\left(1+y^2\right)^{3/2} N_M(y, m_0)}{(1-4y+y^2)\left(1+4y+18y^2+4y^3+y^4\right)}, \tag{26}$$

where

$$\begin{aligned} N_m(y, m_0) = {} & y^3\left(-2+\sqrt{1+y^2}\right)\left(5+y^2+2\sqrt{1+y^2}\right) \\ & +m_0\left(\left(-2y+\sqrt{1+y^2}\right)\left(1+5y^2+2y\sqrt{1+y^2}\right)\right), \end{aligned} \tag{27}$$

$$
\begin{aligned}
N_M(y,m_0) = & \left(-2y+\sqrt{1+y^2}\right)\left(1+5y^2+2y\sqrt{1+y^2}\right) \\
& +m_0\left(\left(-2+\sqrt{1+y^2}\right)\left(5+y^2+2\sqrt{1+y^2}\right)\right). \qquad (28)
\end{aligned}
$$

The factor $1-4y+y^2$ of the denominator of $m(y,m_0)$ and $M(y,m_0)$ is positive when $y \in (0,2-\sqrt{3}) \cup (2+\sqrt{3},\infty)$ and is negative when $y \in (2-\sqrt{3},2+\sqrt{3})$. Therefore to find the sign of $m(y,m_0)$ and $m(y,m_0)$ we need to analyze $N_m(y,m_0)$ and $N_M(y,m_0)$. The component of the numerator of $m(y,m_0)$, $N_m(y,m_0)$, has two factors i.e. $-2+\sqrt{1+y^2}$ and $-2y+\sqrt{1+y^2}$ which can become negative and hence can make $N_m(y,m_0)$ negative. The factor $-2+\sqrt{1+y^2}>0$ when $y\in(\sqrt{3},\infty)$ and $-2y+\sqrt{1+y^2}>0$ when $y\in(0,\frac{1}{\sqrt{3}})$. As both the intervals have empty intersection therefore we must have the following bound on m_0 for $N_m(y,m_0)$ to be positive.

$$
m_0 > \frac{y^3\left(8-\left(1+y^2\right)^{3/2}\right)}{-8y^3+\left(1+y^2\right)^{3/2}}. \qquad (29)
$$

Hence $m(y,m_0)$ will be positive in the following two regions.

$$
\begin{aligned}
R_{1m} &= \{(y,m_0)|m_0 > \frac{y^3\left(8-\left(1+y^2\right)^{3/2}\right)}{-8y^3+\left(1+y^2\right)^{3/2}} \\
&\quad \text{and } \ y\in(0,2-\sqrt{3})\cup(2+\sqrt{3},\infty)\}, \qquad (30)\\
R^*_{1m} &= \{(y,m_0)|m_0 < \frac{y^3\left(8-\left(1+y^2\right)^{3/2}\right)}{-8y^3+\left(1+y^2\right)^{3/2}} \\
&\quad \text{and } \ y\in(2-\sqrt{3},2+\sqrt{3})\}. \qquad (31)
\end{aligned}
$$

Similarly $M(y,m_0)$ is positive in the following two regions

$$
\begin{aligned}
R_{1M} &= \{(y,m_0)|m_0 > \frac{8y^3-\left(1+y^2\right)^{3/2}}{-8+\left(1+y^2\right)^{3/2}} \\
&\quad \text{and } \ y\in(0,2-\sqrt{3})\cup(2+\sqrt{3},\infty)\}, \qquad (32)\\
R^*_{1M} &= \{(y,m_0)|m_0 < \frac{8y^3-\left(1+y^2\right)^{3/2}}{-8+\left(1+y^2\right)^{3/2}} \text{ and } y\in(2-\sqrt{3},2+\sqrt{3})\} \qquad (33)
\end{aligned}
$$

Hence, the central configuration region for this particular set up of the rhomboidal five body problem where both $m(x,y,m_0)$ and $M(x,y,m_0)$ are positive is given by

$$
R_1 = (R_{1m}\cup R^*_{1m})\cap(R_{1M}\cup R^*_{1M}). \qquad (34)
$$

This completes the proof of theorem 2. This central configuration region is given in figure (2)

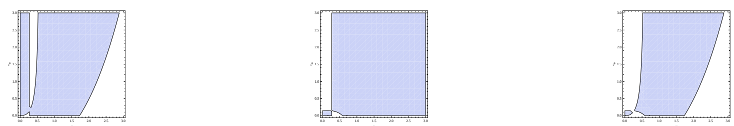

Fig. 2. left: $m(y, m_0) > 0$. **Centre:** $M(y, m_0) > 0$ **Right:** $m(y, m_0) > 0$ and $M(y, m_0) > 0$

4 Proof of Theorem 3.

Let $\lambda = 1$. Solve equations (19 and 20) to obtain m and M as functions of x, y and m_0.

$$m(x, y, m_0) = \frac{4\left(x^2+y^2\right)^{3/2}\left(\begin{array}{c} y^3\left(-8x^3+\left(x^2+y^2\right)^{3/2}\right) \\ +m_0\left(-8y^3+\left(x^2+y^2\right)^{3/2}\right) \end{array}\right)}{\left(x^2-4xy+y^2\right)\left(x^4+4x^3y+18x^2y^2+4xy^3+y^4\right)} \tag{35}$$

$$M(x, y, m_0) = \frac{4\left(x^2+y^2\right)^{3/2}\left(\begin{array}{c} x^3\left(-8y^3+\left(x^2+y^2\right)^{3/2}\right) \\ +m_0\left(-8x^3+\left(x^2+y^2\right)^{3/2}\right) \end{array}\right)}{\left(x^2-4xy+y^2\right)\left(x^4+4x^3y+18x^2y^2+4xy^3+y^4\right)} \tag{36}$$

It can be immediately seen that the denominator of both $m(x, y, m_0)$ and $M(x, y, m_0)$ becomes singular at $y = (2 \pm \sqrt{3})x$. Therefore $y = (2 \pm \sqrt{3})x$ will form two singular curves for the two masses m and M. Therefore the denominator will be positive in region R_d given below and will be negative in its complement.

$$R_d = \{(x, y) | 0 < y < (2 - \sqrt{3})x \text{ or } y > (2 + \sqrt{3})x, x > 0\}. \tag{37}$$

It is not possible to explicitly solve the numerator of either $m(x, y, m_0)$ or $M(x, y, m_0)$ for x or y therefore we choose the inter body distance $x^2 + y^2$ to find regions of central configuration where both m and M are positive. In the numerator of $m(x, y, m_0)$ the factor

$$y^3\left(-8x^3+\left(x^2+y^2\right)^{3/2}\right)+m_0\left(-8y^3+\left(x^2+y^2\right)^{3/2}\right) = N_{3m}$$

can be become negative. By taking $r = \sqrt{x^2+y^2}$, the factor N_{3m} is simplified as below.

$$N_{3m} = y^3\left(-8x^3+r^3\right)+m_0\left(-8y^3+r^3\right) \tag{38}$$

After some algebraic manipulation it can be shown that N_{3m} is positive in the following region.

$$R_{3m} = \{(x,y)|r(x,y) > 2y\sqrt[3]{\frac{m_0+x^3}{m_0+y^3}}, x>0, y>0, m_0>0\}. \tag{39}$$

N_{3m} is negative in the complement of R_{3m}. Therefore, in this particular set up, the central configuration region where m is positive is given by

$$(R_d \cap R_{3m}) \cup (R_d^c \cap R_{3m}^c). \tag{40}$$

Similarly $N_{3M} = x^3\left(-8y^3+\left(x^2+y^2\right)^{3/2}\right)+m_0\left(-8x^3+\left(x^2+y^2\right)^{3/2}\right)$ is positive in the following region.

$$R_{3M} = \{(x,y)|r(x,y) > 2x\sqrt[3]{\frac{m_0+y^3}{m_0+x^3}}, x>0, y>0, m_0>0\}. \tag{41}$$

N_{3M} is negative in the complement of R_{3M}. Therefore, in this particular set up, the central configuration region where M is positive is given by

$$(R_d \cap R_{3M}) \cup (R_d^c \cap R_{3M}^c). \tag{42}$$

Hence, the central configuration region for this particular set up of the rhomboidal five body problem where both $m(x,y,m_0)$ and $M(x,y,m_0)$ are positive is given by

$$R_3 = ((R_d \cap R_{3m}) \cup (R_d^c \cap R_{3m}^c)) \cap (R_d \cap R_{3M}) \cup (R_d^c \cap R_{3M}^c). \tag{43}$$

In the complement of this region no central configurations are possible as at least one of the masses will become negative. This completes the proof of theorem 3.

5 Acknowledgments

The authors, Muhammad Shoaib and Yehia A Abdel-Aziz thank the Deanship of Scientific research at the University of Hail, Saudi Arabia for funding this project (reference number SM3) for the year 1433 Hijri (2012-2013).

References

1.B. Lennard, and S. Simmons. Stability of the Rhomboidal Symmetric-Mass Orbit.*arXiv preprint arXiv:1208.3183* (2012).

2.D. Diarova and N. I. Zemtsova. The instability of the rhombus-like central configurations in newton 9-body problem. *Computer Algebra in Scientific Computing.* Springer Berlin Heidelberg, 2006.

3.L. F. Mello and A. C. Fernandes. Co-circular and co-spherical kite central configurations. *Qualitative theory of dynamical systems.* 10 (2011) 29-41.

4.M. Kulesza, M. Marchesin, and C. Vidal. Restricted rhomboidal five-body problem. *Journal of Physica A: Mathematical and Theoritical.* 44 (2011) 485204.

5.M. Marcelo, and C. Vidal. Spatial restricted rhomboidal five-body problem and horizontal stability of its periodic solutions. *Celestial Mechanics and Dynamical Astronomy* (2013): 1-19.

6.M. Shoaib, B.A. Steves, and A. Széll. Stability analysis of quintuple stellar and planetary systems using a symmetric five-body model. *New Astronomy.* 13 (2008) 639-645.

7.M. Shoaib and I. Faye. Collinear equilibrium solutions of four-body problem. *Journal of Astrophysics and Astronomy.* 32 (2011) 411-423.

8.T Ouyang and Z. Xie. Collinear central configuration in four-body problem, *Celestial Mechanics and Dynamical Astronomy.* 93 (2005) 147-166.

Chaotic Modeling and Simulation (CMSIM) 3: 441–450, 2013

An efficient computational approach for global regularisation schemes

Anoop Sivasankaran[1] and Muhammad Shoaib[2]

[1] Khalifa university of Sciences Technology and Research, Department of Applied Mathematics and Sciences, PO Box 573, Sharjah UAE
(E-mail: Anoop.Sivasankaran@kustar.ac.ae)
[2] University of Hail, Department of Mathematic, PO BoX 2440, Hail Saudi Arabia.
(E-mail: safridi@gmail.com)

Abstract. Due to collisional singularities appearing in gravitational few-body problems, one needs regularisation techniques for their stable approximate solution. We present an efficient computational approach for numerically integrating a symmetrical five body problem called the Caledonian Symmetric Five Body Problem (CS5BP) which is a five-body system with a symmetrically reduced phase space. The proposed global regularisation scheme consists of adapted versions of several known regularisation transformations such as the Levi-Civita-type coordinate transformations together with a time transformation which enables the numerical exploration of the systems as they pass through two-body close encounters. An algebraic optimisation algorithm is adapted for numerically implementing the regularisation scheme which make use of the reverse mode algorithmic differentiation. We show that the proposed regularisation algorithm is numerically and computationally very efficient in handling various two-body close encounters appearing in the CS5BP.
Keywords: Regularisation, singularity, celestial mechanics, few-body problem, optimisation.

1 Introduction

There is a growing interest in studying gravitational few-body problems (with $n > 3$) which makes use of the symmetric boundary conditions to reduce the mathematical complexity of the problem [13],[14], [8], [7].

Several papers in the last decade have studied the the Caledonian Symmetric Four-Body Problem (CSFBP) which is a restricted coplanar four-body system with a symmetrically reduced phase space [5], [12]. The model involves two pairs of non-equal masses moving in coplanar, initially circular orbits, starting in a collinear arrangement [5]. The authors have shown that the global stability of the CSFBP system depends on a parameter called the Szebehely constant C_0. The Szebehely constant $C_0 = -\frac{c^2 E}{G^2 M^5}$ is a dimensionless function of the total energy (E) and the magnitude of the angular momentum of the system

Received: 16 April 2013 / Accepted: 18 July 2013

ISSN 2241-0503

(c), where G is the gravitational constant, and M is the total mass. A generalization of the CSFBP named the Caledonian Symmetric Five-Body problem (CS5BP) was done by introducing a stationary mass to the centre of mass of the CSFBP with the same analytical stability criteria [8].

Existing numerical integration schemes were inadequate to study orbits with strong close encounters, as the numerical integration fails due to collision singularities [15], [16]. In gravitational few-body problems, singularities normally appear when the distance between objects undergoing orbital motion becomes very small. As a result, the equations describing the dynamics of the system tend towards singular and the numerical integration falls apart [3]. Use of regularisation algorithms to numerically integrate gravitational few-body problems which involve near collisions or close encounters has been widely acknowledged [3], [1]. Recently a global regularisation scheme for the CSFBP is prsented in [11]. In this paper, we extend the regularisation scheme to the Caledonian Symmetric Five-Body problem (CS5BP).

2 Definition of the Caledonian Symmetric Five Body Problem(CS5BP)

Let us consider five bodies P_0,P_1,P_2,P_3,P_4 of masses m_0,m_1, m_2,m_3,m_4 respectively existing in three dimensional Euclidean space [6]. The radius and velocity vectors of the bodies with respect to the centre of mass of the five body system are given by $\mathbf{r}_i$ and $\dot{\mathbf{r}}_i$ respectively, $i = 0, 1, 2, 3, 4$. Let the centre of mass of the system be denoted by O.

The CS5BP involves two types of symmetries; past-future symmetry and dynamical symmetry [8]. Past future symmetry exists in an n-body system when the dynamical evolution of the system after $t = 0$ is a mirror image of the dynamical evolution of the system before $t = 0$. It occurs whenever the system passes through a mirror configuration, *i.e.* a configuration in which the velocity vectors of all the bodies are perpendicular to all the position vectors from the centre of mass of the system [5].

Dynamical symmetry exists when the dynamical evolution of two bodies on one side of the centre of mass of the system is paralleled by the dynamical evolution of the two bodies on the other side of the centre of mass of the system. The resulting configuration is always a parallelogram, but of varying length, width and orientation [8]. See Figure 1 for the configuration of the CS5BP for $t > 0$.

The CS5BP has the following conditions:

1. All five bodies are finite point masses with:

$$m_1 = m_3, \qquad m_2 = m_4 \tag{1}$$

2. P_0 is stationary at origin O, the centre of mass of the system. P_1 and P_3 are moving symmetrically to each other with respect to the centre of mass of the system. Likewise P_2 and P_4 are moving symmetrically to each other. Thus dynamical symmetry is maintained for all time t;

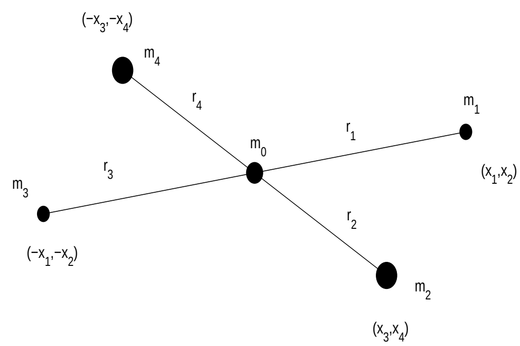

Fig. 1. The configuration of the coplanar CS5BP for $t > 0$

$$\mathbf{r}_1 = -\mathbf{r}_3, \qquad \mathbf{r}_2 = -\mathbf{r}_4, \qquad \mathbf{r}_0 = 0,$$
$$\mathbf{V}_1 = \dot{\mathbf{r}}_1 = -\dot{\mathbf{r}}_3, \qquad \mathbf{V}_2 = \dot{\mathbf{r}}_2 = -\dot{\mathbf{r}}_4, \qquad \mathbf{V}_0 = \dot{\mathbf{r}}_0 = 0. \tag{2}$$

3. At time $t = 0$ the bodies are collinear with their velocity vectors perpendicular to their line of position. This ensures the past-future symmetry and is described by:

$$\mathbf{r}_1 \times \mathbf{r}_2 = 0, \qquad \mathbf{r}_1 \cdot \dot{\mathbf{r}}_1 = 0, \qquad \mathbf{r}_2 \cdot \dot{\mathbf{r}}_2 = 0. \tag{3}$$

We define the masses as ratios to the total mass. Let the total mass M of the system be

$$M = 2\,(m_1 + m_2) + m_0 \tag{4}$$

Let μ_i be the mass ratios defined as $\mu_i = \frac{m_i}{M}$ for $i = 0, 1, 2, 3, 4$ and $\mu = \frac{\mu_1}{\mu_2}$. Equation (4) then becomes

$$2\,(\mu_1 + \mu_2) + \mu_0 = 1, \tag{5}$$

and

$$0 \leq \mu_0 \leq 1, 0 \leq \mu_1 \leq 0.5, 0 \leq \mu_2 \leq 0.5. \tag{6}$$

3 The regularisation scheme

The proposed regularisation scheme consists of a combination of several known regularisation techniques: a Levi-Civita type coordinate transformation, a time transformation function similar to that of [1] and the global formulation of [3]. In general, the proposed scheme follows the transformations described in [4]. We extend the regularisation procedure of the CSFBP [11] into the case of the CS5BP.

Let the position coordinates of the four bodies in cartesian coordinates be $\mathbf{r}_1 = (x_1, x_2)$, $\mathbf{r}_2 = (x_3, x_4)$, $\mathbf{r}_3 = (-x_1, -x_2)$, $\mathbf{r}_4 = (-x_3, -x_4)$, with corresponding momenta $(\omega_1, \omega_2) = \mu_1 M(\dot{x_1}, \dot{x_2})$, $(\omega_3, \omega_4) = \mu_2 M(\dot{x_3}, \dot{x_4})$, $(-\omega_1, -\omega_2)$, $(-\omega_3, -\omega_4)$.

For simplicity, we set the gravitational constant G and total mass M to be equal to unity. According to the symmetrical restrictions, the Hamiltonian function can be written as

$$\begin{aligned} H = {} & \frac{1}{\mu_1 M}(\omega_1^2 + \omega_2^2) + \frac{1}{\mu_2 M}(\omega_3^2 + \omega_4^2) - 2G\mu_1\mu_2 M^2\left(\frac{1}{r_{12}} + \frac{1}{r_{14}}\right) \\ & - \frac{G\mu_1^2 M^2}{r_{13}} - \frac{G\mu_2^2 M^2}{r_{24}} - 4G\mu_0 M\left(\frac{\mu_1 M}{2r_{13}} + \frac{\mu_2 M}{2r_{24}}\right), \end{aligned} \tag{7}$$

where the corresponding inter-body distances are given by

$$\begin{aligned} r_{12} &= \left((x_1 - x_3)^2 + (x_2 - x_4)^2\right)^{1/2} = r_{34}, \\ r_{14} &= \left((x_1 + x_3)^2 + (x_2 + x_4)^2\right)^{1/2} = r_{23}, \\ r_{13} &= \left((2x_1)^2 + (2x_2)^2\right)^{1/2}, \\ r_{24} &= \left((2x_3)^2 + (2x_4)^2\right)^{1/2}. \end{aligned} \tag{8}$$

These four inter-body distances result in collision singularities which is characterised by the following four types of two-body close encounters [10].

1. "12"-type double binary collision: collisions occurring in the binary formed between P_1 and P_2 and the symmetrical binary formed between P_3 and P_4.
2. "14"-type double binary collision: collisions occurring in the binary formed between P_1 and P_4 and the symmetrical binary formed between P_2 and P_3.
3. "13"-type single binary collision: collision occurring in the binary formed between P_1 and P_3.
4. "24"-type single binary collision: collision occurring in the binary formed between P_2 and P_4.

Note that P_0 is stationary at O, the centre of mass of the system and thus P_0 has no influence in deciding the kinetic energy of the system and the collisions.

In order to regularise these singularities first we will map the (x_i, ω_i) physical plane into the (Q_i, P_i) parametric plane using a series of transformation equations so that the new Hamiltonian function will have no singularities as it passes through a two-body close encounter. There are three important steps in the regularisation scheme [9].

Step 1: Coordinate transformation
We first transform the coordinate system to inter-body coordinates.

$$q_1 = x_1 - x_3, \qquad q_2 = x_2 - x_4, \tag{9}$$

$$q_3 = x_3 + x_1, \qquad q_4 = x_4 + x_2, \tag{10}$$

$$q_5 = 2x_1, \qquad q_6 = 2x_2, \tag{11}$$

$$q_7 = 2x_3, \qquad q_8 = 2x_4. \tag{12}$$

This will make sure that all the possible two-body close encounters in the CS5BP system are regularised [11].

We introduce a generating function $F_1(p_k, q_k)$ to obtain conjugate momenta p_k of the corresponding q_k

$$F_1(p_k, q_k) = p_k q_k = (x_1 - x_3)p_1 + (x_2 - x_4)p_2 + (x_3 + x_1)p_3 + (x_4 + x_2)p_4 \\ + 2x_1 p_5 + 2x_2 p_6 + 2x_3 p_7 + 2x_4 p_8, \quad (13)$$

which will give

$$\omega_i = \frac{\partial F_1}{\partial x_i}, \quad (14)$$

where i=1 to 4 and k=1 to 8.

Next we find an expression for new momenta, p_k's, in terms of old momenta, ω_i, using an arbitrary relation which is similar to that for the q' s (i.e. $q_5 - q_7 - 2q_1 = 0, q_5 + q_7 - 2q_3 = 0, q_6 + q_8 - 2q_4 = 0, q_6 - q_8 - 2q_2 = 0$), we set

$$\begin{aligned} p_5 - p_7 - 2p_1 &= 0, \\ p_5 + p_7 - 2p_3 &= 0, \\ p_6 + p_8 - 2p_4 &= 0, \\ p_6 - p_8 - 2p_2 &= 0. \end{aligned} \quad (15)$$

Using equation (14) and (15), we can deduce a set of new conjugate momenta p's as

$$\begin{aligned} &p_1 = \frac{1}{6}\left(\omega_1 - \omega_3\right), \qquad p_2 = \frac{1}{6}\left(\omega_2 - \omega_4\right), \\ &p_3 = \frac{1}{6}\left(\omega_1 + \omega_3\right), \qquad p_4 = \frac{1}{6}\left(\omega_2 + \omega_4\right), \\ &p_5 = \frac{1}{3}\omega_1, \qquad p_6 = \frac{1}{3}\omega_2, \\ &p_7 = \frac{1}{3}\omega_3, \qquad p_8 = \frac{1}{3}\omega_4. \end{aligned} \quad (16)$$

Now we perform the Levi-Civita type coordinate transformation on each inter-body coordinate. We introduce the regularising function using the Levi-Civita transformation, in a complex form

$$q_j + iq_{j+1} = \left(Q_j + iQ_{j+1}\right)^2, \quad (17)$$

where j= 1,3,5,7. Here note that (q_j, q_{j+1}) refers to a physical plane and (Q_j, Q_{j+1}) refers to a parametric plane. Their corresponding conjugate momenta P_k's are given by

$$P_k = \frac{\partial F_2(p_k, Q_k)}{\partial Q_k} \quad (18)$$

where k= 1 to 8 and $F_2(p_k, Q_k)$ is the generating function of the form

$$F_2(p_k, Q_k) = p_j f(Q_j, Q_{j+1}) + p_{j+1} g(Q_j, Q_{j+1})$$

Using these relations, we can write

$$\begin{aligned} P_j &= 2p_jQ_j + 2p_{j+1}Q_{j+1}, \\ P_{j+1} &= -2p_jQ_{j+1} + 2p_{j+1}Q_j, \end{aligned} \tag{19}$$

Step 2: Time transformation
In the next step, we introduce a fictitious time τ, which is a key factor for the regularising effect. The basic principle of regularisation theory is to transform physical coordinates to a parametric plane and physical time to an artificial time by a differential time transformation, which consequently smooths collision effects in the Hamiltonian system. In the literature, we can find a variety of choices for the time transformation function which has a general form

$$dt = g d\tau = R^n d\tau,$$

where R is the separation between the colliding binaries, g is the time re-scaling factor and n has various choices according to the application. We had tried a few arbitrary values for g and we found that, to preserve conservation of energy, it is advantageous to choose a time re-scaling factor of the form

$$\begin{aligned} \frac{dt}{d\tau} = g &= \frac{r_{12}r_{13}r_{14}r_{24}}{(r_{12}+r_{13}+r_{14}+r_{24})^{5/2}} \\ &= \frac{(Q_1^2+Q_2^2)(Q_3^2+Q_4^2)(Q_5^2+Q_6^2)(Q_7^2+Q_8^2)}{(Q_1^2+Q_2^2+Q_3^2+Q_4^2+Q_5^2+Q_6^2+Q_7^2+Q_8^2)^{5/2}}. \end{aligned} \tag{20}$$

Step 3: Fixing the energy
With the introduction of the time rescaling factor, the new Hamiltonian $\tilde{H}(Q_i, P_i)$ takes the following form in the extended phase space

$$\Gamma(Q_i, P_i) = g(\tilde{H} - h_0), \tag{21}$$

where Γ is the transformed Hamiltonian $\tilde{H}(Q_i, P_i)$ in the extended phase space and h_0 is the total energy or the initial value of $\tilde{H}$. For any particular orbit, $\tilde{H}(\tau) = h_0$, a constant and $\Gamma(\tau) = 0$. We have not shown the transformed Hamiltonian $\Gamma(Q_i, P_i)$ in this paper, as the right hand side of the expression is very lengthy due to a large number of multiplicative terms. The numerator terms in the time rescaling factor g cancel out the singular terms in the denominator of the Hamiltonian function and prevent the increase of the velocity to infinity at the collision stages.

We can derive the Hamilton equations of motion with respect to the fictitious time, using this transformed Hamiltonian in the new set of parametric coordinates:

$$\begin{aligned} \frac{dQ_i}{d\tau} &= \frac{\partial \Gamma}{\partial P_i}, \\ \frac{dP_i}{d\tau} &= -\frac{\partial \Gamma}{\partial Q_i}. \end{aligned} \tag{22}$$

Equation (22) is the final regularised equation of motion, which is a set of ordinary differential equations whose solution is a function of the fictitious time τ and these equations are regular, for any $q_i \to 0$.

There can be singularities when all $q_i \to 0$, where i= 1 to 8. This situation is only possible for a CS5BP system with $C_0 = 0$. This corresponds to a singularity at the origin in the physical plane. For $C_0 \neq 0$; regions of forbidden motion appear very close to the origin and a total central collision is not theoretically possible.

4 Optimisation of the regularised Hamiltonian

An optimisation strategy is not generally required for restricted few-body problems for $n < 4$, since the equations of motion derived using standard regularisation schemes usually contain algebraic terms which can be easily handled by most of the standard numerical integrators. However, the transformed Hamiltonian $\Gamma(Q_i, P_i)$ in Equation (21) is determined using a large number of algebraic multiplications. It is evident that the symbolic differentiation to derive the gradient of $\Gamma(Q_i, P_i)$ will produce a large number of additive and multiplicative terms, leading to an inefficient evaluation of the right hand side of the Equation (22). The direct numerical integration of the regularised Equation (22) (i.e. without using any optimisation techniques) required an excessive amount of computational time even for a very small time period of 10 due to the large number function evaluations involved.

We adapt an algebraic optimisation algorithm of [2] to simplify the Equation 22. The first step in the optimisation process is to rewrite the regularised Hamiltonian $\Gamma(Q_i, P_i)$ in terms of the most frequently appearing terms as a MAPLE procedure [9]. Then we split up the product terms in the MAPLE procedure in calculating the regularised Hamiltonian to avoid the generation of common subexpressions while computing its partial derivatives [2].

We also make use of the reverse-mode algorithmic differentiation to reduce the total number of multiplicative operations (multiplication and addition) to derive the partial derivatives of the regularised Hamiltonian $\Gamma(Q_i, P_i)$. The reverse-mode of automatic differentiation allows computation of gradients at a small cost of computing functions by decomposing the function into a sequence of elementary assignments. The forward-mode differentiation of $\Gamma(Q_i, P_i)$ will generate more than 2100 multiplicative terms, whereas the reverse mode algorithmic differentiation leads to a procedure with only about 320 multiplications. Then we convert repeating symbolic expressions into computation sequences needed for the algorithmic differentiation using the built-in MAPLE functions. In general, this algebraic optimisation procedure can be extended to majority of the global regularisation schemes used in gravitational few-body problems (with $n \geq 3$) and fast numerical realization can be achieved.

5 Numerical experiments

We show some preliminary numerical results using the non-regularised and regularised integration schemes for a regular quasi-periodic orbit. The initial conditions for integrating equation (20) and (22) were fixed using the energy and angular momentum equations of the CS5BP. Numerical experiments were

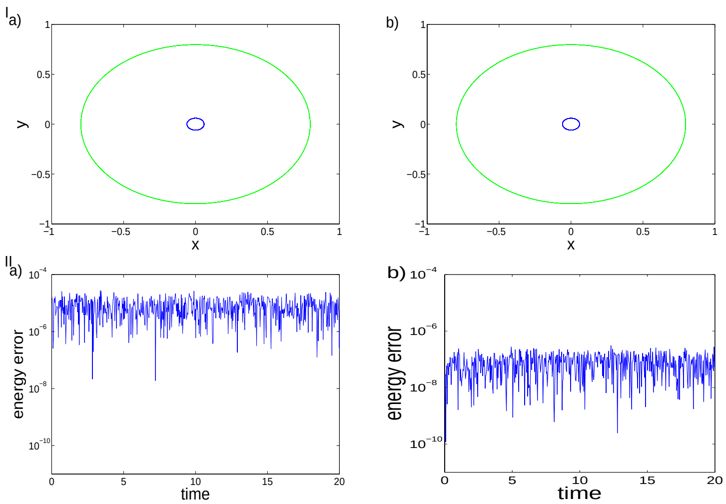

Fig. 2. A quasi-periodic orbit over the time $[0, 20]$ ($\mu = 1$, $\mu_0 = 0$, $E = -7$, $C_0 = 60$ initial $\mathbf{r}_1 = 0.80$ and $\mathbf{r}_2 = 0.06$); with a) non-regularised; b) regularised equations. I. Trajectories of P_1(green) and P_2 (blue) in the xy-plane of motion; II. Energy error over the time period $[0, 20]$

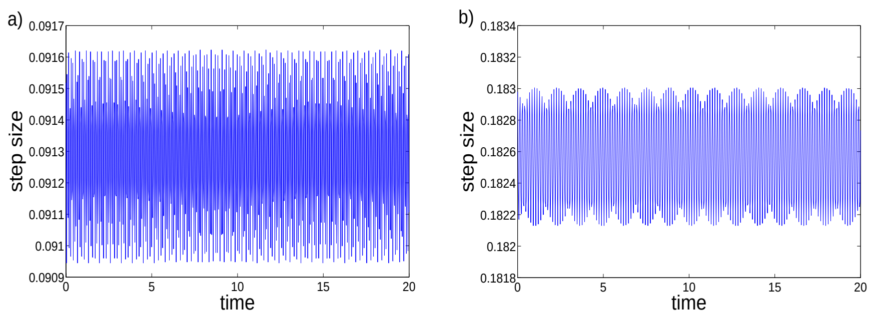

Fig. 3. Time step variations over the time $[0, 20]$ with a) non-regularised; b) regularised equations.

conducted using the standard MATLAB multi-step integrator ode113 which is a variable order Adams-Bashforth-Moulton PECE solver. The orbital trajectories in the xy-plane of motion are shown in Figure 2.1.A central binary is formed (with P_2 and P_4) and the other symmetrical pair P_1 and P_3 orbit around the binary's centre of mass. Only the positions of masses m_1 (x_1, x_2) (green) and m_2 (x_3, x_4)(blue) are shown. The orbits are well separated and remained bounded for some reasonable amount of integration time.

Figure 2.II shows the numerical energy error versus time over a 20 time unit period. Although the orbital trajectories appear to be identical, the regularised integration scheme exhibits a better energy error profile by a factor of 100. Figure 3 shows the corresponding time step variations for the above integrations. The regularised integration scheme has improved the CPU workload

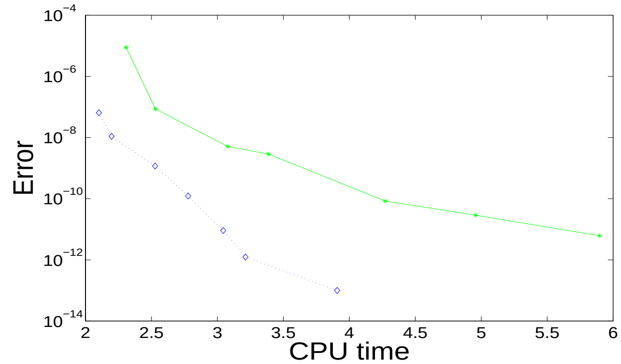

[h]

Fig. 4. Comparisons of the errors with variable absolute tolerance error and relative tolerance error; green (non-regularised) and blue (regularised).

by a factor of 1.4 by allowing the integrator to choose bigger step-sizes resulting in decreased number of time steps. Figure 4 shows a comparison between the CPU time and the maximum observed energy error for the given simulation time. It is clear that the regularised scheme allows better accuracy with improved CPU run time. Despite the regularity of the orbit and the absence of extreme close encounters, our numerical tests indicate that the overall CPU workload has been improved. The computational cost involved in each time step differs for both the non-regularised and regularised integrations, since the regularised scheme has twice as many equations in the non-regularised scheme and it involved a large number of algebraic multiplications and additions due to several coordinate transformations forward and backwards. The regularised treatment combined with the algebraic optimisation scheme outperforms the non-regularised approach in terms of computational efficiency and numerical accuracy.

6 Conclusions

We developed a global regularisation scheme that consists of adapted versions of several known regularisation transformations such as the Levi-Civita-type coordinate transformations; that together with a time transformation, removes all the singularities due to colliding pairs of masses in the CS5BP. An algebraic optimisation algorithm is proposed for numerically implementing the regularisation scheme. Regardless of the nature of the orbits, it was found that the regularised integration scheme outperformed the standard non-regularised integration schemes in terms of computational performance and improved numerical accuracy characterized by stable energy profiles.

7 Acknowledgement

The authors are grateful to Prof. Bonnie Steves (Glasgow Caledonian University, Scotland) and Dr Winston Sweatman (Massey University, New Zealand) for many enlightening discussions that motivated our work. The basic outline of the regularisation algorithm was generously provided by Dr Winston Sweatman.

References

1. S. J. Aarseth and K. Zare. A regularisation of the three body problem. *Celestial Mechanics* 10:185-205, 1974.
2. D. Gruntz and J. Waldvogel. Orbits in the Planar Three-Body Problem, In W. Gander and J. Hrebicek (eds) *Solving Problems in Scientific Computing Using Maple and Matlab*, pp 51-72, 1997.
3. D. C. Heggie. A Global Regularisation of the Gravitational N-Body Problem. *Celestial Mechanics* 10:217-241, 1974.
4. D. C. Heggie and W. L. Sweatman. Three-body scattering near triple collision or expansion. *Monthly Notices of Royal Astronomical Society* 250:555-575, 1991.
5. A. E. Roy and B. A. Steves . The Caledonian Symmetrical Double Binary Four-Body Problem: Surfaces of zero velocity using the energy integral. *Celestial Mechanics and Dynamical Astronomy* 78:299-318, 2000.
6. M. Shoaib. Many Body Symmetrical Dynamical Systems. *Glasgow Caledonian University*, 2004.
7. M. Shoaib and I. Faye. Collinear equilibrium solutions of four-body problem. *Journal of Astrophysics and Astronomy*. 32:411-423, 2011.
8. M. Shoaib, B. A. Steves and A. Széll. Stability analysis of quintuple stellar and planetary systems using a symmetric five-body model. *New Astronomy* 13:639-645, 2008.
9. A. Sivasankaran. Stability of the Caledonian Symmetric Four-Body Problem with close encounters. *Glasgow Caledonian University*, 2010.
10. A. Sivasankaran and B. A. Steves and W. L. Sweatman. Close encounters in the the Caledonian Symmetric Four-Body Problem. In H. Varvoglis and S. Ferraz-Mello (eds). *Proceedings of the International Conference on the Dynamics of Celestial Bodies*, Publication of Astronomical Observatory of Belgrade pp 57-61, 2009.
11. A. Sivasankaran and B. A. Steves and W. L. Sweatman. A global regularisation for integrating the Caledonian Symmetric Four-Body Problem. *Celestial Mechanics and Dynamical Astronomy* 107:157-168, 2010.
12. B. A. Steves and A. E. Roy. Surfaces of separation in the Caledonian Symmetrical Double Binary Four-Body Problem, In B. A. Steves and A. J. Maciejewski (eds) *The Restless Universe: Application of Gravitational N-Body Dynamics to Planetary, Stellar and Galactic systems*, IOP Publishing, pp 301-325, 2001.
13. W. L. Sweatman. The symmetrical one-dimensional Newtonian four-body problem: A numerical investigation. *Celestial Mechanics and Dynamical Astronomy* 82:179-201, 2002.
14. W. L. Sweatman. A family of Schubart-like interplay orbits and their stability in the one-dimensional four-body problem. *Celestial Mechanics and Dynamical Astronomy* 94:37-65, 2006.
15. A. Széll and B. A. Steves and B. Érdi. The hierarchical stability of quadruple stellar and planetary systems using the Caledonian Symmetric Four-Body Problem. *Astronomy and Astrophysics*, 427:1145-1154, 2004.
16. A. Széll and B. Érdi and Z. Sándor and B. Steves. Chaotic and stable behavior in the Caledonian Symmetric Four-Body Problem. *Monthly Notices of Royal Astronomical Society*, 347:380-388, 2004.

Chaotic Modeling and Simulation (CMSIM) 3 : 451-461, 2013

Pattern Formation Dynamics in Diverse Physico-Chemical Systems

Tony Karam, Houssam El-Rassy, Victor Nasreddine, Farah Zaknoun, Samia El-Joubeily, Amal Zein Eddin, Hiba Farah, Jad Husami, Samih Isber† and Rabih Sultan*

Departments of Chemistry and †Physics, American University of Beirut, Beirut, Lebanon
E-mail: rsultan@aub.edu.lb

Abstract: Complex reaction-transport dynamics can lead to the formation of ordered structures. A constant dissipation of free energy is a requirement for sustaining macroscopic order, especially in solution. In the solid phase, the evolved pattern can be locked for days, months or even years. Liesegang bands are stratified stripes of precipitate that appear and persist, when co-precipitate ions interdiffuse in a gel medium. A host of interesting properties characterize such rich dynamical systems: band spacing laws (direct and revert), band splitting, rhythmic multiplicity, multiple precipitate formation and band redissolution are but a few manifested characteristics, emerging from a complex dynamics with a great diversity of scenarios.
The familiar and well-known band formation in rocks could be the result of a complex coupled diffusion-percolation-chemical reaction mechanism. Similarities between geochemical self-organization and the Liesegang phenomenon are surveyed and analyzed. The simulation of band generation in a rock bed is realized and carried out in-situ, by injection and infusion of the reactant components into the rock medium.
Ramified, tree-like structures (dendrites) are obtained during the electrodeposition or simple electroless redox deposition of metal systems. A great variety of morphologies just resembling tree branches are observed and characterized as fractal structures.
Keywords: Liesegang, dendrites, reaction-diffusion, rock banding.

1. Liesegang Banding

In 1896, Raphael Eduard Liesegang discovered an intriguing phenomenon [1] whereby precipitation in a gel medium takes place in banded form, just like the superb display of bands that we commonly observe in rocks [2-4]. Various specimens of Liesegang patterns, prepared for different precipitates, are shown in Fig. 1.

Received: 12 April 2013 / Accepted: 20 July 2013

ISSN 2241-0503

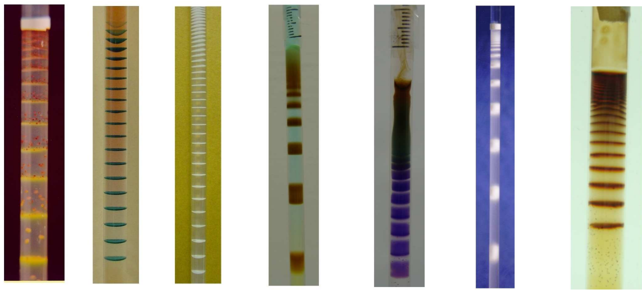

Figure 1: A panorama of colorful Liesegang patterns in gel.

In the laboratory, the Liesegang experiment [5-7] is quite simple: a concentrated electrolyte containing a certain co-precipitate ion (say Pb^{2+}) is allowed to diffuse into a gel containing its insoluble salt counterpart (such as I^- to form PbI_2); normally one order of magnitude more dilute. Due to the coupling of diffusion to a cycle of supersaturation, nucleation and depletion, known as the Ostwald cycle [8], the precipitation takes place in the form of beautifully stratified bands, as displayed in Fig. 1.

We highlight the main features of such a rich dynamical phenomenon, but also shed light on abnormalities, curiosities and strange behavior exhibited by such systems under certain conditions. The observations common to most Liesegang systems are summarized by the four well-known empirical laws [9,10]:

Time law: $x_n = \sqrt{at_n}$	*Spacing law:* $\rho_n = \dfrac{x_{n+1}}{x_n} \to 1+p$ as as n is large.
Width law: $w_n = mx_n^{\alpha} \quad \alpha > 0$	*Matalon-Packter law:* $p = F(b_0) + \dfrac{G(b_0)}{a_0}; \begin{cases} a_0 \text{ conc. of outer} \\ b_0 \text{ conc. of inner} \end{cases}$

where n denotes band number, x is location and w is band width. The spacing law formula suggests that the spacing between consecutive bands increases as we move away from the electrolytes junction. Although 90% of the Liesegang patterns follow this so-called Jablczynski spacing law [11], some systems exhibit an opposite trend, known as *revert* spacing [12,13]. The distinction between *direct* and *revert* spacing Liesegang patterns is depicted in Fig. 2.

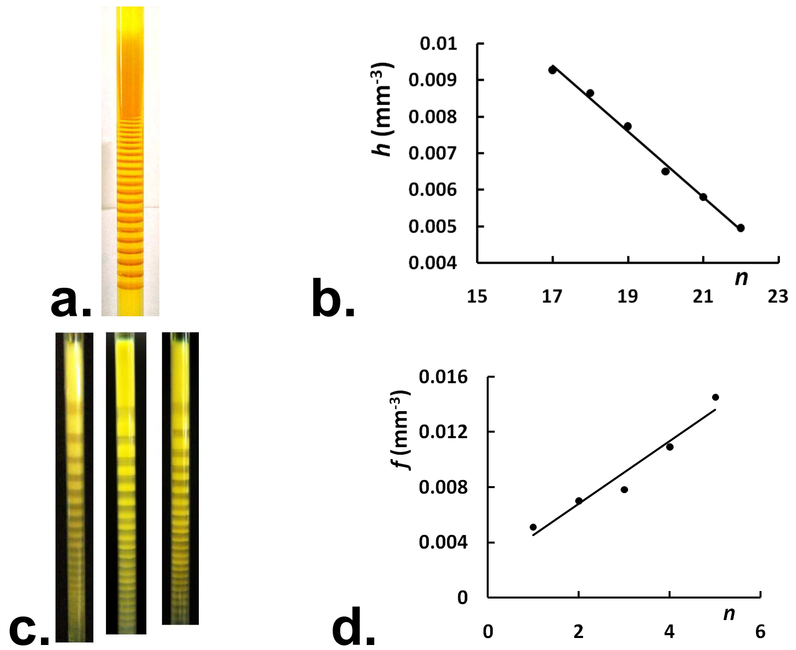

Figure 2: a. Liesegang pattern of $CuCrO_4$ showing direct (normal) spacing. b. Plot of fraction of adsorbed CrO_4^{2-} on the copper chromate precipitate (h) with band number. c. Liesegang patterns of $PbCrO_4$ showing *revert* spacing. d. Plot of fraction of adsorbed CrO_4^{2-} on the lead chromate precipitate (f) with band number. We see that h decreases while f increases.

In a recent study [13], we showed that the fraction of CrO_4^{2-} adsorbed (f) on the lead chromate precipitate increases with band number n (see Fig. 2d); whereas the opposite trend was observed for the adsorption on copper chromate (the fraction h decreases with band number n; as seen in Fig. 2b). Hence the increased extent of adsorption causes the bands to form closer and closer as n increases. It seems that more CrO_4^{2-} adsorbed attract the Pb^{2+} in the gel closer than in the preceding band, thus causing the precipitate band to from closer, and the spacing to become narrower. The opposite behavior (decreasing extent of adsorption with band number as in Fig. 2b) results in a normal Liesegang pattern with direct spacing (Figure 2a).

Liesegang systems exhibit a great diversity of special features. A pattern of bands seemingly 'migrates' if redissolution of the bands at the top is synchronized with the band formation. Such scenario occurs in systems where the precipitate redissolves to form a complex ion. Typical studied examples include the $Co(OH)_2$ [14,15], $Cr(OH)_3$ [16] and HgI_2 [17] systems. When $Co(OH)_2$ is precipitated from Co^{2+} and NH_4OH, the precipitate redissolves in excess NH_4OH to form the hexaammine cobalt (II) complex ion, $Co(NH_3)_6^{2+}$, according to the reaction:

$$Co(OH)_2\,(s) + 6\,NH_4^+\,(aq) \longrightarrow Co(NH_3)_6^{2+}\,(aq) + 4\,H^+\,(aq) + 2\,H_2O$$

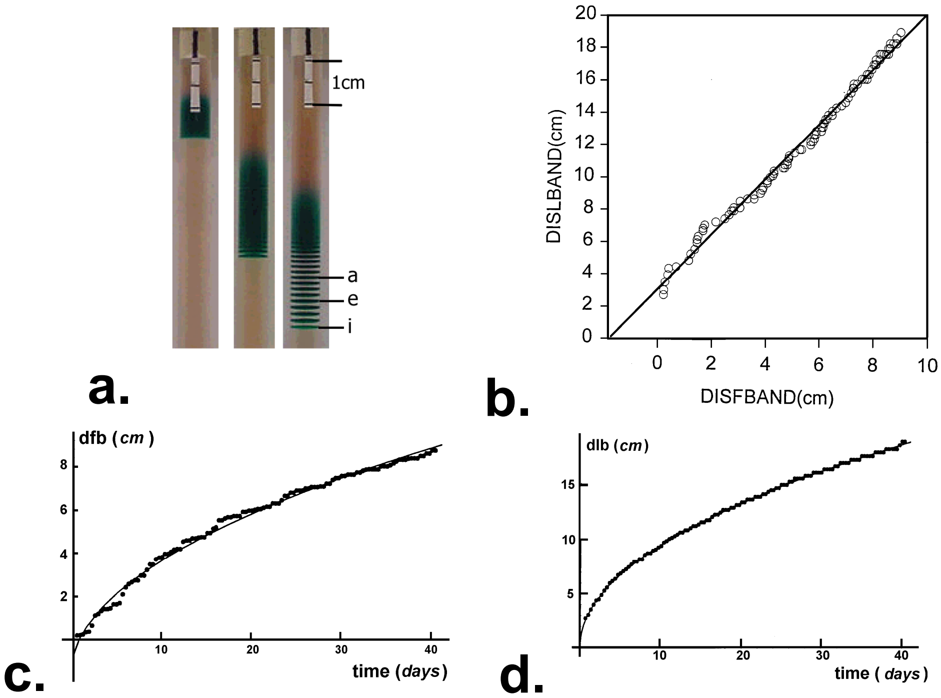

Figure 3: a. Propagating $Co(OH)_2$ Liesegang pattern via a concerted band formation and band redissolution scenario. b. Correlation plot showing the linear correlation between the distance of last band (*dlb*) and distance of first band (*dfb*). c. Plot of *dfb* versus time. d. Plot of *dlb* versus time. The two parameters are controlled by diffusion.

The precipitation-redissolution-propagation of the $Co(OH)_2$ pattern of bands is illustrated in Fig. 3a. The distance of the top edge of the propagation zone (*dfb*) and the distance of the last band (*dlb*) are plotted versus time in days. The plots are shown in Figs. 3c and 3d. We see that the propagation at the top and the bottom is dominated by diffusion. The correlation between *dfb* and *dlb* is almost perfectly linear [14], as revealed by the correlation plot in Fig. 3b.

A host of other diverse features are observed in Liesegang systems. To name but a few, we report secondary banding [18], spiral and helicoidal patterns [19] and two-precipitate dynamics [20].

2. Geochemical Banding

Perhaps the most common and most spread resemblance between Liesegang patterns and natural phenomena is the landscape of bands that we observe in rocks [21,2,3]. Many studies have emphasized such similarity, presented coherent explanations and proposed mechanisms. Theoretical modeling studies are extensive in the literature [21]. Possible scenarios range from cyclicity in large mafic-ultramafic layered intrusions, to fractional crystallization in magmatic processes, to temperature-pressure changes in both first and second-order phase transitions, to nonlinear reaction-diffusion dynamics.

In a recent work, we attempted to simulate geochemical banding (or self-organization) in-situ, i.e. inside the rock bed [22,23].

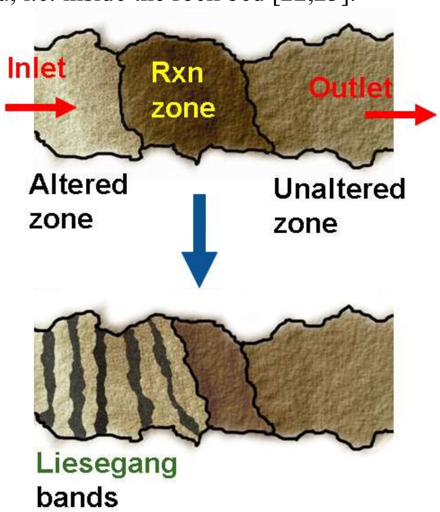

Figure 4: Liesegang bands in a rock bed behind a reaction front. The infiltrating water carries a co-precipitate ion that meets its counter ion in the rock medium and thus precipitation takes place; but it does so but in banded form, just resembling a Liesegang pattern.

Consider a porous rock infiltrated from one side by an inlet flow of reactive water, that causes the dissolution of certain constituent rock minerals. The water flow, acting as a sink of co-precipitate ions for the altered rock, can provoke the precipitation and deposition of other insoluble minerals. In many such situations, the minerals deposition occurs in banded form, in a way that just resembles the Liesegang bands obtained in a lab experiment. Such a plausible scenario is illustrated in Fig. 4.

In the lab, a ferruginous limestone rock with a planar surface (Figure 5) was infiltrated through a thin tube inserted at its center by a 4.30 M H_2SO_4 solution by means of a multi-rate infusion pump. The acid causes the dissolution of calcite ($CaCO_3$) and the precipitation of the acid-insoluble gypsum ($CaSO_4$) and anhydrite ($CaSO_4.2H_2O$) according to the reaction:

$$CaCO_3 + H_2SO_4\ (aq) \longrightarrow CaSO_4 + CO_2 + H_2O$$

Due to the spatio-temporal flow, the deposition of $CaSO_4$ is anticipated to occur in banded form in accordance with the above described Liesegang dynamics (Sect. 1).
The experiment was kept running for about two years (692 days). The appearance of the various banded zones at t = 202 days is depicted in Fig. 5a. The latter were delineated and labeled by tracing contours defining the inner and outer edges of each zone (Figure 5b at 692 days). The gypsum/anhydrite content of regions 1 through 7 of Fig. 5b was determined by powder X-ray diffraction. The results are shown in Table 1.

Table 1: $CaSO_4$ composition over the various zones of Fig. 5

Region	1	2	3	4	5	6	7
% $CaSO_4$	100	97.5	98.9	28.4	85.8	17.6	5.4

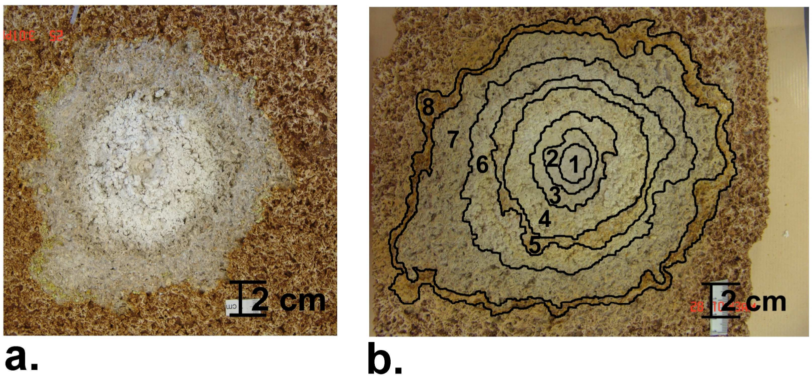

Figure 5: Acidization of a ferruginous limestone rock, by slow injection of H_2SO_4 at the center causing the dissolution of calcite ($CaCO_3$). The front is accompanied by the deposition of gypsum ($CaSO_4$) and anhydrite ($CaSO_4.2H_2O$). a. At t = 202 days. b. 'Concentric' deposition zones exhibiting oscillation in the $CaSO_4$ content at t = 692 days.

We clearly see that beyond the central region where the deposition of $CaSO_4$ is maximal (bands 1-3), the $CaSO_4$ content starts oscillating.
Very few other simulations of rock banding in-situ were attempted by a number of investigators. Rodriguez-Navarro et al. [24] observed Liesegang rings by monitoring the slow carbonation of traditional, aged lime mortars. A portlandite [$Ca(OH)_2$]/quartz mortar kept for a long time under excess, CO_2-rich water gives rise to a calcite ($CaCO_3$) deposit, via the reaction:

$$Ca(OH)_2 \ + \ CO_2 \ (aq) \ \longrightarrow \ CaCO_3 \ + \ H_2O.$$

The carbonation process yields 3D Liesgeang patterns consisting of concentric ellipsoids of alternating calcite and calcite-free zones. The rings exhibit revert spacing instead of direct spacing and obey Jablczynski's spacing law. The revert nature of the pattern was attributed to the decrease in CO_2 uptake and diffusion as the process progresses toward the core.

3. Dendritic Metal Deposits

Another intriguing class of pattern formation in solid structures is the ramified, tree-like structures we observe in metal deposits [25,26]. Two routes are known for obtaining metal deposits: electrolytic and electroless. In the former, metal ions are reduced by standard electrolysis at the cathode. In the latter, a spontaneous redox reaction is carried out in the supporting medium. We perform such a study on Ag metal deposits, by growing the latter via both methods.

Electroless

Silver metal was deposited by reduction of Ag^+ with metallic copper according to the following scheme:

$$\textit{Oxidation}: \quad Cu \rightarrow Cu^{2+} + 2\,e^- \qquad E^0_{Cu^{2+}/Cu} = +0.34\ \mathrm{V}$$

$$\textit{Reduction}: \quad Ag^+ + e^- \rightarrow Ag \qquad E_{Ag^+/Ag} = +0.80\ \mathrm{V}$$

The overall reaction is:

$$Cu + 2\,Ag^+ \rightarrow 2\,Ag + Cu^{2+} \quad (1)$$

To that end, a shallow methacrylate glass (plexiglass) dish of 10.5 cm diameter was manufactured, mounted with a peripheral ring of 0.3 mm height acting as a spacer, on top of which a plexiglass cover can rest. The solution layer thickness will thus be 0.3 mm. The cover has a 1.50 cm hole, wherein a well-fitted metallic disc (here Cu) can be inserted.

With the perforated cover on, a solution of silver nitrate of known concentration (say 0.10 M), was carefully poured through the cover hole, until it spread evenly and without air bubbles throughout the dish area. Once such a thin solution film is achieved, the copper disk is placed at the center, marking the start of the spontaneous reaction (1). One important variant from other electroless growth experiments is the bare solution medium, without soaking in a filter paper to lock the pattern. After big experimental challenges, the preliminary appearance of the fractal growth (seemingly promising) is displayed in Fig. 6.

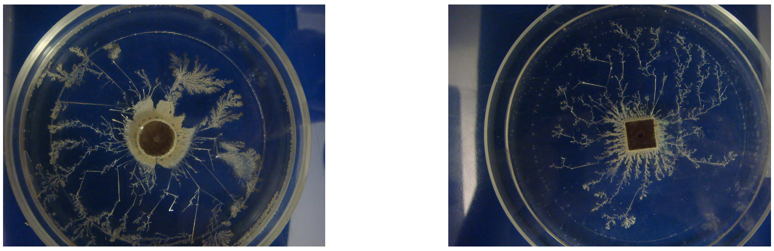

a. b.

Figure 6: Silver deposits showing dendritic structure growth. a. Circular disc of reductant (Cu). b. Square Cu disc.

An interesting observation is that the ramifications display straight, stringy branches in the circular core, whereas they exhibit curved branching with the square core. Different regions of the Ag deposits were cut, and the images transformed into black and white, for good contrast. Samples are depicted in Fig. 7.

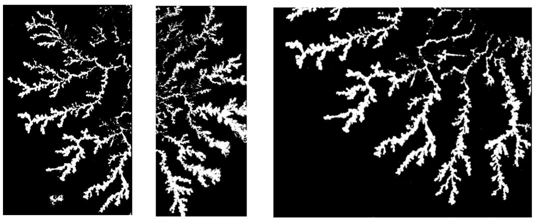

a. b. c.

Figure 7: Selected regions from the deposits in Fig. 6a after transformation of the image to black and white. The three regions (a-c) essentially exhibit the same value of the fractal dimension.

The dendrites exhibited a fractal dimension of 1.58 ± 0.04.

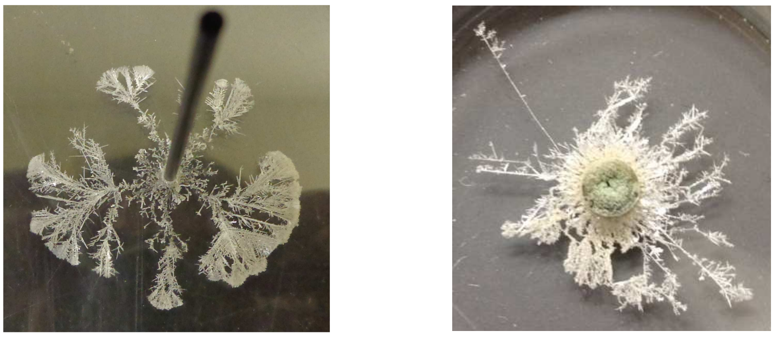

a. b.

Figure 8: a. Ag deposits by electrolysis in a circular field with potential difference of 3.09 V. b. Ag deposits via reduction of Ag^+ by Cu in a horizontal magnetic field of 0.50 T.

Electrolysis
Figure 8a shows a 'rosette' obtained by electrodeposition at a graphite electrode immersed in the solution at the dish center. The anode is a circular tungsten wire electrode of 0.5 mm diameter thickness.

Figure 8b displays electroless Ag deposits from the reduction of Ag^+ by metallic Cu, in the presence of a horizontal magnetic field of 0.50 T applied across the dish. The striking differences in the morphology (compare Figs 6a and 8b) reveal the importance, complexity and rich dynamics of metal deposition and growth. These observations are under continuing investigation at the present time.
Other dynamical studies of complex fractal structure in metal deposition systems include the simultaneous growth of two metals [27,28] and the effect of electric [29] and magnetic fields [30,31] in electroless and electrolytic systems.

Acknowledgements: This work was supported by the University Research Board (URB) of the American University of Beirut (AUB); and the Lebanese National Council for Scientific Research (LNCSR).

References

1. R. E. Liesegang. *Chemische Fernwirkung. Lieseg. Photograph. Arch.* 1896, 37:305; continued in 37:331, 1896.
2. R. Sultan and A. Abdel-Rahman. On Dynamic Self-Organization: Examples from Magmatic and Other Geochemical Systems. *Latin American Journal of Solids and Structures* (*LAJSS*) 10:59-73, 2013.
3. Samar Sadek and Rabih Sultan. Liesegang Patterns in Nature: A Diverse Scenery Across the Sciences, a *review* paper. In: Lagzi I. (ed) *Precipitation Patterns in Reaction-Diffusion Systems*. Research Signpost publications, Trivandrum, Chapter 1, pp. 1-43. 2011.
4. J. H. Kruhl (ed). *Fractals and Dynamic Systems in Geoscience*, Springer-Verlag, Berlin, 1994.
5. R. A. Schibeci and C. Carlsen. An Interseting Student Chemistry Project: Investigating Liesegang Rings. *J. Chem. Educ.* 65:365-366, 1988.
6. H. K. Henisch. *Crystals in Gels and Liesegang Rings*, Cambridge University Press, Cambridge, 1988.
7. R. Sultan and S. Sadek. Patterning Trends and Chaotic Behavior in Co^{2+}/NH_4OH Liesegang Systems. *J. Phys. Chem.*100:16912-16920,1996.
8. Wi. Ostwald, Lehrbuch der Allgemeinen Chemie, 2. Aufl., Band II, 2. Teil: Verwandtschaftslehre, Engelmann, Leipzig, 1899, p.779.
9. T. Antal, M. Droz, J. Magnin, Z. Rácz and M. Zrinyi. Derivation of the Matalon-Packter law for Liesegang patterns. *J. Chem. Phys.* 109:9479-9486, 1998.
10. Ferenc Izsák and István Lagzi , A New Universal Law for the Liesegang Pattern Formation. *J. Chem. Phys.* 122:184707-184713, 2005.

11. C. K. Jablczynski. La formation Rythmique des Précipités: Les Anneaux de Liesegang. *Bull. Soc. Chim. Fr.* 33:1592, 1923.

12. N. Kanniah, F. D. Gnanam and P. Ramasamy. *Proc. Indian Acad. Sci., Chem. Sci.* 93:801-811, 1984.

13. T. Karam, H. El-Rassy and R. Sultan. Mechanism of Revert Spacing in a $PbCrO_4$ Liesegang System. *J. Phys. Chem. A,* 115:2994-2998, 2011.

14. V. Nasreddine and R. Sultan. Propagating Fronts and Chaotic Dynamics in $Co(OH)_2$ Liesegang Systems. *J. Phys. Chem. A* 103:2934-2940, 1999.

15. R. Sultan. Propagating Fronts in Periodic Precipitation Systems with Re-dissolution. *Phys. Chem. Chem. Phys. (PCCP)* 4:1253-1261, 2002.

16. M. Zrínyi, L. Gálfi, É. Smidróczki, Z. Rácz and F. Horkay. Direct Observation of a Crossover from Heterogeneous Traveling Wave to Liesegang Pattern Formation. *J. Phys. Chem.* 95:1618-1620, 1991.

17. I. Das, A. Pushkarna and N. R. Argawal. Chemical Waves and Light-Induced Spatial Bifurcation in the Mercuric Chloride-Potassium Iodide System in Gel Media. *J. Phys. Chem.* 93:7269-7275, 1989.

18. R. Feeney, P. Ortoleva, P. Strickholm, S. Schmidt and J. Chadam. Periodic Precipitation and Coarsening Waves: Applications of the Competitive Particle Growth Model. *J. Chem. Phys.* 78:1293-1311, 1983.

19. D. S. Chernavskii, A. A. Polezhaev and S. C. Müller. A Model of Pattern Formation by Precipitation. *Physica D* 54, 160-170, 1991.

20. R. Sultan, N. Al-Kassem, A. Sultan and N. Salem. Periodic Trends in Precipitate Patterning Schemes Involving Two Salts. *Phys. Chem. Chem. Phys. (PCCP)* 2, 3155-3162, 2000.

21. P. Ortoleva. *Geochemical Self-Organization,* Oxford University Press, New York, 1994.

22. M. Msharrafieh, M. Al-Ghoul and R. Sultan. Simulation of Geochemical Banding in Acidization-Precipitation Experiments In-Situ. In: M. M. Novak (ed) *Complexus Mundi: Emergent Patterns in Nature*. World Scientific, Singapore, pp. 225-236, 2006.

23. F. Zaknoun, H. El-Rassy, M. Al-Ghoul, S. Al-Joubeily, Th. Mokalled and R. Sultan. Simulation of Geochemical Self-Organization: Acid Infiltration and Mineral Deposition in a Porous Ferruginous Limestone Rock. In: C. H. Skiadas and I. Dimotikalis (eds) *Chaotic Systems: Theory and Applications*. World Scientific, pp. 385-394, 2010.

24. C. Rodriguez-Navarro, O. Cazalia, K. Elert and E. Sebastian. Liesegang Pattern Development in Carbonating Traditional Lime Mortars. *Proc. R. Soc. Lond. A* 458:2261-2273, 2002.

25. M. Matsushita, M. Sano, Y. Hayakawa, H. Honjo and Y. Sawada. Fractal Structures of Zinc Metal Leaves Grown by Electrodeposition. *Phys. Rev. Lett.* 53:286-289, 1984.

26. R. Saab and R. Sultan. Density, Fractal Angle and Fractal Dimension in Linear Zn Electrodeposition Morphology. *J. Non-Equilib. Thermodyn.* 30:321-336, 2005.

27. E. Nakouzi and R. Sultan. Fractal Structures in Two-Metal Electrodeposition Systems I: Pb and Zn. *Chaos* 21:043133, 2011.

28. E. Nakouzi and R. Sultan. Fractal Structures in Two-Metal Electrodeposition Systems II: Cu and Zn. *Chaos* 22:023122, 2012.
29. C. M. Cronemberger and L. C. Sampaio. Growth of Fractal Electrochemical Aggregates Under electric and Magnetic Fields Using a Modified Diffusion-Limited Aggregation Algorithm *Phys. Rev. E* 73:041403, 2006.
30. I. Mogi, M. Kamiko and S. Okubo. Magnetic Field Effects on Fractal Morphology in Electrochemical Deposition. Physica B 211:319-322, 1995.
31. Y. Tanimoto, A. Katsuki, H. Yano and Sh. Watanabe. Effect of High Magnetic Field on the Silver Deposition from its Aqueous Solution. *J. Phys. Chem. A* 101:7359-7363, 1997.

Chaotic Modeling and Simulation (CMSIM) 3: 463–471, 2013

Positive Solutions for Second Order Multi-Point Boundary Value Problems

Fatma Tokmak[1] and Ilkay Yaslan Karaca[2]

[1] Ege University, Department of Mathematics, 35100 Bornova, Izmir, Turkey
(E-mail: `fatma.tokmakk@gmail.com`)
[2] Ege University, Department of Mathematics, 35100 Bornova, Izmir, Turkey
(E-mail: `ilkay.karaca@ege.edu.tr`)

Abstract. By using double fixed point theorem, we study the existence of at least two positive solutions of a second order multi-point boundary value problem.
Keywords: Positive solutions, Fixed point theorem, Boundary value problems.

1 Introduction

In this paper we consider the second order multi-point boundary value problem (BVP)

$$\begin{cases} (\phi(u'(t)))' + q(t)f(t,u(t)) = 0, \quad t \in (0,1), \\ \phi(u'(0)) = \sum_{i=1}^{m-2} a_i \phi(u'(\xi_i)), \quad u(1) = \sum_{i=1}^{m-2} b_i u(\eta_i), \end{cases} \tag{1}$$

where $\xi_i, \eta_i \in (0,1) (i = 1,2,...,m-2)$ with $0 < \xi_1 < \xi_2 < ... < \xi_{m-2} < 1$, $0 < \eta_1 < \eta_2 < ... < \eta_{m-2} < 1$, $\phi : \mathbb{R} \to \mathbb{R}$ is an increasing homeomorphism and homomorphism with $\phi(0) = 0$. A projection $\phi : \mathbb{R} \to \mathbb{R}$ is called an increasing homeomorphism and homomorphism if the following conditions are satisfied:
(i) If $x \leq y$, then $\phi(x) \leq \phi(y)$, for all $x, y \in \mathbb{R}$;
(ii) ϕ is continuous bijection and its inverse mapping is also continuous;
(iii) $\phi(xy) = \phi(x)\phi(y)$, for all $x, y \in \mathbb{R}$, where $\mathbb{R} = (-\infty, \infty)$.

We assume that the following conditions are satisfied:

(A1) $f \in \mathcal{C}([0,1] \times \mathbb{R}^+, \mathbb{R}^+)$, $q \in \mathcal{C}[0,1]$ is nonnegative,

(A2) $a_i \in [0,\infty), b_i \in [0,\infty), i = 1,2,...,m-2$ with $0 < \sum_{i=1}^{m-2} a_i < 1$ and $0 < \sum_{i=1}^{m-2} b_i < 1$.

Received: 24 April 2013 / Accepted: 21 July 2013

ISSN 2241-0503

The study of multi-point boundary value problems for linear second-order ordinary differential equations was initiated by Il'in and Moiseev [1]. Since then, there has been a lot of recent attention focused on the study of nonlinear multi-point boundary value problems, see [2–5]. We cite some appropriate references here [6–9].

In [8], Ji *et al.* studied the existence of multiple positive solutions for one-dimensional p-Laplacian boundary value problem

$$\begin{cases} (\phi(u'(t)))' + q(t)f(t,u(t)) = 0, \quad t \in (0,1), \\ u(0) = \sum_{i=1}^{n} \alpha_i u(\xi_i), \quad u(1) = \sum_{i=1}^{n} \beta_i u(\xi_i). \end{cases} \tag{2}$$

The authors established the existence of multiple positive solutions (2) by using fixed point theorem in a cone.

In [9], Ma *et al.* studied the existence of positive solutions for multi-point boundary value problem with p-Laplacian operator

$$\begin{cases} (\phi(u'(t)))' + q(t)f(t,u(t)) = 0, \quad t \in (0,1), \\ u'(0) = \sum_{i=1}^{n} \alpha_i u'(\xi_i), \quad u(1) = \sum_{i=1}^{n} \beta_i u(\xi_i). \end{cases} \tag{3}$$

In this paper, motivated by the above research efforts on multi-point boundary value problems, criteria for the existence of at least two positive solutions of the BVP (1) are established by using the double fixed point theorem. Thus, our results are new for differential equations.

This paper is organized as follows. In Section 2, we give some preliminary lemmas which are key tools for our proof. The main result is given in Section 3.

2 Preliminaries

In this section, we give some lemmas which are useful for our main result.

We consider the Banach space $\mathbb{B} = \mathcal{C}^1[0,1]$ endowed with the norm

$$\|u\| = \max_{0 \le t \le 1} |u(t)|.$$

Define the cone $\mathcal{P} \subset \mathbb{B}$ by

$$\mathcal{P} = \{u \in \mathbb{B} : u \text{ is a concave, nonnegative and nonincreasing function,} \\ u(1) = \textstyle\sum_{i=1}^{m-2} b_i u(\eta_i)\}.$$

Lemma 1. *If* $u \in \mathcal{P}$*, then* $\min_{0 \le t \le 1} u(t) \ge M\|u\|$*, where* $M = \dfrac{\sum_{i=1}^{m-2} b_i(1-\eta_i)}{1 - \sum_{i=1}^{m-2} b_i \eta_i}$.

Proof. Since $u \in \mathcal{P}$, nonnegative and nonincreasing

$$\|u\| = u(0), \quad \min_{0 \le t \le 1} u(t) = u(1).$$

On the other hand, $u(t)$ is concave on $[0,1]$. So, for every $t \in [0,1]$, we have

$$\frac{u(t) - u(1)}{1-t} \ge \frac{u(0) - u(1)}{1},$$

i.e., $u(t) \ge (1-t)u(0) + tu(1)$. Therefore,

$$\sum_{i=1}^{m-2} b_i u(\eta_i) \ge \sum_{i=1}^{m-2} b_i (1-\eta_i) u(0) + \sum_{i=1}^{m-2} b_i \eta_i u(1).$$

This together with $u(1) = \sum_{i=1}^{m-2} b_i u(\eta_i)$, implies that

$$u(1) \ge \frac{\sum_{i=1}^{m-2} b_i (1-\eta_i)}{1 - \sum_{i=1}^{m-2} b_i \eta_i} u(0).$$

So, the proof of Lemma is completed. □

Lemma 2. *Assume that* $(A1), (A2)$ *hold. Then* $u \in \mathcal{C}^1[0,1]$ *is a solution to problem* (1) *if and only if* u *is a solution to the integral equation:*

$$u(t) = \int_t^1 \phi^{-1} \left(\int_0^s q(\tau) f(\tau, u(\tau)) d\tau + A \right) ds$$

$$+ \frac{1}{1 - \sum_{i=1}^{m-2} b_i} \sum_{i=1}^{m-2} b_i \int_{\eta_i}^1 \phi^{-1} \left(\int_0^s q(\tau) f(\tau, u(\tau)) d\tau + A \right) ds, \qquad (4)$$

where

$$A = \frac{1}{1 - \sum_{i=1}^{m-2} a_i} \sum_{i=1}^{m-2} a_i \int_0^{\xi_i} q(s) f(s, u(s)) ds. \qquad (5)$$

Proof. First, suppose that $u \in \mathcal{C}^1[0,1]$ is a solution of problem (1). Integrating the equation (1) from 0 to t, one has

$$-\phi(u'(t)) + \phi(u'(0)) = \int_0^t f(s, u(s)) ds. \qquad (6)$$

and taking $t = \xi_i$ in (6), we have

$$\phi(u'(\xi)) = \phi(u'(0)) - \int_0^{\xi_i} q(s)f(s,u(s))ds.$$

So, we get

$$\sum_{i=1}^{m-2} a_i\phi(u'(\xi_i)) = \sum_{i=1}^{m-2} a_i\phi(u'(0)) - \sum_{i=1}^{m-2} a_i \int_0^{\xi_i} q(s)f(s,u(s))ds.$$

Since $\phi(u'(0)) = \sum_{i=1}^{m-2} \alpha_i\phi(u'(\xi_i))$, we have

$$\phi(u'(0)) = -\frac{1}{1-\sum_{i=1}^{m-2}\alpha_i} \sum_{i=1}^{m-2} \alpha_i \int_0^{\xi_i} q(s)f(s,u(s))ds = -A. \tag{7}$$

Substituting (7) into (6), we get

$$u'(t) = -\phi^{-1}\left(\int_0^t q(s)f(s,u(s))ds + A\right). \tag{8}$$

Integrating the equation (8) from t to 1, one has

$$u(t) = u(1) + \int_t^1 \phi^{-1}\left(\int_0^s q(\tau)f(\tau,u(\tau))d\tau + A\right), \tag{9}$$

and taking $t = \eta_j$ in (9), we get

$$u(\eta_j) = u(1) + \int_{\eta_j}^1 \phi^{-1}\left(\int_0^s q(\tau)f(\tau,u(\tau))d\tau + A\right)ds.$$

So,

$$\sum_{i=1}^{m-2} b_i u(\eta_i) = u(1)\sum_{i=1}^{m-2} b_i + \sum_{i=1}^{m-2} b_i \int_{\eta_i}^1 \phi^{-1}\left(\int_0^s q(\tau)f(\tau,u(\tau))d\tau + A\right)ds.$$

Since $u(1) = \sum_{i=1}^{m-2} b_i u(\eta_i)$,

$$u(1) = \frac{1}{1-\sum_{i=1}^{m-2} b_i}[\sum_{i=1}^{m-2} b_i \int_{\eta_i}^1 \phi_{-1}\left(\int_0^s q(\tau)f(\tau,u(\tau))d\tau + A\right)ds. \tag{10}$$

Substituting (10) into (9), we get (4), which completes the proof of sufficiency.

Conversely, if $u \in C^1[0,1]$ is a solution to (4), apparently

$$u'(t) = -\phi^{-1}\left(\int_0^t q(s)f(s,u(s))ds + A\right),$$

$$(\phi(u'(t)))' = -q(t)f(t,u(t)),$$

$$\phi(u'(0)) = \sum_{i=1}^{m-2} a_i\phi_p(u'(\xi_i)), \quad u(1) = \sum_{i=1}^{m-2} b_i u(\eta_i).$$

The proof is complete. $\square$

Now define an operator $T : \mathcal{P} \longrightarrow \mathbb{B}$ by

$$Tu(t) = \int_t^1 \phi^{-1}\left(\int_0^s q(\tau)f(\tau,u(\tau))d\tau + A\right) ds$$

$$+\frac{1}{1-\sum_{i=1}^{m-2} b_i} \sum_{i=1}^{m-2} b_i \int_{\eta_i}^1 \phi^{-1}\left(\int_0^s q(\tau)f(\tau,u(\tau))d\tau + A\right) ds. \quad (11)$$

Lemma 3. *Assume that* $(A1)-(A2)$ *hold. Then* $T : \mathcal{P} \to \mathcal{P}$ *is a completely continuous operator.*

Proof. It is clear that $T\mathcal{P} \subset \mathcal{P}$ and $T : \mathcal{P} \to \mathcal{P}$ is a completely continuous operator by a standard application of the Arzela-Ascoli theorem.

3 Main Results

In this section we state and prove our main result. The following fixed point theorem is fundamental and important to the proof of main result.

For a nonnegative continuous functional γ on a cone $\mathcal{P}$ in a real Banach space $\mathbb{B}$, and each $d > 0$, we set

$$\mathcal{P}(\gamma, d) = \{x \in \mathcal{P} |\ \gamma(x) < d\}.$$

Lemma 4. *(Double Fixed Point Theorem) [10] Let* $\mathcal{P}$ *be a cone in a real Banach space* $\mathbb{B}$*. Let* α *and* γ *be increasing, nonnegative, continuous functionals on* $\mathcal{P}$*, and let* θ *be a nonnegative, continuous functional on* $\mathcal{P}$ *with* $\theta(0) = 0$ *such that, for some* $c > 0$ *and* $M > 0$*,*

$$\gamma(u) \le \theta(u) \le \alpha(u) \ \textit{and}\ \|u\| \le M\gamma(u)$$

for all $u \in \overline{\mathcal{P}(\gamma, c)}$*. Suppose that there exist positive numbers* a *and* b *with* $a < b < c$ *such that*

$$\theta(\lambda u) \le \lambda\theta(u), \quad \textit{for} \quad 0 \le \lambda \le 1 \quad \textit{and} \quad u \in \partial\mathcal{P}(\theta, b)$$

and

$$T : \overline{\mathcal{P}(\gamma, c)} \to \mathcal{P}$$

is a completely continuous operator such that:

(i) $\gamma(Tu) > c$*, for all* $u \in \partial\mathcal{P}(\gamma, c)$*;*
(ii) $\theta(Tu) < b$*, for all* $x \in \partial\mathcal{P}(\theta, b)$*;*
(iii) $\mathcal{P}(\alpha, a) \ne \emptyset$*, and* $\alpha(Tu) > a$*, for all* $u \in \partial\mathcal{P}(\alpha, a)$*.*

Then T has at least two fixed points, u_1 and u_2 belonging to $\overline{\mathcal{P}(\gamma, c)}$ such that

$$a < \alpha(u_1), \quad \textit{with} \quad \theta(u_1) < b,$$

and

$$b < \theta(u_2), \quad \textit{with} \quad \gamma(u_2) < c.$$

Let us define the increasing, nonnegative, continuous functionals $\gamma,\ \beta$, and α on $\mathcal{P}$ by

$$\begin{aligned} \gamma(u) &= \min_{0 \le t \le \xi_1} u(t) = u(\xi_1), \\ \beta(u) &= \max_{\xi_1 \le t \le \xi_{n-2}} u(t) = u(\xi_1), \\ \alpha(u) &= \max_{0 \le t \le \xi_{n-2}} u(t) = u(0). \end{aligned}$$

It is obvious that for each $u \in \mathcal{P}$,

$$\gamma(u) \le \beta(u) \le \alpha(u).$$

In addition, from by Lemma 1, for each $u \in \mathcal{P}$,

$$\|u\| \le \frac{1}{M} \min_{0 \le t \le 1} u(t) \le \frac{1}{M} \min_{0 \le t \le \xi_1} u(t) = \frac{1}{M}\gamma(u).$$

Thus,

$$\|u\| \le \frac{1}{M}\gamma(u), \quad \forall u \in \mathcal{P}.$$

For the convenience, we denote

$$\begin{aligned} K &= (1-\xi_1)\phi^{-1}\left(\int_0^{\xi_1} q(\tau)d\tau\right), \\ L &= \frac{1}{1-\sum\limits_{i=1}^{m-2} b_i}\phi^{-1}\left(\frac{1}{1-\sum_{i=1}^{m-2} a_i}\int_0^{\xi_1} q(\tau)d\tau\right). \end{aligned}$$

Theorem 1. *Suppose that assumptions $(A1), (A2)$ are satisfied. Let there exist positive numbers $a < b < c$ such that*

$$0 < a < \frac{K}{L}b < \frac{KM}{L}c,$$

and assume that f satisfies the following conditions

(A3) $f(t,u) > \phi\left(\frac{c}{K}\right)$, *for all* $(t,u) \in [0,\xi_1] \times [c, \frac{1}{M}c]$,
(A4) $f(t,u) < \phi\left(\frac{b}{L}\right)$, *for all* $(t,u) \in [0,1] \times [0, \frac{1}{M}b]$,
(A5) $f(t,u) > \phi\left(\frac{a}{K}\right)$, *for all* $(t,u) \in [0,1] \times [0, a]$.

Then the boundary value problem (1) *has at least two positive solutions* u_1 *and* u_2 *satisfying*

$$a < \alpha(u_1) \text{ with } \beta(u_1) < b, \quad b < \beta(u_2) \text{ with } \gamma(u_2) < c.$$

Proof. We define the completely continuous operator T by (11). So, it is easy to check that $T : \overline{\mathcal{P}(\gamma, c)} \to \mathcal{P}$. We now show that all the conditions of Lemma 4 are satisfied. In order to show that condition (i) of Lemma 4, we choose $u \in \partial\mathcal{P}(\gamma, c)$. Then $\gamma(u) = \min_{0\le t\le \xi_1} u(t) = u(\xi_1) = c$, this implies that $c \le u(t)$ for $t \in [0, \xi_1]$. Recalling that $\|u\| \le \frac{1}{M}\gamma(u) = \frac{1}{M}c$, we get

$$c \le u(t) \le \frac{1}{M}c, \quad t \in [0, \xi_1].$$

Then assumption $(A3)$ implies $f(t, u) > \phi\left(\frac{c}{A}\right)$, for all $(t, u) \in [0, \xi_1] \times [c, \frac{1}{M}c]$. Therefore,

$$\begin{aligned}
\gamma(Tu) &= \min_{t\in[0,\xi_1]} (Tu)(t) = (Tu)(\xi_1)\\
&\ge \int_{\xi_1}^{1} \phi^{-1}\left(\int_0^s q(\tau)f(\tau, u(\tau))d\tau\right) ds\\
&\ge \int_{\xi_1}^{1} \phi^{-1}\left(\int_0^{\xi_1} q(\tau)f(\tau, u(\tau))d\tau\right) ds\\
&= (1-\xi_1)\phi^{-1}\left(\int_0^{\xi_1} q(\tau)f(\tau, u(\tau))d\tau\right)\\
&> \frac{c}{K}(1-\xi_1)\phi^{-1}\left(\int_0^{\xi_1} q(\tau)d\tau\right)\\
&= c.
\end{aligned}$$

Hence, condition (i) is satisfied.

Secondly, we show that (ii) of Lemma 4 is satisfied. For this, we select $u \in \partial\mathcal{P}(\beta, b)$. Then, $\beta(u) = \max_{t\in[\xi_1,\xi_{n-2}]} u(t) = u(\xi_1) = b$, this means $0 \le u(t) \le b$, for all $t \in [\xi_1, 1]$. Noticing that $\|u\| \le \frac{1}{M}\gamma(u) = \frac{1}{M}\beta(u) = \frac{1}{M}b$, we get

$$0 \le u(t) \le \frac{1}{M}b, \text{ for } 0 \le t \le 1.$$

Then, assumption $(A4)$ implies $f(t, u) < \phi\left(\frac{b}{L}\right)$. Therefore

$$\begin{aligned}
\beta(Tu) &= \max_{t\in[\xi_1,\xi_{m-2}]} (Tu)(t) = (Tu)(\xi_1)\\
&\le \frac{1}{1-\sum_{i=1}^{m-2} b_i}\phi^{-1}\left(\frac{1}{1-\sum_{i=1}^{m-2} a_i}\int_0^1 q(\tau)f(\tau, u(\tau))d\tau\right)
\end{aligned}$$

$$
\begin{aligned}
&< \frac{b}{L}\frac{1}{1-\sum_{i=1}^{m-2} b_i}\phi^{-1}\left(\frac{1}{1-\sum_{i=1}^{m-2} a_i}\int_0^1 q(\tau)d\tau\right)\\
&= b.
\end{aligned}
$$

So, we get $\beta(Tu) < b$. Hence, condition (ii) is satisfied.

Finally, we show that the condition (iii) of Lemma 4 is satisfied. We note that $u(t) = a\left(\frac{\sum_{i=1}^{m-2} b_i - 1}{1-\sum_{i=1}^{m-2} b_i\eta_i}t+1\right)$, $0 \leq t \leq 1$ is a member of $\mathcal{P}(\alpha, a)$, and so $\mathcal{P}(\alpha, a) \neq \emptyset$. Now, let $u \in \partial\mathcal{P}(\alpha, a)$. Then $\alpha(u) = \max_{t\in[0,\xi_{n-2}]} u(t) = u(0) = a$. This implies

$$
0 \leq u(t) \leq a,\ t \in [0,1].
$$

By assumption $(A5)$, $f(t,u) > \phi\left(\frac{a}{A}\right)$. Then,

$$
\begin{aligned}
\alpha(Tu) &= \max_{t\in[0,\xi_{n-2}]}(Tu)(t) = (Tu)(0)\\
&\geq \int_0^1 \phi^{-1}\left(\int_0^s q(\tau)f(\tau,u(\tau))d\tau + A\right)ds\\
&\geq \int_{\xi_1}^1 \phi^{-1}\left(\int_0^s q(\tau)f(\tau,u(\tau))d\tau\right)ds\\
&\geq (1-\xi_1)\phi^{-1}\left(\int_0^{\xi_1} q(\tau)f(\tau,u(\tau))d\tau\right)\\
&> (1-\xi_1)\frac{a}{A}\phi^{-1}\left(\int_0^{\xi_1} q(\tau)d\tau\right) = a.
\end{aligned}
$$

So, we get $\alpha(Tu) > a$. Thus, (iii) of Lemma 4 is satisfied. Hence, the boundary value problem (1) has at least two positive solutions u_1 and u_2 satisfying

$$
a < \alpha(u_1) \text{ with } \beta(u_1) < b, \text{ and } b < \beta(u_2) \text{ with } \gamma(u_2) < c.
$$

□

References

1. V. A. Ilin and E. I. Moiseev. A nonlocal boundary value problem of the first kind for the Sturm-Liouville operator in differential and difference interpretations. *Differentsialnye Uravneniya*, 23:1198–1207, 1987.
2. C. Bai and J. Fang. Existence of multiple positive solutions for nonlinear m-point boundary value problems. *J. Math. Anal. Appl.*, 281:76-85, 2003.

3.C. Bai and J. Fang. Existence of multiple positive solutions for nonlinear m-point boundary value problems. *Appl. Math. Comput.*, 140:297-305, 2003.
4.K. Q. Lan. Multiple positive solutions of semilinear differential equations with singularities. *J. London Math. Soc.*, 63:690-704, 2005.
5.R. Ma. Existence theorem for a second order m-point boundary value problem. *J. Math. Anal. Appl.* 211:545-555, 1997.
6.J. Y. Wang and W. J. Guo. A singular boundary value problem for the one-dimensional p-Laplacian. *J. Math. Anal. Appl.* 201:851-866, 1996.
7.Y. Wang and C. Hou. Existence of multiple positive solutions for one-dimensional p-Laplacian. *J. Math. Anal. Appl.* 315:144-153, 2006.
8.D. Ji, M. Feng and W. Ge. Multiple positive solutions for multipoint boundary value problems with sign changing nonlinearity. *Appl. Math. Comput.*, 196:511-520, 2008.
9.D. Ma, Z. Du and W. Ge. Existence and iteration of monotone positive solutions for multipoint boundary value problem with p-Laplacian operator. *Comput. Math. Appl.*, 50:729-739, 2005.
10.R. I. Avery and J. Henderson. Two positive fixed points of nonlinear operators on ordered Banach spaces. *Comm. Appl. Nonlin. Anal.*, 8:27-36, 2001.